Tribocorrosion in pressurized high temperature water: a mass flow model based on the third body approach

(EPFL)
ÉCOLE POLYTECHNIQUE
FÉDÉRALE DE LAUSANNE

Suisse
2014

Remerciements

A l'issue de ce travail de recherche, je suis plus que convaincue qu'une thèse est un travail qui de loin peut être réalisé en solitaire. Grand nombre de personnes ont contribué à ce que celui-ci soit achevé avec succès et sur ces quelques paragraphes j'aimerais les remercier.

En premier lieu, je tiens à remercier mon directeur de thèse, Stefano Mischler, pour l'opportunité inoubliable d'avoir pu entreprendre cette thèse dans un domaine aussi intéressant que la tribocorrosion. Je lui suis reconnaissante pour ces brainstormings pleins de nouvelles idées qui m'ont enrichie jours après jours. Mais surtout je le remercie pour sa gaité et sa bonne humeur qui ont fait un environnement de travail très encourageant et agréable. Je me souviendrai toujours de cette phrase *« la tribologie porte la richesse de sa complexité »* qu'il a su me répéter lorsque les choses devenaient dures à comprendre. Merci pour m'avoir permis de voir les choses depuis un tout autre point de vue.

Je tiens à remercier Areva, pour le soutien financier de cette thèse. Je remercie également les collaborateurs, Walter-John Chitty, Dominique Hertz, Carole Falcand et Damien Kaczorowski pour avoir contribué à l'avancement du projet.

Je veux remercier au Prof. Dragan Damjanovic de l'EPFL, Prof. Nicholas Spencer de l'EHTZ, le Prof. Robert Wood de l'Université de Southampton et Dr. Walter-John Chitty d'Areva de d'avoir accepté de faire partie de mon jury de thèse et de l'attention portée à mon travail.

Mes remerciements vont également à mes collègues qui ont vécu mon quotidien pendant beaucoup et même peu de temps. D'abord, merci *Pierre Mettraux* pour tant de choses que je ne saurais énumérer. Tu es devenu plus qu'un collaborateur, un ami. Merci pour ces heures de MEB agrémentées de discussions allant de la technique jusqu'au sport, pour ton support technique lorsqu'on avait à faire à Microsoft et ou Labview, pour tes conseils avisés tant dans la pratique comme dans la technique et pour quelques tours à Aubonne. Je tiens aussi à remercier à Nicolas Xanthopoulos pour sa « patience » lors des analyses Auger surtout lors des profils en profondeur. Mais aussi pour sa qualité humaine et sa volonté de vouloir m'initier à quelques sports d'hiver

sans beaucoup de succès. Je souhaite aussi remercier le Professeur Anna Igual Muñoz (UPV) pour une année pleine de partage, des discussions très enrichissantes lors de son séjour en Suisse. Merci pour tes encouragements et cette vitalité quotidienne que tu as su nous transmettre en grandes doses même lorsque le mauvais temps ne laissait pas voir les montagnes. Merci au Dr. Javier Navarro (UPV) pour avoir apporté des idées très intéressantes dans la dernière phase du projet et proprement dit dans la modélisation mathématique.

Et bien sûr, un projet sans collègues doctorant(e)s n'est pas un projet complet. Je remercie à Shoufan pour son initiation à l'alphabet chinois. Merci Angelita pour m'avoir amené un peu de chaleur Sud-Américaine dans mon quotidien. Merci à Carlos pour son énergie espagnole et les explications pour l'impédance. Merci à vous trois pour la bonne ambiance et les moments de partage tant scientifique comme humains. Je vous souhaite une bonne continuation et bon courage.

Je ne manquerai pas de remercier mes ami(e)s Charline, Marion, Delphine, Auré, Yvan, Bruna, Flo, Cornelia pour des moments de partage, découverte et soutient pendant ces années EPFL. Un grand merci à Adolfo pour avoir su me réconcilier avec mes racines et m'apporter son support affectif et moral. Je lui serai toujours reconnaissante de m'avoir supporté tout ce temps.

Il me reste à remercier ma famille, qui même en étant loin, a su être présente quand j'en ai eu besoin. Merci : A mes grands-parents (Eduardo y Maria) pour leurs bénédictions. A mon oncle (Santiago), pour être celui qui m'a motivée à suivre l'école polytechnique dès mon jeune âge. A mon père (Nicolas) et ma sœur (Laura) pour avoir su me donner des mots motivants pour aller de l'avant. Mais surtout à ma mère, Nelly Maldonado, pour avoir été un pilier et qui a su être un exemple de persévérance et sacrifice toutes ces années. Je ne pourrais jamais la remercier pour toutes les choses qu'elle a pu m'apporter mais je résume tout ça comme étant son amour de mère. Cette thèse lui est dédiée.

A ma mère et son dévouement

Abstract

Pressurized water reactors (PWR) used for power generation are operated at elevated temperatures (280-300°C) and under high pressure (120-150 bar). In addition to these harsh environmental conditions some components of the PWR assemblies are subject to mechanical loading (sliding, vibration and impacts) leading to undesirable and hardly controllable material degradation phenomena. In such situations wear is determined by the complex interplay (tribocorrosion) between mechanical, material and physical-chemical phenomena. Tribocorrosion in PWR conditions is at present little understood and models need to be developed in order to predict component lifetime over several decades.

The goal of this project, carried out in collaboration with the French company AREVA NP, is to develop a predictive model based on the mechanistic understanding of tribocorrosion of specific PWR components (stainless steel control assemblies, stellite grippers). The approach taken here is to describe degradation in terms of electro-chemical and mechanical material flows (third body concept of tribology) from the metal into the friction film (i.e. the oxidized film forming during rubbing on the metal surface) and from the friction film into the environment instead of simple mass loss considerations.

The project involves the establishment of mechanistic models for describing the single flows based on ad-hoc tribocorrosion measurements operating at low temperature. The overall behavior at high temperature and pressure is investigated using a dedicated tribometer (Aurore) including electrochemical control of the contact during rubbing.

Physical laws describing the individual flows according to defined mechanisms and as a function of defined physical parameters were identified based on the obtained experimental results and from literature data. The physical laws were converted into mass flow rates and solved as differential equation system by considering the mass balance in compartments representing the substrate metal, the metallic and oxide fractions of the friction film (third body) and the aqueous environment.

The obtained model permits to evaluate the evolution with time of the mass in each compartment and thus to gain better insight in the phenomenology and in the mechanisms of tribocorrosion of metals in PWR conditions. It also allows assessing the relative role of a variety of materials, mechanical and electrochemical parameters affecting the entire system. Quantitative predictions of the model were found to fit reasonably well experimental observations. However, assessing the quantitative validity of the model requires the exact quantification of some critical parameters, in particular the metal oxide wear rate, and thus further experimental work. The model was used to appraise the role of certain materials parameters and showed that the oxidation behavior of the rubbing metal plays a crucial role in PWR tribological degradation.

KEYWORDS

PWR, third body, mass flow, mechanistic modeling

Résumé

Les réacteurs à eau pressurisée (REP) utilisés pour la génération d'énergie sont exploités à des températures élevées (280-300°C) et sous haute pression (120-150 bar). En plus de ces conditions sévères certains composants de systèmes de REP subissent des charges mécaniques (frottements, vibrations et impacts) menant à des phénomènes indésirables et difficilement contrôlables de dégradations des matériaux. Dans de telles conditions, l'usure est déterminée par les interactions complexes (tribocorrosion) des phénomènes mécaniques, physico-chimiques et ceux liés aux matériaux. La tribocorrosion dans des conditions de REP est actuellement peu comprise et requiert la création de modèles permettant de prédire la durée de vie de composants sur plusieurs décennies.

Le but de ce projet, accompli en collaboration avec l'entreprise française AREVA NP, est de développer un modèle prévisionnel basé sur la compréhension mécanistique de la tribocorrosion de composants spécifiques aux REP (systèmes de contrôle en acier inoxydable, préhenseurs en stellite). L'approche sélectionnée ici consiste à décrire la dégradation en termes de flux matériels électrochimiques et mécaniques (concept tribologique de troisième corps) du métal au film de friction (la couche oxydée formée lors du frottement sur la surface métallique) et du film de friction au milieu environnant au lieu d'une simple considération de perte de masse.

Ce projet englobe la création de modèles mécanistiques décrivant les flux simples basés sur des mesures ad-hoc de tribocorrosion à basse température. Le comportement général à haute température et à pression élevée est examiné en utilisant un tribomètre (Aurore) dédié incluant le contrôle électrochimique du contact durant le frottement.

Des lois physiques, qui décrivent de manière individuelle les flux en accord aux mécanismes et en fonction des paramètres physiques, ont été identifiées basé sur des valeurs expérimentales et depuis la littérature. Les lois physiques ont été converties en débit de masses et résolues en utilisant un système des équations différentielles en considérant le balance des masses dans chaque compartiment. Ces derniers représentent le substrat, les particules métalliques dans le

film de friction, des particules oxydés aussi dans le film de friction (troisième corps) et finalement à l'extérieur (milieu aqueux) un compartiment avec des fractions d'oxyde sortant du film.

Le modèle permet l'évaluation de l'évolution de la variation de masse en fonction du temps dans chaque compartiment et, de cette façon, augmenter la compréhension des mécanismes reliés à la tribocorrosion en conditions REP.

Il permet également d'évaluer le rôle des paramètres matériaux, mécaniques et électrochimiques affectant l'ensemble du système. Les prévisions quantitatives du modèle ont été trouvés qu'elles satisfont les observations. Toutefois, l'évaluation quantitative de la validité du modèle nécessite la quantification précise de certains paramètres critiques, en particulier le taux d'usure d'oxyde, et donc la poursuite des travaux expérimentaux. Le modèle a été utilisé pour évaluer le rôle de certains paramètres du matériau et a montré que le comportement de l'oxydation dans le frottement joue un rôle crucial dans la dégradation dans des conditions REP.

MOTS-CLES : REP, troisième corps, flux de masses, modélisation mécanistique

Contents

Chapter 1　Introduction

Several metallic components of pressurized water reactors (PWR) used in nuclear power plants are exposed to the combined degradation by friction and corrosion (tribocorrosion). In PWR, corrosion arises from the water pressurized at 150 bars and maintained at 300°C and results in the build up of a micrometer thick surface oxide film. The complex water flow inside the reactor exerts mechanical vibrations of the structure that in turn convert into sliding, fretting and impacts on specific, non rigid components such as control rod assemblies. Tribocorrosion is of complex nature as it involves multi-scale interactions between mechanical, chemical and material factors. Nevertheless, PWR component manufacturers are interested in understanding the deterioration mechanisms as a prerequisite for the improvement of test methods, the selection of appropriate materials and for component lifetime prediction.

Tribocorrosion mechanism, as degradation process, results from the interaction of mechanical and chemical factors. Therefore, they cannot be treated as the simple addition of wear and corrosion taken separately. As an example in PWR conditions the build up of surface oxide films protects the underlying metal against corrosion. However, mechanical loading may disrupt the film and therefore profoundly modify the corrosion behavior. On the other hand, the same film could have a mechanical screening effect preventing plastic deformation of the underlying metal, a mechanism often found responsible for surface film disruption. The understanding of a complex phenomenon such as tribocorrosion requires thus considering the interaction of a number of chemical, mechanical and materials parameters and the interplay of different degradation phenomena. Tribology research has been focused mainly on mechanical interpretation of wear, lubrication and friction and existing models well describe such phenomena in terms of loads, velocity and materials mechanical properties. However, theoretical concepts including chemical reactivity of the contact are still in development and comprehensive models still missing. Thus, the

scientific appraisal of tribocorrosion in PWR conditions requires the development of appropriate experimental and theoretical tools accounting for the combined action of mechanical, chemical and materials factors.

The goal of this thesis is to develop a model describing wear process in pressurized water reactor conditions based on a mechanistic multidisciplinary approach integrating well-defined degradation mechanisms and governing parameters. The mechanistic approach is needed in order to relate wear to physical meaningful parameters as a prerequisite for appraising the causes of wear in industrial systems and for highlighting the influence of critical materials parameters and water properties on the system evolution.

The present thesis is divided into four parts:

> PART 1 (Chapter 2 and Chapter 3)

This part deals with the problem identification and the definitions of the goal and of the strategy. After a general description of a typical nuclear reactor and some of its components subject to tribocorrosion, the physical phenomena characterizing materials degradation in PWR are reviewed based on published literature (Chapter 2). Application relevant corrosion and tribological theoretical aspects are discussed (Chapter 2). Based on the literature review, a mechanistic vision of the tribocorrosion in PWR is proposed. This mechanistic model is best modeled using the third body concept of tribology, which allows describing the overall degradation process in terms of mass flows describing chemical and mechanical material transfer from the rubbing metal into the third body, chemical reactions within the third body, material ejection from the third body and material transfer form the environment into the third body (Chapter 3).

> PART 2 (Chapter 4 and Chapter 5)

The definition of the mass flows requires experimental evidence aimed at identifying determining mechanisms and crucial parameters. This is achieved by investigating model systems using EPFL laboratory tribo-electrochemical tests as well as a high temperature pressurized water electrochemical tribometer purposely developed by Areva to simulate PWR chemical and mechanical conditions. Their utilization is tailored to isolate and investigate specific flows. The obtained results are interpreted in terms of known models.

PART 3 (Chapter 6)

This chapter deals with the definition of physical laws describing each individual mass flow as a function of well-defined physical parameters according to a mechanistic vision of the involved phenomena. The laws will be deduced from the experimental observations issued from the previous chapters as well from existing literature. Some flows are hardly to be isolated and investigated; in these cases the laws will be defined based on kinetic hypotheses.

PART 4 (Chapter 7)

The next step is to assemble the physical flow laws identified in Part 3 into a set of time dependent differential equations that will be solved using a purposely developed computer routine based on Mathematica software. For this, four compartments assigned to the different physical zones of the wearing surface will be defined. The mass balance in each compartment is formalized using the flow rates defined in the previous chapter. Predictions from the numerical model will be compared to experimental results in an attempt to assess its validity and its limitations as prerequisite for future improvements. Finally, the developed algorithm is used to appraise quantitatively the relative role of key material parameters on the overall tribocorrosion process in pressurized water reactor conditions.

Finally, Chapter 8 summarizes the main results and conclusions of the work and proposes some future lines for further model development.

Chapter 2   State of the art

This chapter first introduces the context and the tribocorrosion issues in nuclear power reactors. The related theoretical concepts of wear and corrosion are subsequently presented. Finally, a literature survey on the degradation phenomena in PWR (carried out using the ISI Web of Knowledge data base and on the keywords "wear mechanism" and "water reactor" or "pwr" or "high temperature water") is presented. This allows discussing the relevant mechanisms and assessing the possibilities and limits of available models.

2.1 Wear in nuclear power reactors

2.1.1 Pressurized water reactors PWRs

Nuclear energy is principally generated using two kinds of reactors: pressurized water reactor (PWR) and boiling water reactor (BWR). They were developed in the 1950s and improved since. Both reactors are commonly found in the US and Japan. In France, Russia and China the majority of the nuclear plants uses PWRs. The energy provided by theses reactors is principally for power generation but also for naval propulsion. In fact, the PWRs were originally designed as a submarine power plant [1].

PWRs and BWRs present similarities concerning the fuel (enriched UO_2) and control systems but their principal difference concern the water flow system. BWRs present a single reactor-turbine circuit where water is pressurized at 75bars and it boils in the core of the reactor at 285°C. The produced steam passes through drier plates located in the upper part of the reactor and then it goes directly to the turbine for power generation. In the case of a PWR, water flows through the core and the tubes of a steam generator forming a closed-loop system. In this primary circuit, water is at 325°C and 150bars to prevent boiling. The heat is then transferred to a secondary water circuit where steam is generated. The produced steam drives a turbine for electricity production. After condensation it is conducted again to the heat exchanger. The advantage of the PWR is that no radioactive contamination is present in the steam. As a consequence, the turbine does not need to be shielded and radiologically protected.

Both, PWR and BWR, are considered as light water reactors (LWRs) because they use water as neutron moderator and coolant. It exists also pressurized heavy water reactors (CANDU) using deuterium oxides as moderator [2]. The water used in the reactor core slows down the neutron release, reduces their reactivity and thus acts as a neutron moderator. The water composition in the reactor core varies depending on the reactor type. In BWRs, pure water is used to cool down the reactor and at the same time it acts as a moderator because there is only a single reactor-turbine circuit. Water circulating in the reactor core is contaminated by corrosion products and dissolved oxygen. To eliminate oxygen, hydrogen is continuously added in the recirculation piping system. In PWRs, water passing through the reactor core is de-aerated and of low conductivity. Main additions are lithine, (0.4 to 2 ppm), boric acid (1000 to 1500 ppm) and hydrazine to control

neutron reaction, keep the pH at 7 and eliminate dissolved oxygen as corrosion agent. Water in the secondary circuit is rich in corrosion products mainly iron species released by steel piping components. In order to suppress the formation and transport of corrosion products to the steam generators, compounds such as ammonia and hydrazine are added in the water circuit. Ammonia establishes alkaline pH in the whole steam water system [3]. Hydrazine acts as oxygen scavenger and reduces oxidized iron species to magnetite [4]. Hydrogen is also controlled in order to optimize corrosion products detachment. These latters may modify the structure and morphology of the oxide by precipitating on the surface [5].

2.1.2 Components

In PWR reactors different assemblies and control mechanisms can be found. Among them, the fuel assembly, the rod cluster control assembly (RCCA) and the control rod drive mechanism (CRDM) showed in the Figure 2-1. The Fuel assembly is constituted of vertically mounted Zirconium alloy tubes or rods with the Uranium pellets stacked inside. They are guided along the vertical axis by spacer grids where a system of springs and dimples support the rods (Figure 2-1a) [6]. In order to reduce power, rods containing neutron-absorbing material are lifted in between the fuel rods. Theses rods made out of stainless steel (316L or 316 nitratred) are part of the RCCA shown in Figure 2-1b. They are fastened to a component called spider and guided to the core of the reactor by 304 stainless steel plates [7]. The RCCA is inserted or hold in the correct position by the control rod drive mechanism (CRDM). The CRDM is linked to the RCCA by a notched drive shaft mechanism. The CRDM present six grippers latch arms (Figure 2-1d) interacting with drive rods to allow the movement of the RCCA [8]. The gripper latch arms are made out of stainless steel (304) with the contact area coated by harder cobalt-based alloy (Stellite 6) [9].

a)

1 Vessel head
2 Vessel
3 fuel assembly
4 Lower internals
5 Upper internals
6 Guide tube
7 Control rod drive mechanism
8 Ventilation
9 Vessel head insulation
10 Cable bridge
11 Vessel head lifting ring
12 Vessel support
13 In-core instrumentation
14 Reactor cavity
15 Assismic rod
16 Core support plate
17 Inlet Nozzle
18 Outlet Nozzle
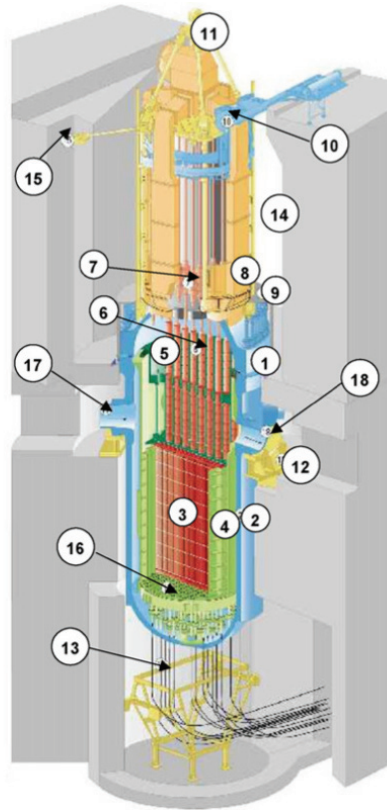
b)
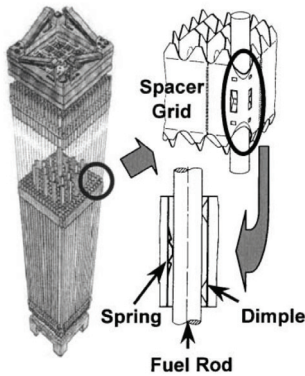
c)
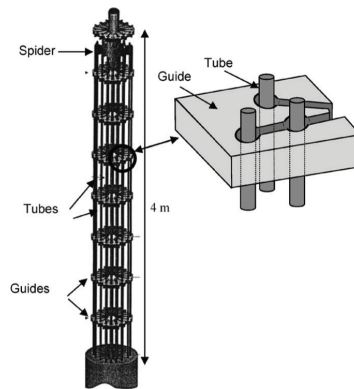
d)
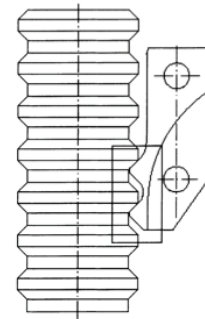
Figure 2-1 Components present in the reactor core: a) Pressure vessel schema [10], b) Fuel Assembly [6], c) Rod Cluster Control Assembly (RCCA) and d) Control Rod Drive Mechanism [9](CRDM)

The fuel assembly (Figure 2-1b) presents spacer grids that are used to hold-down the fuel rods. They have six support points (two springs and four dimples). The main function of the grids during normal reactor operation is to diminish fretting due to flow-induced vibrations and from damage when handling. The average contact pressure of the fuel rod/spring contact is approximately 91 MPa with a spring hold-down force of 13.56 N. Under these conditions the rods could suffer a bending deformation of 0.387 mm [11]. In the case of the control rods that are part of the RCCA (Figure 2-1c), they are subjected to sliding against guide cards when moving up and down as well

as to impact and fretting due to water flow induced vibrations. The obtained contact pressure in the interface control rods/guide was observed to be about 60MPa with a maximum normal load of 15N [7].

As previously exposed, the control rod drive mechanism (CRDM) is located in the upper part of the RCCA. The CRDM includes an electromagnetic latch mechanism with two main mobile parts: the gripper latch arm and the drive rod (Figure 2-1c). They are mainly used step by step in order to control the neutron flux by holding up or down the RCCA system. The step-by-step motion produces a sliding movement of ~100µm between both mobile parts. The contact pressure reaches about 150MPa [9].

2.1.3 Evidence of wear in PWR components

Unexpected wear in certain nuclear reactors was first observed in 1983 in the US and in 1986 in France. The guide cards of some rod cluster control assemblies (RCCA) presented worn areas that were supposed to appear much later. Worn areas presented cup-shaped surface patterns (Figure 1.2). Metallographic cross sections revealed that the microstructure below the surface remains intact and without strain hardening marks. The typical wear depth was observed to vary between 220 and 1000µm per year [9, 10].
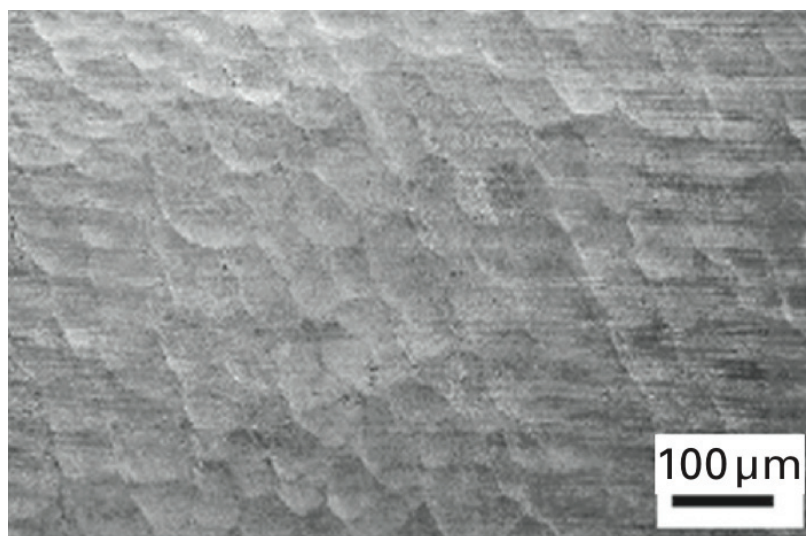
Figure 2-2 Surface of a control rod from the reactor Golfech that present the cup shaped patterns.

The specific rod/guide configuration of the RCCA system was found to critically affect the wear rate. In fact, more pronounced wear of the tube appeared at the contact spots with the edges on the guide card created by the machining paths (Figure 2-2). Rods placed in a single bore configuration wore less than when ones placed in a double bore configuration, that are in contact with more edges. Also, the water flow induced vibrations are larger in double bore configurations [12].
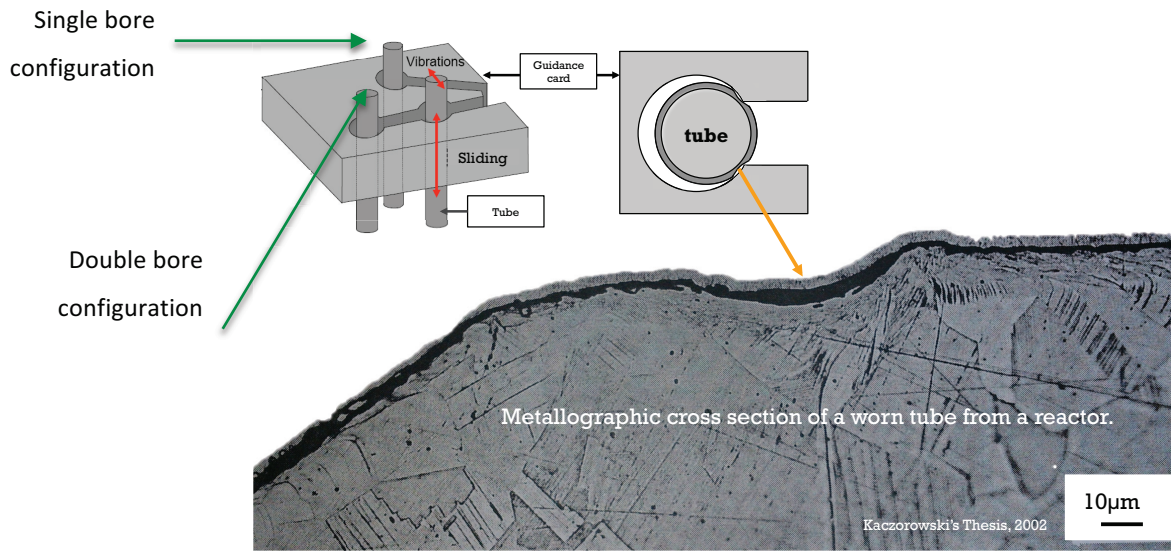
Figure 2-3 Cross section of the border of a rod from Golfech reactor [12]. Upper part (Control rod assembly with single and double bore configuration)

The zones of the rods contacting the bore edges showed, in addition to more severe wear, higher strain hardening as indicated by the presence of a larger grain refined area below the surface (Figure 2-3).

This unexpected high wear was attributed to a tribocorrosion phenomenon involving the interaction of corrosion and mechanical loading. Indeed, the guide cards and the control rods were designed to resist separately wear and corrosion but not the combined action of both [10].

Gripper latch arms also showed an unexpected high wear rate. Two wear zones were identified on these components (Figure 2-4). The zone 1 presented smooth and polished surfaces with a subsurface deformation limited to a depth of 5 µm. In contrast, Zone 2 exhibited larger mechanical damage characterized by subsurface deformation reaching depths of 20 µm and by the presence of wear debris and cracks. Nevertheless, Zone 1 suffered larger wear despite the apparently lower mechanical loading. This suggested that corrosive effects enhance material loss from Zone1.

A further indication that tribocorrosion effects play a role in determining CDRM came from the observation that wear in nuclear power plants was found to be four times larger than in accelerated bench tests [9, 13]. This discrepancy was explained by considering that the time between two successive operations of the gripper latch arms was much larger in nuclear reactors than in the bench tests. The longer latency time favored the growth by corrosion of a thicker oxide film that was removed at the successive operation. Because of this tribocorrosion mechanism, larger wear per operation cycle was generated in nuclear power plants [9].

Figure 2-4 Gripper latch arm showing the two areas where wear occurs 1) straight 2) transition zone in curved shape [9].

2.2.1 Corrosion in PWR conditions

Water constitutes an aggressive environment for most engineering metals and alloys. The reaction between the metal and the water leads to the formation of a surface metal oxide accompanied by the release of hydrogen according to Eq. (2-1).

$$Me + x\,H_2O \rightarrow MeO_x + x\,H_2 \qquad\qquad (2\text{-}1)$$

Molecular oxygen dissolved in water can further enhance the oxidation of the metal and therefore oxygen scavengers such as hydrazine are added to the water in PWR. Literature reports that parameters such as pH [14], oxygen and hydrogen concentration [15] can modify the morphology and the chemical composition of the oxides growth on stainless steel in PWR conditions. As a consequence, the properties of these oxides will also changes depending on the environment to which they are confronted.

Typically the oxide films formed in PWR conditions are several µm in thickness, i.e. much thicker that the passive films usually found in water at ambient temperature. Depending on the material, the structure of the oxide formed under PWR conditions can be complex. For example, stainless steel develops in PWR water a sandwich layer composed of an inner compact chromium rich film and an outer iron rich film sometimes covered with iron oxide crystallites [16, 17] (Figure 2-5). The presence of deposited crystallites depend on the strength of the water flow that can take away corrosion products before they can precipitate [7]. Also, corrosion products generated elsewhere in the piping system can contribute to the film build-up [5].
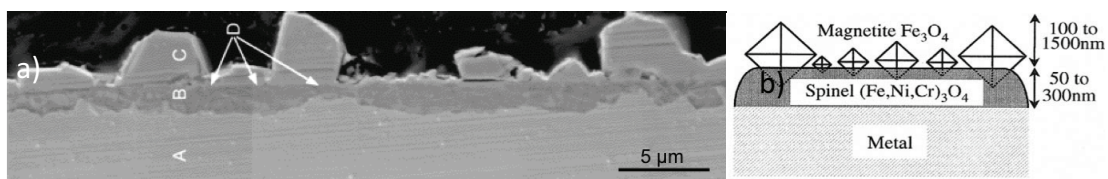
Figure 2-5 a) cross section of an oxide film layer of stainless steel 304 [18], b) Schematic cross section of the oxide layer [17].

Oxide films formed on Stellite 6 alloy are similar in structure to those formed on 304L stainless steel, a two-layer structure. The inner layer is a chromium rich layer with an X-ray diffraction structure close to $CoCr_2O_4$. The outer layer formed by precipitation, mainly of iron, has the structure of magnetite M_3O_4.

At high temperature (above 300°C) the growth rate of the oxide film (kinetics of reaction (2-1)) is limited by the diffusion of the metal ions through the oxide film from the metal/oxide interface to the oxide/water interface [19]. In fact, diffusion of cationic or anionic species is initially rapid (thin oxide film) and slows down with increasing scale thickness. High temperature enhances diffusion and therefore oxides formed in high temperature pressurized water are usually much thicker than the ones observed at room temperature.

When the oxidation reaction is controlled by the diffusion of ions (cations M^{n+} or anions O^{2-}) through the metal scale, which in turn is controlled by the chemical potential gradient as a driving force, the oxide growth follows a parabolic kinetics. Under these conditions the oxidation rate decreases with time due to the increasing diffusion distance generated by the thickening oxide. The oxidation rate in this situation is inversely proportional to the amount of oxidized metal (film thickness) and can be described with a parabolic growth law:

$$\frac{dm_s}{dt} = \frac{K_p}{m_s}$$

(2-2)

Where, K_p [$kg^2\ m^{-4}\ s^{-1}$] is the parabolic oxidation constant and m_s [kg/m^2] the mass of the formed oxide per unit of surface. When integrated with an initial mass of zero (m_s=0) at the beginning of oxidation (t_o=0) Eq. (2-2) yields Eq. (2-3).

$$m_s = \left(2K_p\right)^{1/2} t^{1/2}$$

(2-3)

The mass m_s [Kg/m^2] can be described in terms of oxide thickness d [m^2] by taking into account the surface area A [m^2] and the mass density ρ [kg/m^3] (Eq. (2-4)). Furthermore, the product of the oxide thickness and the area gives the oxide volume V [m^3] (Eq. (2-4)).

$$m_s = d \cdot \rho = \frac{V \cdot \rho}{A}$$

(2-4)

By combining Eq. (2-3) and Eq.(2-5), we obtain:

$$d = \left(2K_p\right)^{1/2} t^{1/2} \rho^{-1}$$

(2-5)

Where K_p becomes $k_p = \frac{K_p}{\rho^2}$ and correspond to the parabolic oxidation constant with unit m^2/s. By replacing Eq. (2-5) into Eq. (2-4) and using the parabolic constant k_p, we obtain the mass of the oxide in function of the oxide thickness based on the parabolic kinetics.

$$m = \left(2k_p\right)^{1/2} t^{1/2} \cdot A \cdot \rho \qquad\qquad (\,2\text{-}6\,)$$

The mass of oxide m [kg] can also be related to the quantity of electricity passing through a surface area of a metal (charge density q) using Faraday's law. The obtained current corresponds to the quantity of charge exchanged during a chemical reaction.

$$m = \frac{q \cdot A \cdot M_{mol}}{n \cdot F} \qquad\qquad (\,2\text{-}7\,)$$

Where q [C/m^2] is the charge density, A [m^2] the surface area, M$_{mol}$ [kg/mol] is the molar mass, ρ [kg/m^3] the mass density, n the charge number and F the Faraday's constant [C/mol]. By replacing the Eq. (2-6) into Eq. (2-7), the charge density can be described in terms of parabolic kinetics (Eq. (2-8))

$$q = \frac{\rho \cdot n \cdot F}{M_{mol}} \left(2k_p\right)^{1/2} t^{1/2} \qquad\qquad (\,2\text{-}8\,)$$

2.2.2 Wear

Wear was defined in the seventies [13] as a progressive removal (or displacement) of material from one body when subjected to contact and relative motion. This definition was applied for sliding or rolling motion and did not take into account the interactions of the body with the environment neither the chemical reactions happening in the contact. Under these considerations, wear can be caused by a plastic deformation at the interface but also by chemical processes.

a) Adhesive
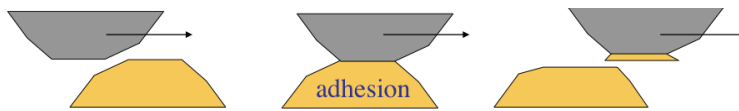
b) Abrasive
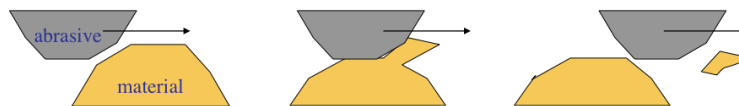
c) Fatigue
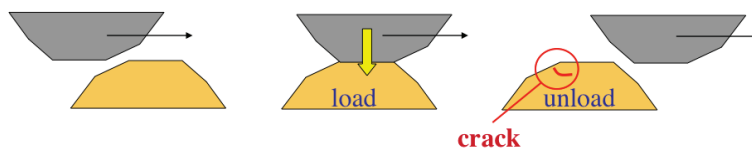
d) Tribo-chemical
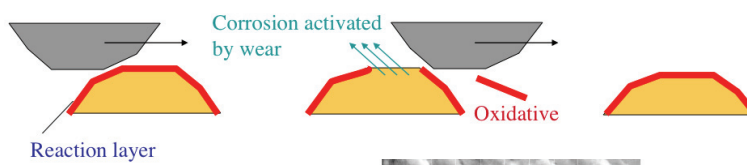
Figure 2-6 Wear mechanisms a) Adhesive wear, b) Abrasive wear, c) Fatigue wear and d) Tribo-chemical wear [13]

*Adhesive wear (*Figure 2-6*a):* occurs when a soft asperity with strong adhesion to the relative flat surface is in contact. This interaction produces a crack at the front edge of the contact and a wear particle is generated. The critical factors affecting these mechanisms are the size of the geometrical surface area, bonding forces, surface contamination [13].

*Abrasive wear (*Figure 2-6*b):* occurs when a hard surface slide against a softer surface and the hard particles remove material from the opposite surface. Abrasive wear mechanism depends then on the hardness ratio between the abrasive and the abraded material (larger than one) and on the roughness of the abrasive material. In order to describe how abrasive wear occur, three main mechanisms were proposed: plowing, cutting and fragmentations. The first one correspond when material is displaced to the sides and forming ridges. This latter does not correspond to material removal. The second one (cutting), when material is took out of the surface in form of microchips with only a little material removal and some ridges. Fragmentation occurs when material is separated from the surface by a cutting process (fracture produced by the indenter) [13].

*Fatigue wear (*Figure 2-6*c) :* is produced when local yield is generated in the subsurface when load is applied in the asperity contact. The yield zone is extended and a crack generated by the repeated rubbing process. The surface is delaminated by the crack propagation. The critical factors affecting this mechanism are the load, number of cycles, residual stress and surface roughness [13].

*Tribo-chemical wear (*Figure 2-6*d)*: Also known as oxidative wear or tribocorrosion. It occurs in presence of oxygen or other oxidized agents. It happens when an asperity moves with respect to a surface covered by an oxide film that detaches at the contact area. The bare metal corrosion is then activated and a new oxide layer forms. The critical factors affecting this mechanism are the mechanical properties of the surface, the kinetics of the reaction, kinematics and loads [13].

Regarding these mechanisms wear phenomena should be considered as a system property and not a material property. In order to describe wear depending on different parameters, several laws were developed; some of them are presented below.

Archard approach

An approach for explaining sliding wear is a theoretical analysis made by Holm and Archard (1953). They considered that technical surfaces are never perfectly smooth. Instead they are characterized by roughness and asperities. Thus, they described wear as a consequence of the contact between surface asperities (Figure 2-7). They proposed that the true contact area A_r is the sum of the

individual asperity areas. These individual areas are proportional to the normal load and the local deformation is assumed to be plastic. In fact, the normal load is maximally supported when both areas completely overlap (Figure 2-7,stage III).
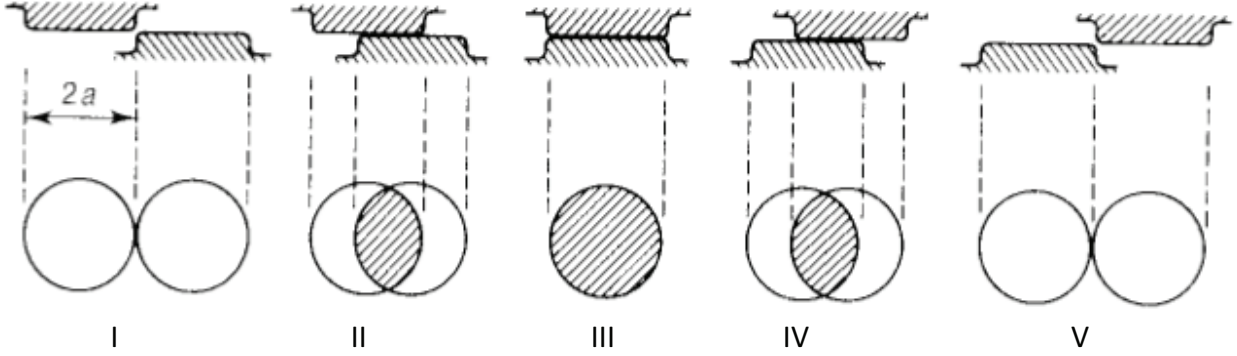
Figure 2-7 Schematic diagram of the contact evolution during the motion of two asperities where a is the radius of a circular asperity contact.

Under this condition, load variation (δF) is expressed as proportional to the flow pressure **P** and the contact area **A**. The flow pressure corresponds to the indentation hardness **H** and A_i to the area of a single particle assumed to be circular ($A_i = \pi \cdot a^2$)

$$\delta F_N = P \cdot A_i \qquad (2\text{-}9)$$

During sliding (Figure 2-7, stage IV and V), the supporting of the normal load is taken by other asperities and as a consequence a continuous creation and destruction of contact areas. The total normal load is then proportional to the sum of all the contact areas (Eq. (2-10))

$$F_N = \sum \delta F_N = H \sum A_i = H \cdot A_r \qquad (2\text{-}10)$$

Under these considerations, wear is associated to the detachment of asperities fragments produced by the continuous sliding and its volume depends on the size and number of the asperity junction. The mean volume assuming a half sphere of radius a is $\delta V = \frac{2}{3} \cdot \pi \cdot a^3$ .Not all the asperities contacts leads to wear particles, so it can be assumed that only a proportion κ detaches. The wear rate (worn volume per unit sliding distance) is then proportional to the mean volume δV and follows the relation:

$$\delta W = \frac{K \cdot \delta V}{2 \cdot a} = \frac{\kappa \cdot \pi \cdot a^2}{3} \qquad (2\text{-}11)$$

The total wear rate W due to all asperities contacts is then the contribution over the total contact area :

$$W = \sum \delta W = \frac{\kappa}{3} \sum \pi \cdot a^2 = K \cdot A_r \qquad (2\text{-}12)$$

By assembling Eq. (2-10) and (2-11), we obtain that according to Archard, the volume V per unit of sliding distance l_{sl} is proportional to the normal load F_N and the hardness of the softer material as presented on Eq. (2-13).

$$V = K \frac{F_N \cdot l_{sl}}{H} \qquad (2\text{-}13)$$

Where K is an a-dimensional wear coefficient [-]. The typical K value varies from 10^{-2} to 10^{-8} as reported by Black et al. (1993). Its numerical value depends on the material removal mechanism (abrasive, adhesive, fatigue wear, etc).

Oxidative wear

Quinn has proposed an oxidation wear mechanism involving the removal of the oxide and its regrowth [20]. The wear rate (w) is the volume per unit sliding distance and it is calculated according to the Eq. (2-14).

$$w = \frac{d \, A \, A_p}{\xi^2 \rho^2 V f^2} e^{-Q_p/RT_o} \qquad (2\text{-}14)$$

d: distance of sliding contact at an asperity, A: real contact area, A_p: Arrhenius constant, Q_p: activation energy, T_o: temperature of oxidation, R: gas constant, ξ: wear particle thickness, ρ: average density of the oxides within the critical oxide film thickness, V: speed of sliding, f: mass fraction of the oxide which is oxygen.

This mechanism has been used to explain wear in the gripper latch arms coated by Stellite [9]. The observed worn areas in this component presented a polished surface and a minimal subsurface deformation, typical characteristics of this mechanism [20].

The reformation of an oxide at a given temperature is influenced by the resting time between two successive strokes (dwell time). Longer is the dwell time thicker is the reformed oxide. The effect of this parameter was observed on Stellite coated components where wear per stroke increases when the latency time is longer [9]. Indeed, longer time intervals between two strokes allow for the growth of a thicker oxide film and thus for more material removal at the successive stroke. In contrast, Aurore tests on self-mated 304L steel showed lower wear at longer latency time [17]. As

a consequence of theses observations, the Quinn's wear mechanism based on the oxide kinetics regrowth is not sufficient to describe the overall wear behavior.

The oxide formed on the top of the metal can have different functions. It can act as a protective film against corrosion but also limits the ductility of the metal and thus promote wear [21]. Numerical simulations of sliding/impact processes occurring on stainless indicated that the presence of a thick film could reduce significantly the strain of the underlying metal [21]. However, results obtained on Norem02 are not in agreement with a mechanical protective action of the oxide film. In fact, these authors observed that wear was larger at 455K (micrometric film) than at room temperature (nanometric film). This behavior was however not observed on a Fe-Cr-C-Si alloy or on Stellite6 [22].

Regarding the observed phenomena. The role of the formed oxide can then vary depending on the material, environmental and the mechanical conditions to which it is subjected.

Tribocorrosion

Tribocorrosion damage result from the interaction of mechanical and chemical factors and is usually different from the simple addition of wear and corrosion taken separately. In fact, friction and wear modify the sensitivity of material to corrosion and conversely corrosion modifies the conditions of friction [23].

In tribocorrosion contact degradation results from the combination of mechanical wear (detachment of metal particles) and wear-accelerated corrosion due to the periodic removal of the passive film protecting the metal against the aggressive environment [23]. A schematic representation of the mechanism is presented on Figure 2-8.
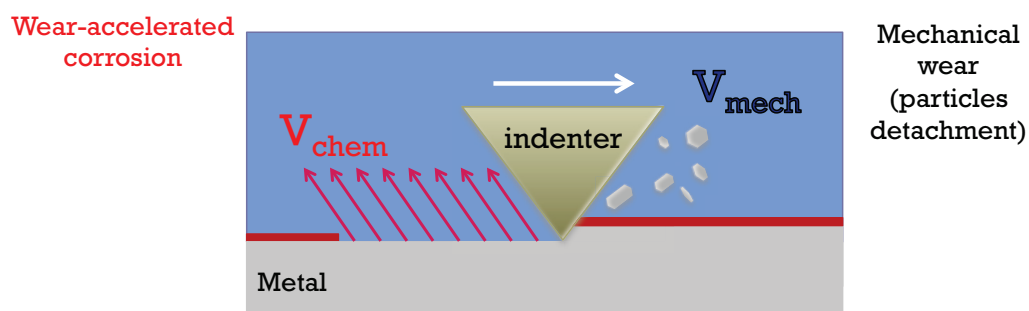
Figure 2-8 Degradation mechanism of passive metals subjected to tribocorrosion.

- ***Current modeling***

Landolt et al. [24] have proposed a model that takes into account corrosion during rubbing of an inert material against a passive metal. This model describe the behavior of the generated anodic current during rubbing due to the subsequently repair of the oxide. It is assumed that this anodic partial current is proportional to the depassivation rate (R_{dep} [m^2/s]) and the repassivation charge density (q_p [C/m^2]):

$$I_r = R_{dep} \cdot q_p \qquad (\text{2-15})$$

The R_{dep} depends on the surface morphology and the contact between the asperities and it can be defined in terms of a probability factor *k'*, the average rate of renewal of asperity contact R_n and the average asperity contact area $A_{j,av}$. The two latters can be described in terms of the geometry of the depassivated asperity. The obtained relation is presented on Eq. (2-16).

$$R_{dep} = k' \cdot R_n \cdot A_{j,av} \qquad (\text{2-16})$$

Three different cases where described in order to determine the anodic partial current I$_r$. They are schematically illustrated in Figure 2-9. The first case corresponds to the contact between two rough bodies (Figure 2-9a), the second is the contact between a hard rough indenter against a smooth surface (Figure 2-9b) and the third one is a smooth hard body sliding on rough ductile body (Figure 2-9c).
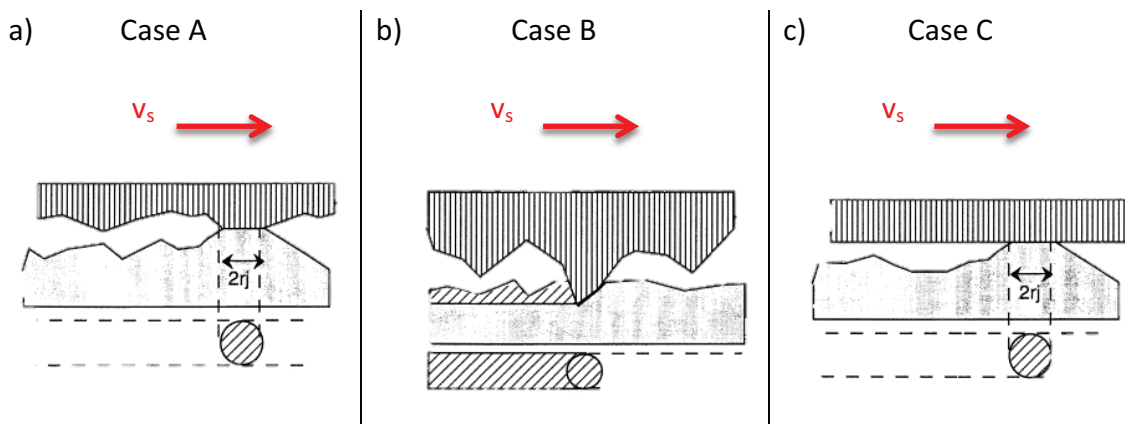
Figure 2-9 Three models for the estimation of the effect of normal force on the depassivated area: (a) Contact between two rough bodies, (b) hard rough body sliding on smooth ductile body, and (c) smooth hard body sliding on rough ductile body. The movement is on the direction of the sliding velocity v$_s$ [24].

The current generated due to the continuous passivation/depassivation of the damaged surface based on the model is described in Eq. (2-17).

$$I_r = K \cdot v_s \cdot q_P \cdot \left(\frac{F_N}{H}\right)^b \qquad\qquad (\,2\text{-}17\,)$$

Where K is the proportionality factor, v_s is the sliding velocity, Q_p the repassivation charge density, F_N the normal force, H the hardness and b a parameter that depends on the contact geometry. The parameter b varies between 0.5 and 1 depending on the case to which it is applied.

The mathematical description of the current depending the treated case and the description of the proportionalities constant is summarized on Table 2-1.

Table 2-1 Current equations depending on the model with the description of the proportionalities parameters.

Mathematical expressions of the current depending on the models		
Case A	Case B	Case C
$I_r = K_a \cdot v_s \cdot Q_p \cdot \left(\frac{F_N}{H}\right)^{0.5}$	$I_r = K_b \cdot v_s \cdot Q_p \cdot \left(\frac{F_N}{H}\right)^{0.5}$	$I_r = K_c \cdot v_s \cdot Q_p \cdot \left(\frac{F_N}{H}\right)$
$K_a = 0.89 \cdot k' \cdot n_j^{\frac{1}{2}}$	$K_b = 1.12 \ \cdot k' \cdot n_j^{\frac{1}{2}} \cdot cos\alpha$	$K_c = \dfrac{k'}{\lambda}$
k': Probability factor, n_j: number of asperities depassivated simultaneously, α: average attack angle of asperities, λ: length of the smooth body in sliding direction.		

The values of the proportionality constants as presented on Table 2-1 are dependent on the number of asperities that can be depassivated at the same time. This value being hard to evaluate, the Eq. (2-17) is commonly used for estimating the influence of electrochemical, mechanical and material properties on wear accelerated corrosion [25].

Third body concept

Godet [26] introduced third body approach in the 70s in order to describe friction and wear behavior by taking into account the screening effect of "wear debris" in dry contacts. This concept was introduced to identify the medium at the interface between two solids in contact. It was proposed that during friction between two bodies, particle detachment accumulation can generate a third body in between the two initial bodies.

Berthier [27] contribute to develop the model by introducing scale factor and dynamic interactions. The latters constitute the notion of velocity accommodation mechanisms varying along the contact and time. This approach was used as a mechanical approach (mainly on lubrication) by describing a cycle into a tribological circuit.

Descartes [28] has defined the function of the third body as being a medium that transmits the load between the two bodies while accommodating the greater part of their difference in speed. It was exposed that the stresses and displacements imposed on the contact will contribute to the particles detachments and formation of the third body. The author described the flows of the third body as is present on Figure 2-10 with 6 different flows. An internal flow Q_i, that circulates between the first and the second body. Third body is feed by external sources: particles from the environment Q_s^e and from the first body Q_s^i. Particles from the third body going out of the third body follow a external flow Q_e or re-introduced in the internal flow by flowing Q_r. Particles that are completely ejected from the contact constitutes a wear flow Q_w.
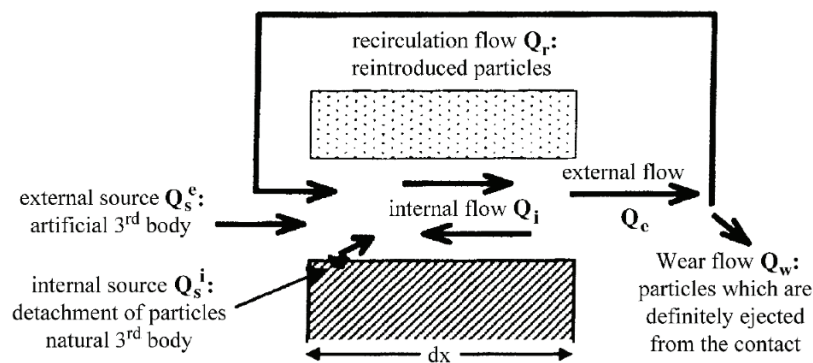
Figure 2-10 Tribological circuit for an elementary two-dimensional contact [28].

This approach was adapted by Landolt et al. [29] to describe tribocorrosion systems where the metal can passivate in presence of the electrolyte. The proposed model exposed that the contact (immersed in an electrolyte solution) has a ductile-conductive material (first body) and an inert-hard indenter counter piece (second body). The Figure 2-11 shows the different phenomena that could occurs during rubbing as proposed the authors.
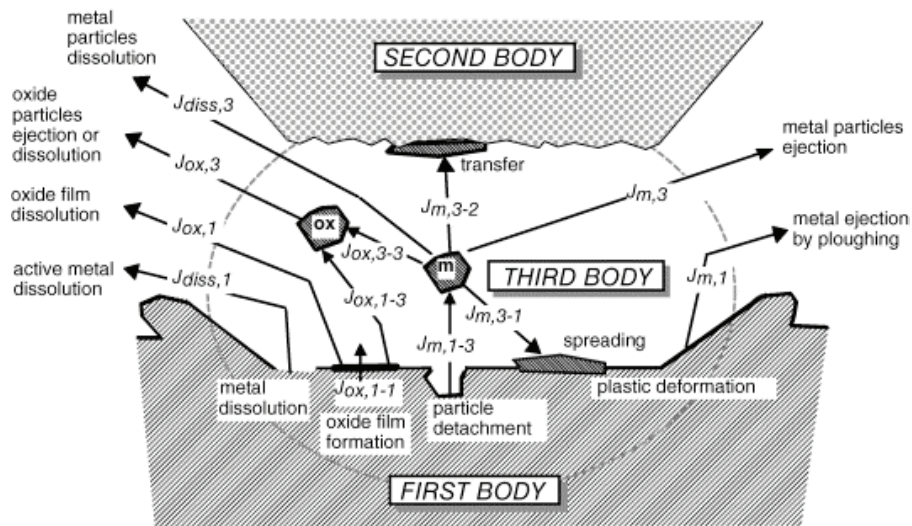
Figure 2-11 Schematic illustration of a tribocorrosion contact involving a ductile metal (first body) sliding against a hard inert counter piece (second body). Wear particles originating from the metal form a third body.

The fluxes can be described by dividing the fluxes in three different groups regarding its nature (metallic particles) and the phenomena to which they are summited (oxidation and dissolution).

METALLIC PARTICLES

$J_{m, 1-3}$: metallic wear particles torn from the first body

$J_{m,3}$: particles ejected from the third body

$J_{m,3-2}$: metallic particles form a transfer film on the 2nd body

$J_{m, 3-1}$: metallic particles can be spread on the first body

3 and 4 do not contribute to measure the total wear. The latter only corresponds to the material that leaves de contact.

OXIDATION

$J_{ox,3-3}$:   metallic third body particles (electrochemical oxidation)

$J_{ox,3-2}$:   oxidized products can be transferred to the 2nd body

$J_{ox,3-1}$:   oxidized products can be spread to the 1st body

$J_{ox,1-1}$:   surface oxide film formation

J_{ox} :   oxide film may undergo chemical dissolution releasing metal ions

$J_{ox,1-3}$:   Release of solid products from the film by forming 3rd body particles

DISSOLUTION

$J_{diss,3}$:   Metallic 3rd body particles $\rightarrow$ dissolved ions

$J_{diss,1}$:   Dissolved ions, metal dissolution

This vision of the tribocorrosion process requires the identification of the relevant mechanisms and the governing laws of the flows as well as their interdependence. However, this pre-requisite is not available at this point. And this is the main challenge for using third body model.

2.2.3   Tribological Transformed Structure

During rubbing, the metal is subjected to different mechanical solicitations that lead to plastic deformation and changes in the oxide structure. The subsurface deformation after a tribocorrosion test can present different zones as shown in Figure 2-12 [30]. The zone 1 corresponds to the un-deformed metal. The zone 2 is composed of plastically deformed and work hardened material. The deformation is more pronounced near the surface where severe plastic deformation can lead to the build up of thin grain-refined layer. In zone 3 the composition differs form the underlying metal due to mechanical mixing of surface oxide and metal.
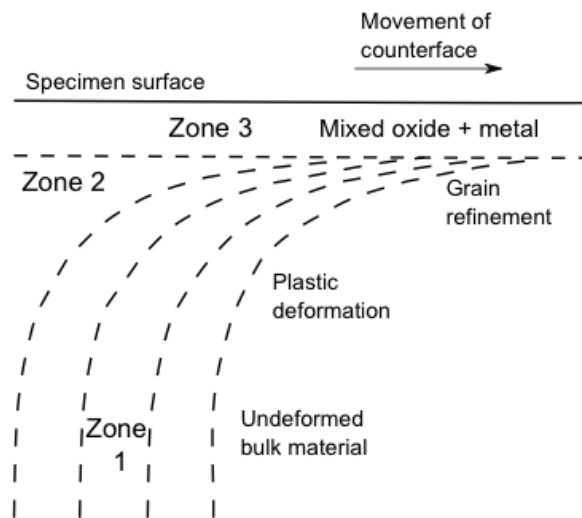
Figure 2-12 Schematic representation of different zones due to the subsurface deformation at room temperature [30].

2.3 Wear phenomena in PWR

Scratching and plastic deformation

Figure 2-13 show the observation on tests under PWR conditions using 304L alloy showed a surface covered by scratches and ridges due to the plastic deformation of the surface in contact with hard asperities (sleeve on zirconia). The ridges were observed to appear on the lateral borders but also on the frontal part of the scratch. Considering these observations, the surface degradation was attributed mainly to an abrasion wear mechanism. Tests using 316L nit (nitrided) did not show scratches similar to the 304L, in contrast the oxide was spread and compacted on the surface [31]. Moreover the author proposes that the increase of cycles could cause a mixing below the surface when rubbed more than 200 cycles. Indeed, ridges created during scratching of the metal could be detached after repeated passes and incorporated into the friction film [32]. However, the metal particles rapidly oxidize as soon as exposed to the environment during smearing of the film.
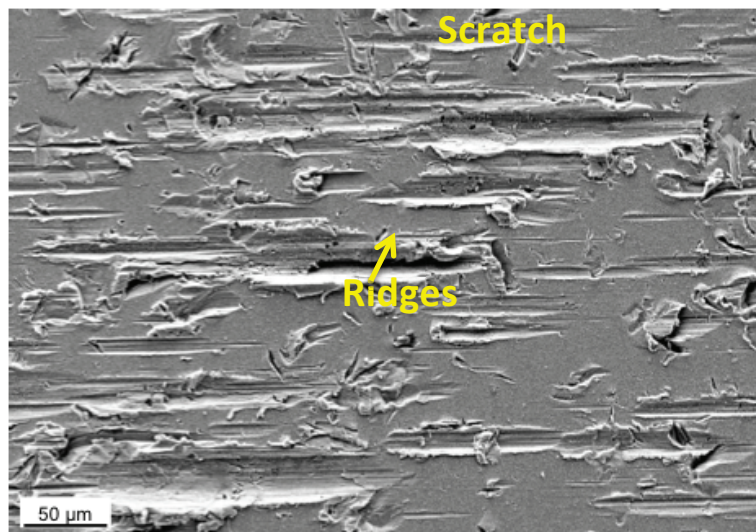
Figure 2-13 Upper view of a wear track on stainless steel 304L obtained in PWR conditions test (Tube JP4 (304L, pH7.9), 0.2V/Pt, 1N, 113 cycles).

Plastic deformation due to the cyclic rubbing under PWR conditions also showed the presence of "lamellar zones" (Figure 2-14) with a length between 30 and 60 µm and a 20-30µm width. These zones were observed on cross sections realized on the tube and sleeve samples tested under PWR conditions. They are characterized by a laminated appearance more or less marked. It is observed superposed thin layers with contrasts similar to the substrate and the oxide [31]. Only few of these zones could go up to of a length of 100µm. These zones are harder than the substrate. TEM

images showed that this area presented an austenitic phase with compatible martensitic phase. They were observed to present cracks that suggest facilitating the oxygen diffusion and giving rise to partial oxidation [31].
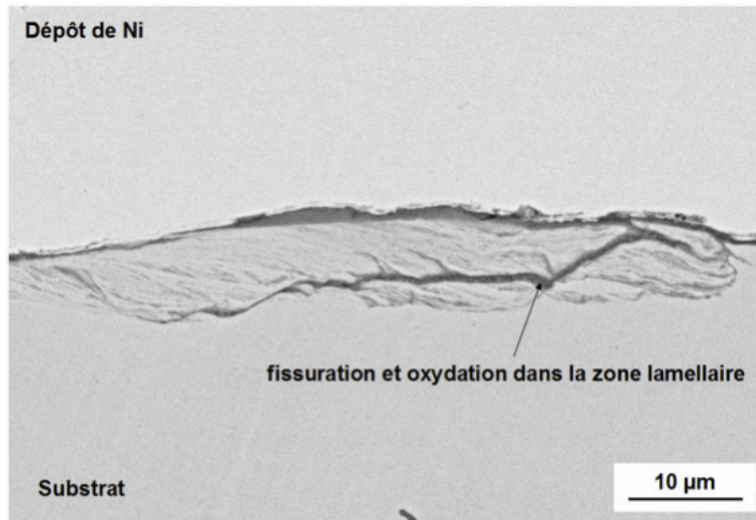
Figure 2-14 Cross section of a lamellar zone presenting cracks and partial oxidation.

Depassivation

It was observed [16] that moving the pH of pressurized water at 300°C from 6.9 to 5.2 leads to a significant increase in wear of a 304L couple. These authors used pressurized water equipped with an electrochemical set-up allowing for the control of the oxidation rate in-situ and in real time. At the onset of rubbing the anodic current was found to increase thus indicating the occurrence of oxide film removal and consequently oxidation of the bare metal exposed to water. The amount of metal oxidized during rubbing was extracted using Faraday's law from the current enhancement observed during rubbing. By comparing the electrochemical response in the investigated pH they concluded that the difference in wear could not be attributed to metal oxidation solely and thus that another mechanism than oxidative wear was controlling the overall material degradation. The authors tentatively attributed the pH effect on wear to the electrostatic repulsion forces exerted by the double layer formed on each immersed contacting surface. This repulsion forces oppose to the normal load applied to the contact and thus reduce damage. Similarly, the possibility that electrical charges produced by friction influence wear of oxide coated metals was tentatively discussed [10]. However, these phenomena are still little understood and therefore it is difficult to assess their real impact on wear.

Wear morphology with particle re-deposition

Comparing the non-rubbed surfaces at different pHs showed that the friction film can be thicker (304L, pH 6.9) or slightly thinner (304L pH 5, 316L nit pH 6.9) than the original oxide film. These indicates that pH 6.9 favors the agglomeration of detached oxide debris particles in a thicker film while this does not happen at lower pH. A reasonable explanation lies in the surface charges that develops on the surfaces and that can create repulsion forces between particles impeding agglomeration. Surfaces charges are at minimum at pH corresponding to the point of zero charge (PZC) that for iron and chromium oxide varies approximately between pH 6.5 and 8 at room temperature.

In tribocorrosion test at PWR conditions using 304L alloy was observed that the pH modifies the composition of the external oxide layer. At pH 6.9 the external oxide layer was rich in iron but at pH5 it was chromium rich. In fact, the electrostatic repulsion created by changing the solution pH could influence the sedimentation of certain debris particles inside the wear track. It was observed that crystals of the primary oxide layer are recovered by particles. In fact, the isoelectric points of chromium (Cr_2O_3) and iron oxide (Fe_2O_3) are 6.5 and 8.5 respectively [32]. This pH is near to 7.9, which induces the oxides particles that detaches from the surface to be less charged than at pH 5 and in consequence sediment in the wear track. The re-deposition phenomenon was also observed when testing 316L nit alloy under PWR conditions [31]. Figure 2-15a show that outside the wear track, single crystals with well-defined structure are observed; in contrast, inside the wear track (non-compacted zones), fines particles covers the initial structure as presented on Figure 2-15b.

OUT OF THE TRACK

INSIDE THE TRACK
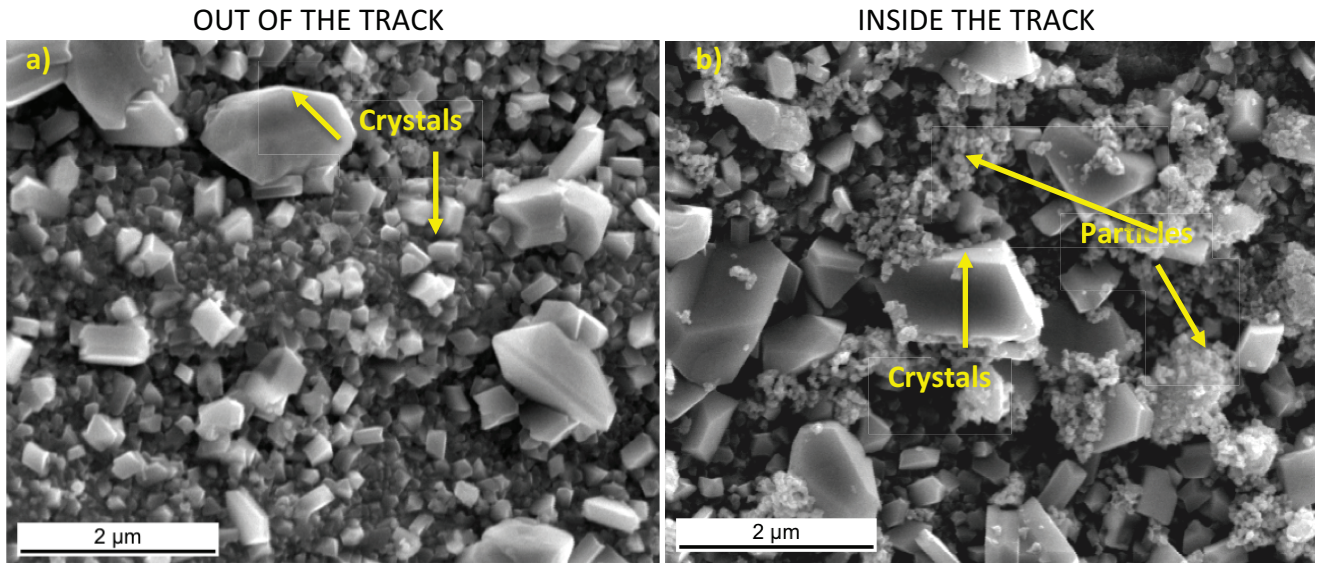
Figure 2-15 SEM images worn and un-worn surface of a tube after tribocorrosion test under PWR conditions (EC12) using 316L nit. at pH 6.9, under OCP conditions, during 70h and by applying a normal force of 10N. a) Surface structure observed out of the wear track, b) Inside the wear track inside a non-compacted zone [32].

Mechanical mixing

The mechanically mixed zone situated below the oxide layer (Figure 2-16a) showed a dynamic behavior and affect the substrate situated below. The chemical composition of the mechanical mixed zone located below the wear track, using X-ray spectrometry, on a tube cross section showed that this zone can be rich in oxygen and impoverished in iron (Figure 2-16b). A gradient of oxygen concentration was observed with the increase of the particles size. In fact, more oxygen was present on the nano-grain zone and diminishes when going to the substrate. The author describes this behavior by the superposition of thick layer of stainless steel and oxides [31].
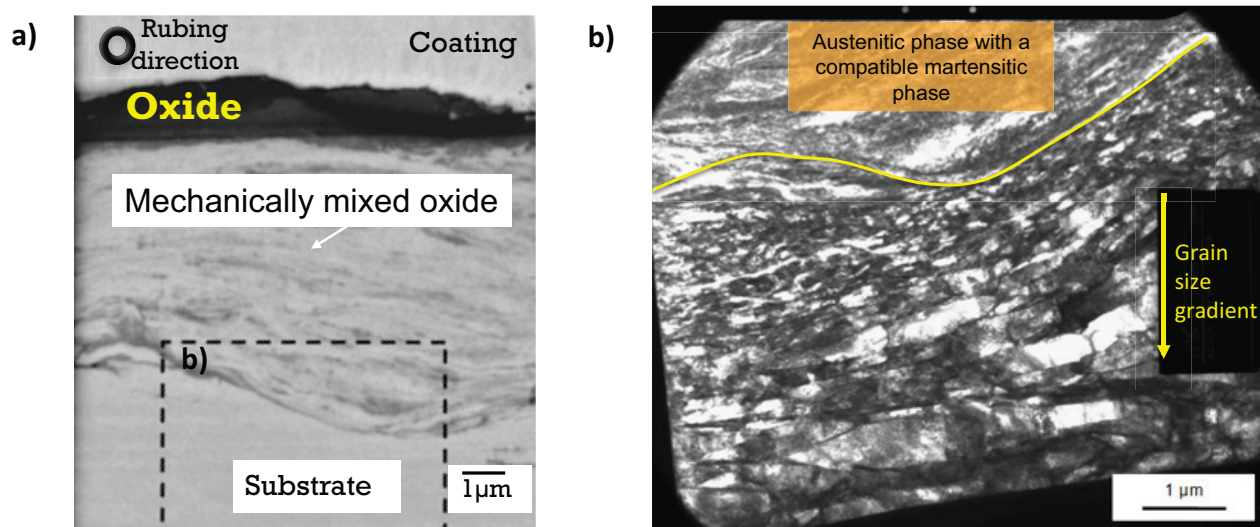
Figure 2-16 a) FIB cross section of a lamellar zone in the so-called friction film, b) SEM image of micro-refinement under the worn zone of a tube on stainless steel [31]

Mechanical mixing behavior was related to the scratching phenomenon presented previously in this section. Perret [32] proposed a mechanism (Figure 2-17) explaining the incorporation of metal in this friction film. Indeed, ridges created during scratching of the metal could be detached after repeated passes and incorporated into the friction film [32]. However, the metal particles rapidly oxidize as soon as exposed to the environment during smearing of the film.

| I. Oxide formation | II. First scratch (Ridges formation) | III. Flattening | IV. Ridge breaks and smeared |
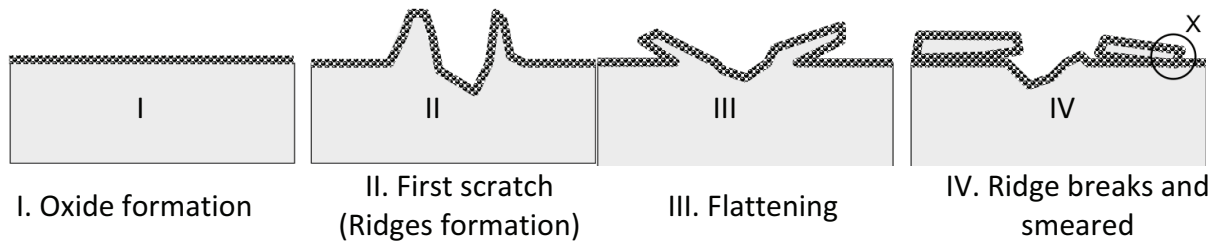
Figure 2-17 Schematic representation of the wear mechanism producing mechanical mixing on tests performed in PWR conditions [32].

Tribological Transformation Surface (TTS)

Figure 2-18 show the cross section inside the wear track after a tribocorrosion tests using 316Lnit in the rubbing direction. It presents a summary of most of the observations in this section. This image shows the presence into three zones: oxide layer on the top part, a zone with mixed oxide and metal and the third one a zone with plastic deformation. These observations are in agreement with Rigney [29] features concerning the TTS behavior. The plastic deformation area (zone 2) was observed to present a gradient of hardness in the subsurface metal layer after PWR wear of stainless steel [4, 7]. In some cases work hardening resulted in remarkable embrittlement of the metal leading to cracking during hardness indentation tests [4]. In Norem 02 (hard facing iron base and cobalt free alloys) tribologically induced martensitic transformation was observed at temperatures below 465K. Above this temperature, where thicker oxide films are formed, severe wear and large plastic deformation was observed [22].

The area with mixed oxide and metal was typically found on worn surfaces and so-called friction film [8, 31, 32]. This film corresponds in principle to the Zone 3 illustrated in Figure 2-12. They were described as being composed by compacted and smeared oxide wear debris particles. In the case of the stainless steel, the friction film was observed to be twice as hard than the substrate metal. It could present a martensitic α' phase due to work-hardening process [32].
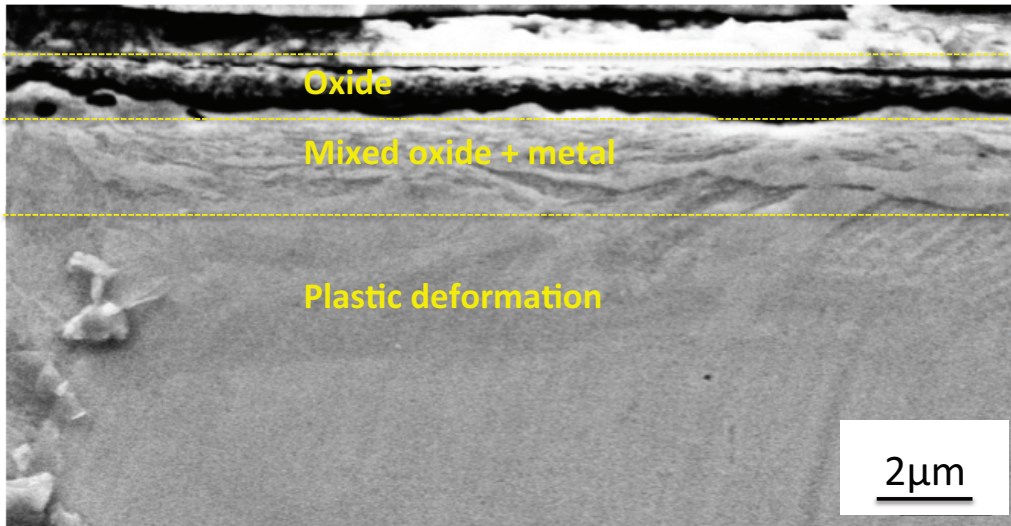
Figure 2-18 Metallographic cross section of the tube wear area in stainless steel (AISI 304L) performed under PWR conditions [31]

Evidence of subsurface deformation was also observed on Zr alloys [33] and Inconel [34] alloys. The formation of cracks and strained layers increases with the applied load on the Zr alloys [33, 35]. The brittle behavior observed was attributed to a delamination wear mechanism (platelets detachment). In the case of Inconel, the subsurface deformation was influenced by the formation of smaller cells (690TT alloy) that can easily accommodate large strains. This assumptions permit to rely the subsurface deformation to a reduction of wear comparing the 690TT alloy (smaller cells) and the 600MA alloy [34].

The observed phenomena related to the subsurface deformation have shown that the presence of friction films and/or oxide could influences the mechanical response of contacts and thus wear. Moreover, they can show the presence of different mass laws going through this so-called friction film. In consequence this behavior can be represented as a third body concept.

2.3.1 Wear models in nuclear domain

A lot of laws and parameters have already been proposed in order to explain the wear taking into account the mechanical and chemical aspect. Some of them were used in the nuclear domain. For example, in the eighties Frick et al. [36] developed a work-rate model described by a time dependence of the Archard's equation $\left(V = k \frac{F_N}{H} l\right)$ correlating wear volume *V(t)* with the work *W(t)* done during the wear process [37]. The work energy has also been used to determine the work depth in fuel rods [38] and the critical sliding conditions [31]. Ko et al. proposed that the utilization of the tangential force in a wear model concerning impact sliding was better adapted to estimate the wear behavior. Other proposed models are based on the oxidation kinetics [9, 39] or the latency time [9]. The majority of the proposed models are based on the mechanical approach (Archard's), vibrational modes (VITRAN) and corrosion (Faraday's law) separately. Some of theses models and the parameters used are exposed on the Table 2-2.

Table 2-2 Examples of wear rate models

Frick 's model [38, 40]	Wear depth model [41]	Numerical simulation [42]	Wear for CRDM [9]
Based on Archard's model	Based on Archard's model V=KQS	VITRAN (vibrational model)	Based on Faraday's law
$$\frac{dV(t)}{dt} = K_v \frac{dW(t)}{dt}$$ $$= K_v \frac{d[F(t)l(t)]}{dt}$$ $$if\ W(t) > W_o$$	$$\frac{dD(x)}{dt} = Kq(x)\frac{dS(x)}{dt}$$	$$\langle W_n \rangle = \frac{1}{t}\int_0^t f\,d$$	$$Q = i_t t$$ $$= \int i_o \left(\frac{t}{t_o}\right)^{-n} dt$$ $$= kNt^{1-n}$$
V (t) wear volume **W(t)** specific wear rate coefficient **F** force *l(t)* sliding distance K_v proportionality factor	*D(x)* wear depth *S(x)* slip distance at a specific point within the contact region. *q(x) S(x)* local dissipated energy due to the shear stress in the contact	*t* transient time *f* normal impact force, *s* rod sliding distance	*Q* Quantity of material loss per step *k* constant *N* Steps number *t* time between two steps

The observed phenomena in the literature study has shown that wear in PWR conditions involves a number of complex phenomena controlled by the interaction between mechanical and chemical effects at different length scales. A few models were proposed to quantitatively describe wear in

these conditions. However, none of them includes any combination of mechanical, chemical and material aspects. In order to develop a new approach to tribocorrosion modeling, the third body concept will be used as a tool because it integrates different phenomena by introducing flows; as is explain on the next section.

2.3.2 Mass flow on Aurore PWR conditions

Based on the third body approach, Perret [32] proposed a phenomenological wear model that describes wear process as a series of mass flows. Phenomena such as oxidation of the bare metal following a parabolic kinetics, particles deposed inside hollows (re-deposition), the thickening, compacting and mixing of the oxide permitted to construct the model observed on Figure 2-19.
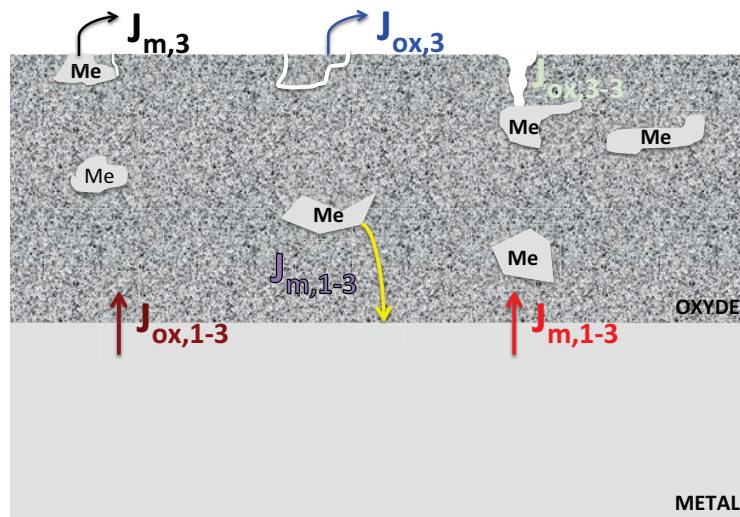
Figure 2-19 Mass flow model proposed by Perret [32]

The mass flow model proposes that the oxide could be considered as a third body and is formed by the flow $J_{ox,1-3}$ (oxidation) coming from the bare metal. Due to rubbing and the mechanical deformation observed below the surface, some local depassivation can be formed and give rise to scratches and ridges. This phenomena lead to a mixing of the oxide which could introduce metal particles on the oxide by the flow $J_{m,1-3}$ or re-introduce this particles on the bare metal following the flow $J_{m,3-1}$. The metal particles that remains on the oxide can oxidize by been in contact with water following the flow $J_{ox,3-3}$. The particle ejection from the 3rd body happens by following the flow $J_{ox,3}$ and **$J_{m,3}$** that corresponds to the oxide particles and the metal particles (already on the 3rd body) respectively.

Based on this model, wear was suggested to be limited by controlling the flows $J_{ox,3}$ and $\mathbf{J_{m,3}}$ together with the mixing of the oxide. The factors affecting the behavior of the 3rd body on this model depends on the mechanical efforts, mechanical properties of the oxide and metal, and adhesion properties between the bodies.[32]

2.4 Conclusion

The nuclear industry requires a better understanding of tribocorrosion in PWR in order to develop predictive models and test equipment allowing anticipating the lifetime of tribological components of nuclear reactors.

The literature study has shown that wear in PWR conditions involves a number of complex phenomena controlled by the interaction between mechanical and chemical effects at different length scales. A few models were proposed to quantitatively describe wear in these conditions. However, none of them includes any combination of mechanical, chemical and material aspects. The phenomenological model proposed by Perret in his thesis constitutes a promising approach for rationalizing the deterioration phenomena and the associated critical factors reported in literature. However, it does not allow quantitative predictions.

The information obtained in this chapter will permit to define the thesis objectives and the strategy to be adopted in order to model PWR tribocorrosion.

Chapter 3

Thesis objectives and strategies

3.1 Goal of the thesis

This thesis was initiated with the general aim to provide theoretical tools for assessing and anticipating sources of wear problems in nuclear reactors and for the selection of appropriate materials and designs. As seen in the previous chapter tribocorrosion phenomena in PWR are complex and involve a number of different mechanisms including various interactions between mechanical and chemical factors. The appraisal of this complexity requires a theoretical framework capable of qualitatively and quantitatively link the different deterioration mechanisms and the corresponding governing physical laws. Among the existing tribological concepts only the third body approach appears to satisfy this need. Based on this approach, J. Perret postulated that the wear process in PWR relevant conditions could be described by a number of mass flows involving material transfer from the contacting body to a third body generated during sliding (the friction film) on the body surface and subsequent transfer from the third body to the environment. Perret's attempt (Chapter 2, Figure 2-19) allowed rationalizing qualitatively many experimental observations but was unable to provide any quantitative framework.

In this perspective the goal of this thesis is to develop a quantitative model of the mass flows through the third body in an attempt to generate a theoretical framework able to predict the wear of metals operating in PWR conditions as a function of well defined parameters and by considering the interplay among different degradation phenomena.

Such an attempt implies a number of scientific challenges:

- To identify a set of mass flows corresponding to the main degradation mechanisms observed experimentally. At the initial stage, the number of considered mass flows has to be kept at a minimum and this for simplicity reasons. Nevertheless, the set should be at a later stage expanded to include other phenomena.
- To describe, for each flow, a physical law based on a mechanistic vision of the involved process. This task is particularly challenging, as some processes can hardly be isolated from the overall wear process. This is for example the case of the chemical reactivity of metal particles incorporated in the third body that can hardly be investigated as distinct process. In this case, assumptions must be taken.

- To incorporate the physical laws into a system of differential equations to be integrated into an effective wear predictive model.

Comparison with experimental observations will serve to assess the validity of the model, its limits and its improvement perspectives. Note that due to the complexity of the phenomenon the available amount of experimental results obtained under well defined, model relevant conditions are limited. The development of a third body based mass flow model of tribocorrosion in PWR is a complex task and must be seen as an iterative process where initially simple models will be refined based on ad hoc designed experiments and the introduction of more comprehensive and detailed physical laws.

3.2 Strategy

Third body approach of wear in PWR conditions

Figure 3-1 summarizes in a schematic way the experimental observations on the structure of metals surfaces after tribocorrosion in pressurized high temperature water as found in PWR. The metal surface experiences work hardening leading among others to the formation of a nano-crystalline surface layer, as typically found in tribocorrosion systems at room temperature [43-46]. Under the effect of repeated deformation the metal surface experiences mechanical mixing with the surface oxide formed by corrosion reaction. As suggested by the absence of metal on the outer oxide layer, the metal particles embedded in the oxide layer progressively oxidize in contact with water either at the oxide surface or when the oxide film locally cracks. Finally, wear occurs by detachment of oxide particles and their dispersion in the aqueous environment. Some of the detached oxide particle may nevertheless redeposit on the oxide surface. For the purpose of modeling the surface structure is divided in three sections: the liquid environment constituted by water, the friction film including the mechanically mixed layer, the oxide layer and the redeposited oxide particles, the metal substrate comprising the nano crystalline layer, the deformed subsurface and the bulk material.
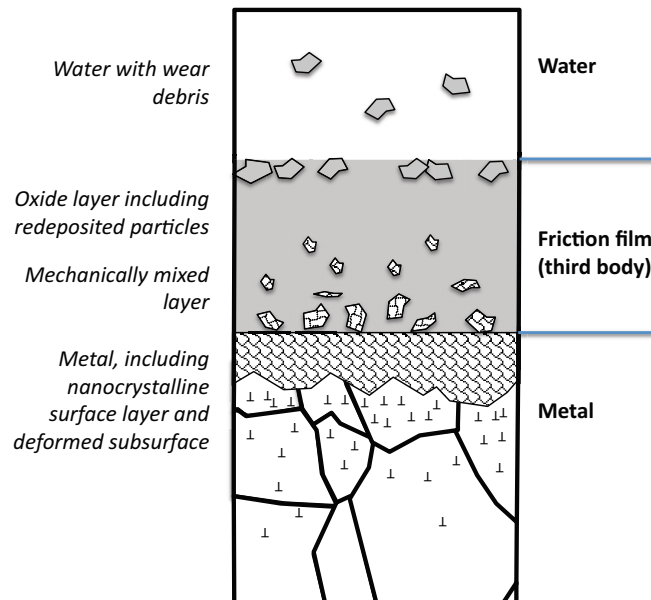
Figure 3-1 Schematic view of a summary of the experimental observations on the metal surfaces after a tribocorrosion in PWR conditions.

3.2.1   Flows and compartment description

The starting point of the present modeling attempt is the mass flow concept proposed by J. Perret encompassing source mass flows from the metal or from the water alimenting the friction film (considered as third body), internal flows accounting for third body chemical transformations and wear flows describing the definitive elimination of material from the contact. For the simplicity, only one sliding partner is assumed to wear while the counterpart is supposed to be inert.

This phenomenological model implies a number of flows described in Table 3-1

Table 3-1 Summary of flows and their terminology

Flow	Definition
ϕ_1	Metal particles entering the friction film
ϕ_2	Oxidized metal entering friction film
ϕ_3	Particle detachment from the friction film
ϕ_4	Particles re-deposition
ϕ_5	Oxidation of metal particles within the friction film

Further, in order to establish mass balances between the different flow, the physical spaces (metal, friction film, water) were associated to four different compartments (listed in Table 3-2) fed by specific mass flows (ϕ_1, ϕ_2, ϕ_3, ϕ_4 and ϕ_5).

Table 3-2 Summary of compartments and their terminology

Compartment	Definition
1	Contains mass of bulk metal
2	Contains mass of oxidized metal on the friction film
3	Contains mass of non oxidized metal in the friction film
4	Contains mass of oxidized metal in water (WEAR)

Figure 3-2 illustrates the correspondence between the physical model of the surface, the involved mass flows and the defined compartments.
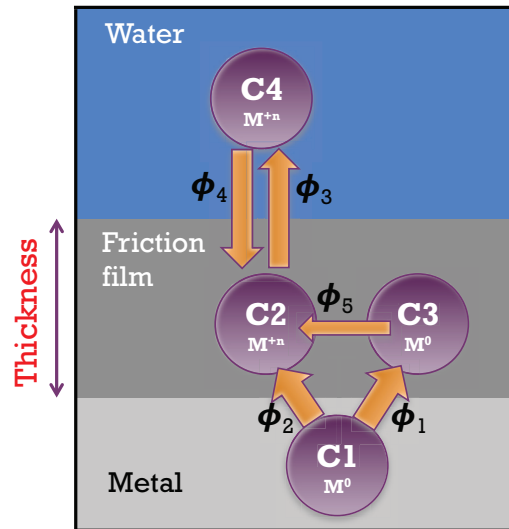
Figure 3-2 Model of the mass flow occuring in a contact operating in high temperature water

The starting point is the compartment C1; which contains particles of bare metal. From this compartment, the particles feed the friction film in two different manners: The first is transfer of metal particles. They are integrated in the friction film by mechanical action and deposited on the compartment C3 following the mass flow ϕ_1. The second manner to feed the friction film is the chemical transformation of the metal into oxide particles. The latters moves towards the compartment C2 following the specific flow ϕ_2.

The oxide particles are released from the friction film into the compartment C4 by the action of the flow ϕ_3. Some of these particles can re-enter the friction film by compaction or sedimentation from environment and thus return to C2. In this case they follow the flow ϕ_4. This approach assumes that all the particles that will be released into the water solution are oxide particles. Metallic particles located within the friction film (C3) will oxidize inside the friction film and migrate to C2 following the flow ϕ_5.

3.2.2   Thesis phasing

The thesis will be developed according three successive stages.

As a first step, the physical laws describing the different mass flows will be defined. The physical law will be established based on a mechanistic understanding of the involved phenomena, which allows identifying critical parameters. As far as possible, the physical law will be supported by experimental evidence. For example, the flows ϕ_1 and ϕ_2 can be studied in model systems operating in water solution at room temperature in absence of third bodies. The obtained results can be interpreted in term of existing mechanistic models such as described in the previous chapter. Transposing the obtained results to the PWR conditions requires considering that the third body will attenuate the stress field acting at the metal surface. Further, moving from room to high temperature requires adapting the chemical kinetics. This will be appraised by analyzing experiments carried out in a dedicated high temperature, pressurized tribocorrosion instrument (Aurore). The flow ϕ_3 is closely related to the wear rate of metal oxides and can thus be extracted, at least as a first approximation, from literature data. The flow ϕ_4 requires analysis of the possible deposition mechanisms and their modeling. The flow ϕ_5 can hardly be investigated separately and thus it description must be based on speculative hypotheses.

As a second step the physical laws needs to be assembled in a set of differential equations in order to establish mass balances in each compartment and obtain in this way a model describing the evolution of the mass flows as a function of specific physical parameters.

As a final stage the model predictions will be compared to experimental results in order to assess the validity of the developed model and to identify future improvements and design dedicated set of experiments designed to improve the model.

Chapter 4   Physical laws for ϕ_1 and ϕ_2

Wear of Stellite alloys and 304L stainless steel at low temperature

The flows ϕ_1 and ϕ_2 can be best assessed by using a model tribocorrosion system exempt of friction films as observed in PWR conditions. Such as system consisting of stellite type alloys and stainless steel rubbing in sulphuric acid at room temperature is investigated in this chapter. Under these conditions, both types of alloy form a much thinner (1-5 nm) surface oxide layer than the one observed in high temperature water (µm range).

The tribocorrosion of three different CoCr alloys (with varying carbide contents) and stainless steel was investigated using a reciprocating ball (alumina)-on-plate tribometer immersed in a 0.5M sulfuric acid solution. Alumina was chosen as a mechanical and chemical inert counter body. The alloys studied were a Stellite6 (S6) with 22% of carbides, a Stellite 21 (S21) with 6% of carbides, a Stellite 21 (LCS21) without carbides and 304L stainless steel for comparison.

Tribocorrosion tests were carried out under different applied potentials and under different loads in order to evaluate determining parameters and mechanisms. Scanning electron microscopy, laser profilometry and focused ion beam (FIB) were used for surface and sub-surface characterization of the wear tracks.

4.1 Experimental

4.1.1 Materials

Three different CoCr alloys (stellites) and one stainless steel (304L) alloy were used in electrochemical and tribocorrosion tests. The first alloys is a CoCrW alloy named also Stellite 6 (S6), the second and the third alloys are CoCrMo alloys with high (S21) and low (LCS21) carbon content. The stainless steel alloy is a 304L type. It was obtained from a control rod guidance assembly furnished by Areva [32]. The nominal compositions of the different alloys are shown in Table 4-1.

Table 4-1 Nominal composition of CoCr alloys (S6, S21, LCS21) and stainless steel 304L type.

Alloys	[wt%]									
	Co	Cr	W	Mo	C	Ni	Fe	Si	Mn	B
CoCrW (S6)	Balance	27-32	4-6	-	0.9-1.4	3	3	2	1	-
CoCrMo (S21)	Balance	26-28	-	5-7	0.20-0.25	1	0.75	1	1	0.007
Low carbon CoCrMo (LC21)	Balance	28.8	-	5.68	0.01	0.32	0.24	-	-	-
Stainless steel (304L)	-	19.9	-	0.2	-	10.6	Balance	-	2.5	-

Microstructure

Carbides were revealed on the three alloys by immersing the samples in a permanganate solution (4g KMnO4, 4g NaOH in 100ml water) during one minute, subsequently they were rinsed with distilled water and dried with compressed air. The microstructure of the S21 alloy was revealed by electrochemical etching at 6V in 8% oxalic acid and afterwards by staining using a permanganate solution (4g KMnO4, 4g NaOH in 100ml water). This treatment resulted ineffective on the same LCS21 alloy, which as expected presented no carbide staining. The structure of the S6 alloy was observed by analyzing SEM images taken with backscattered detector (BSD).

In order to determine the volume fraction of carbides the optical microscope images were treated using the ImageJ software (Developed by the National Institutes of Health NIH), which first transforms the grey scale pictures in bit mapped black/white according to a selected color

threshold (maintained identical for all pictures). Afterward the software calculates the surface fraction of the two color phases.

Optical microscope image of the S21 alloy microstructure is shown on the Figure 4-1. The observed grains have sizes varying between 1 to 10 µm in diameter. The carbides (stained using permanganate solution) appear darker on the Figure 4-1. Their size distribution is wide: large carbides with a size up to 5µm were found together with sub micrometer sized carbides. According to optical image quantification using the software ImageJ, the volume fraction of the carbides is 10%.
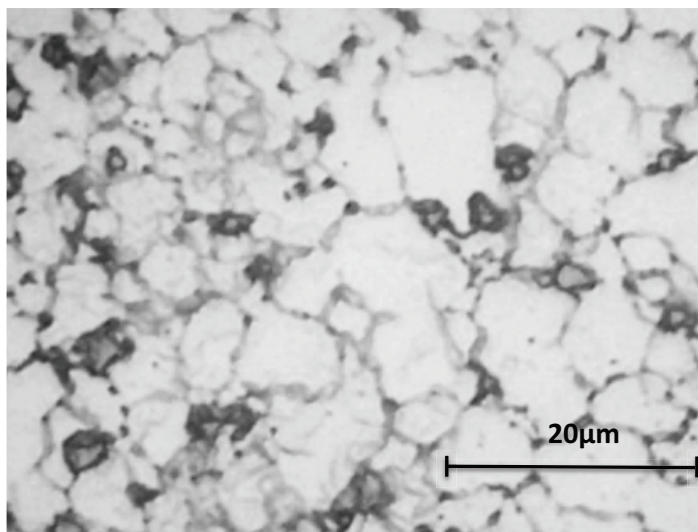
Figure 4-1 Optical microscope image presenting the alloys microstructure of S21 alloy. Electrochemical etching has been performed in oxalic acid solution and carbide staining using permanganate solution.

The Figure 4-2a shows the image obtained by using the optical microscope of the S6 alloy surface after polishing and stained in permanganate solution. The darker zones represent the carbides. This image treated by the software ImageJ revealed that the carbides volume fraction is ~29%. Most of them formed a network on the surface and only few were dispersed in the matrix. The smallest isolated carbides sizes are in the sub micrometer range.

The Figure 4-2b shows an SEM image using backscattered detector (BSD) of the S6 alloy surface. It was observed that the carbides present two different phases. EDS analysis showed that the whiter zones corresponds to a Tungsten rich phase and the darker to a Chromium rich phase. The W-rich phase act as bridges between the Cr-rich phases forming thus elongated carbides agglomerates. Few of them are randomly isolated on the matrix, their size being in the micrometer range. Image

analysis (Software ImageJ) showed that the Cr-rich phase and the W-rich phase covers ~21-22% and ~2-3% of the surface respectively.

Similar microstructures were observed in previous studies concerning cast Stellite 6 alloy [[47]]. In contrast no W-rich phases were observed on HIPed alloys; this behavior was attributed to dissolution of the W-phase phase on the matrix. Therefore the formation of W-rich phases on Stellite 6 alloys is directly related to manufacturing processes [48].
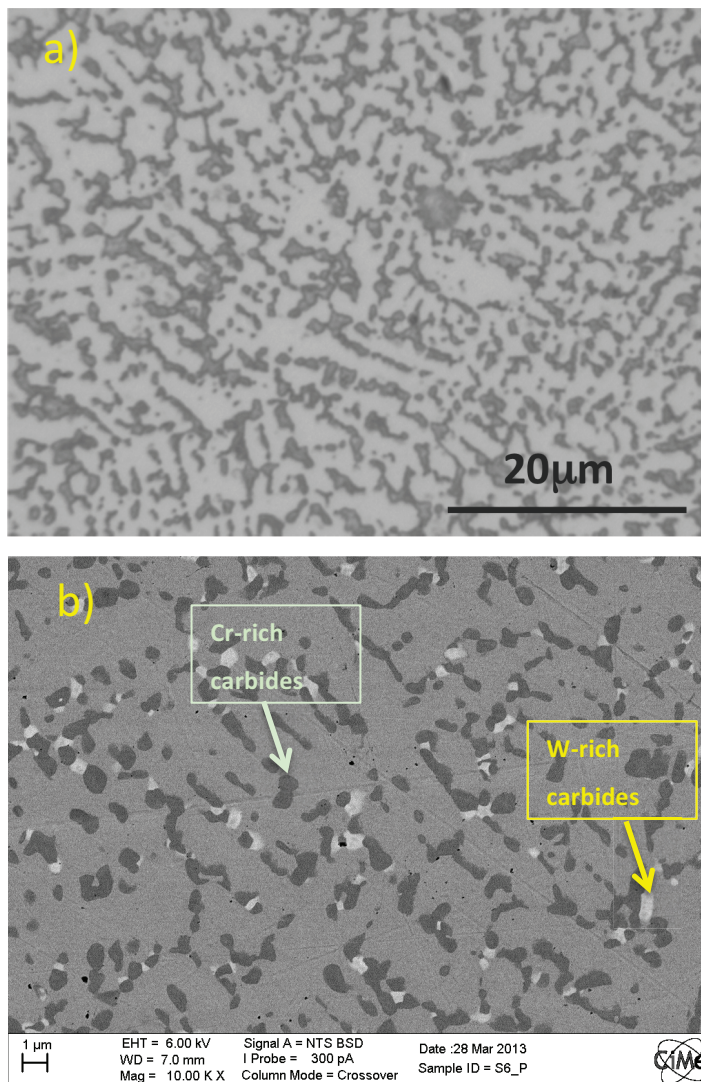
Figure 4-2 Images of the surface of the S6 alloy using a) optical microscope and b) backscattered detector (BSD) on SEM.

The microstructure of the stainless was analyzed in a previous studies using electrochemical etching [32]. The obtained metallographic section (Figure 4-3) shows that twined austenitic grains mainly compose the structure of the 304L stainless steel.
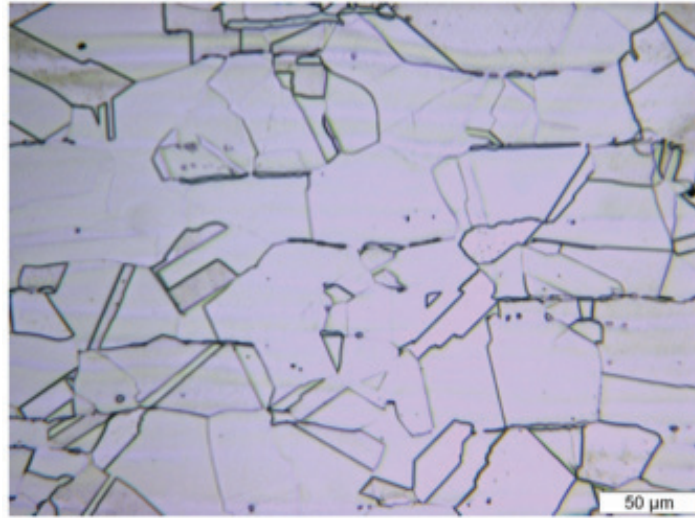
Figure 4-3 Microstructure of the 304L alloy. Its microstructure was revealed using electrochemical etching. Data from [32]

4.1.2 Tribometer

The reciprocating pin-on-plate tribometer shown in Figure 4-4 was used for tribocorrosion tests. The back and forth movement is obtained by a linear motor ALS that is driven by an Aerotech's Soloist device controlling the amplitude and the velocity of the displacement and the dwell time at direction reversal during reciprocating motion.

A PP electrochemical cell is fixed over the motor. The three-electrode system is composed of a reference electrode of mercury sulfate electrode (MSE 0.658 vs. NHE).

Counter electrode *(2)* : a platinum wire in spires that is placed around the sample.

Work electrode *(3)*: sample

The electrodes are connected to a Bank Wenking LB 95L potentiostat.
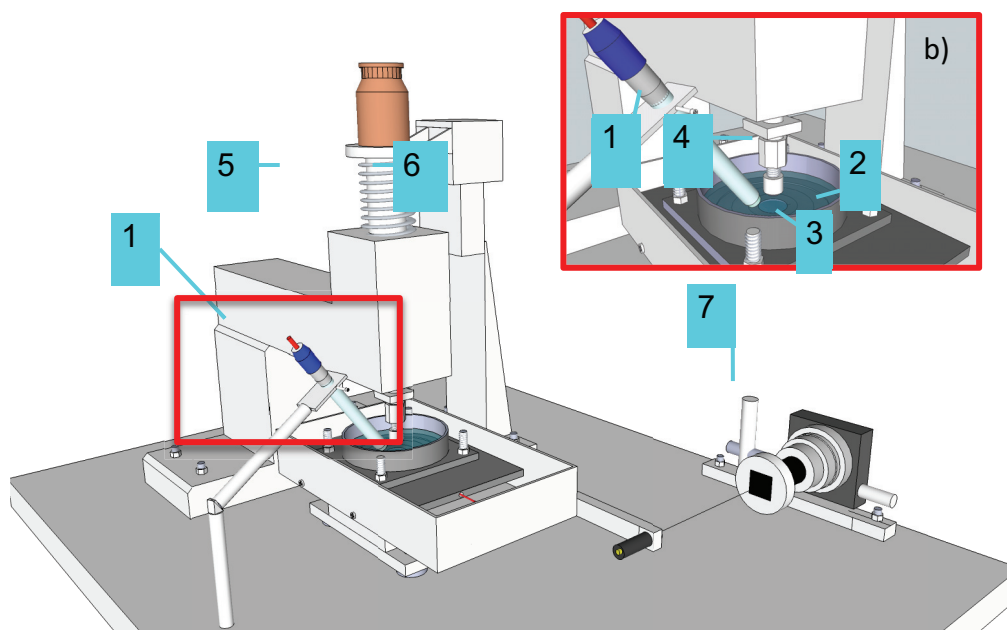
Figure 4-4 Tribometer a) 3D view. b) Specific view of the electrochemical cell: (1) Reference electrode, (2) Counter electrode, (3) Work electrode, (4) Quartz force sensor, (5) Spring, (6) Z-displacement captor, (7) Position sensitive device PSD.

The alumina ball fixed to a 3-component force sensor KISTLER 9251 *(4),* which is fixed on a vertically mounted shaft held by a linear ball bearing. This quartz force sensor permits to measure the orthogonal components of a dynamic or quasi-static force emitting an electrostatic signal proportional to the acting force. The load is applied on the other end of the shaft by using appropriate dead weights. The vertical position of the shaft is maintained by a spring *(5)* (constant

2.4 N/mm) placed around it that compensate shaft's weight and allows thus applying smaller forces.

The table displacement is monitored for control purposes through a laser diode coupled with a position sensitive device PSD (Hamamatsu) *(7)*.

The electrochemical (current, potential), force (normal force, friction force) and displacement (x, z) values are continuously monitored at a sampling rate of 1 kSample/s and treated by an acquisition system based on a analog/digital board installed in a personal computer (PC) and controlled by a home developed software based on Labview.

The data acquisition software treated the data in two different ways: transient and mean values. *Transient* were recorded by continuously monitoring the different parameters during a single back and forth cycles with a frequency of 1kSample/second. Every minute the current transient was saved on the PC hard disk. *Mean values* were calculated as average value of each monitored transient (typically every second) and continuously saved as a function of time on the PC hard disk.

4.1.3 Tribocorrosion test

Sample preparation

The samples were polished in water using SiC paper from 500-mesh up to 4000-mesh. Final polishing was performed using diamond particles of 1µm (Struers lubricant). The obtained surfaces were ultrasonically cleaned in ethanol during five minutes and then rinsed in distilled water and dried using oil free compressed air.

Tribocorrosion tests were conducted in a 0.5 M H_2SO_4 solution. The experimental parameters tested were the normal force (5.8, 11.7 or 17.5 N), the applied potential (-1.5 or 0 V_{MSE}) and the dwell time (0.25 or 0.75 s). In all experiments the stroke length and the sliding velocity were kept constant at 5mm and 20 mm/s respectively (corresponding to an oscillation frequency of 1 Hz). Each test was performed two times using new alumina balls in order to evaluate reproducibility.

The elastic stresses generated between the alumina ball and the sample surface were calculated using Hertz theory and listed in the Table 4-2. The average contact pressure largely exceeds the yield stress of this type of alloy (between 540 and 750 MPa depending on Stellite type). Thus the contact is expected to behave plastically at least at the beginning of the test.

Table 4-2 Hertz analysis of the alumina/CoCrMo contact

Force [N]	E' [GPa]	P_{moy} [MPa]	P_{max} [MPa]	τ_{max} [MPa]	δ [µm]
5.8	312	964	1446	482	0.64
11.7	312	1218	1828	609	1.02
17.5	312	1393	2090	697	1.33

E' :   Effective Young's Modulus P_{moy}: mean contact pressure

P_{max}: maximum contact pressure τ_{max} : maximum shear stress

∂:   indentation

Acquisition protocol

Three types of protocols were performed depending on the applied potential. They are illustrated in Table 4-3.

Table 4-3 Protocol of the tribocorrosion test depending on the domain of the applied potential

Cathodic potential						
	Cathodic cleaning	Stabilization	Pre-polarisation		Movement	Stand-by
Time [min]	5	5	3	2	30 (0.25s dwell time, 1800 cycles) 3 (0.25s dwell time, 180cycles)	3
E [V]	-1.5	OCP	-1.5			
F_N [N]	-	-	-		5.8N or 11.7N	

Passive domain						
	Cathodic cleaning	Stabilization	Pre-polarisation		Movement	Stand-by
Time [min]	5	5	8	2	30 (0.25s dwell time) or 60 (0.75s dwell time)	3
E [V]	-1.5	OCP	0			
F_N [N]	-	-	-		1.09, 5.8, 11.7 or 17.5	

Open circuit potential						
	Cathodic cleaning	Stabilization	Load application		Movement	Stand-by
Time [min]	5	5	3	2	30 (0.25s dwell time) or 60 (0.75s dwell time)	3
E [V]	-1.5	OCP				
F_N [N]	-		11.7			

Experiments start by a cathodic cleaning at a potential of -1.5V$_{MSE}$. Afterwards the sample is kept for 5 minutes without any polarization in order to stabilize the OCP (open circuit potential). This procedure is supposed to yield the same initial surface state for all samples independently on possible surface contaminations occurring during storage or mounting. The following steps varies depending on applied potential as follows:

Tests at cathodic potentials: after the stabilization at OCP, the potential of -1.5 V$_{MSE}$ is applied. After 3 minutes the ball is set in contact with the CoCrMo disk. After 2 more minutes motion is activated for the given number of cycles (180 or 1800 cycles depending on test corresponding to 3 or 30 minutes duration for a constant dwell time of 0.25 s). After the motor has completed the requested number of cycles the sample is left under applied potential for 3 more minutes after

which the ball is lifted, the liquid removed and the sample is rinsed with distilled water, dried using compressed air, and finally disassembled.

Tests at passive potentials: after the stabilization at OCP, the potential of 0 V_{MSE} is applied. After 8 minutes the ball is set in contact with the CoCrMo disk. After 2 more minutes motion is activated for 1800 cycles (corresponding to 30 or 60 minutes duration for dwell times of 0.25 or 0.75 s, respectively). After the motor has completed the requested number of cycles the same procedure as described for the cathodic potential is followed.

Tests at Open circuit potential: the potential is left free during 3 minutes and then the ball is set in contact with the disk. After 2 more minutes, motion is activated. After 1800 cycles the same procedure as described for the cathodic potential is followed.

4.2 Electrochemical behavior

4.2.1 Polarization behavior

The potentiodynamics curves of the three CoCr alloys and the stainless steel 304L in a 0.5M H_2SO_4 solution are shown in the Figure 4-5. The corrosion potential of the alloys is similar and remains between -0.7 and -0.8V. Three different domains can be distinguished: The cathodic domain includes potentials below -0.8V. The current in this domain is due to the reduction of protons and in a lesser extent dissolved oxygen. The passivation plateau extends from -0.5V to 0.3V. The transpassive domain is observed above -0.4V. In this region, the current increases with the applied potential due to water oxidation and alloy dissolution. The latter on CoCr alloys is related to the oxidation of Cr^{3+} species into soluble Cr^{6+} [49, 50].

No active peaks are observed in S21 and LCS21 potentiodynamic curves. The S6 alloy and 304L exhibit an active/passive transition around -0.7V. The passive domain is smaller for the S6 and LCS21 compared to the S21 and 304L alloys.
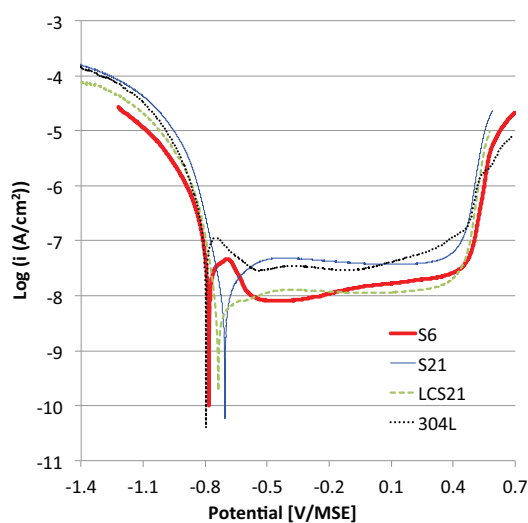
Figure 4-5 Polarization curves of the CoCr alloys S6, S21, LCS21 and 304L stainless steel in a 0.5M H_2SO_4 solution. Sweep rate is 2 mV/s.

4.2.2 Passivation transients

The Figure 4-6 shows the passivation transient of three different CoCr alloys and 304L stainless steel in 0.5M H_2SO_4 solution. The current decreases exponentially with time due to the formation and growth of the passive film. This behavior is typical for metal passivation [51, 52] and it was previously reported for CoCrMo alloys [53, 54] and stainless steel [55].

The shape of the transients recorded in sulfuric acid solution indicates that CoCr alloys passivate faster than 304L stainless steel. The current peak is higher in the case of 304L with respect to the CoCr alloys.
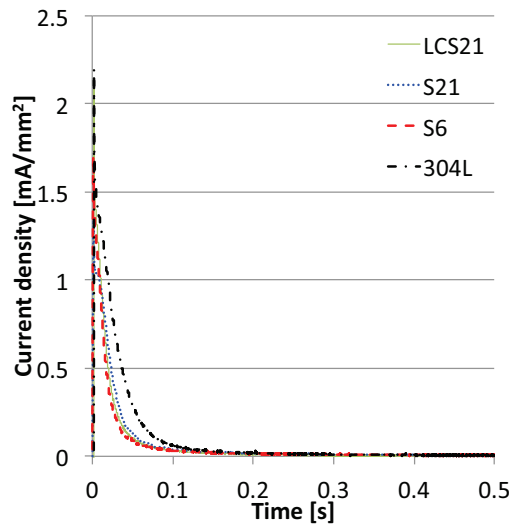
Figure 4-6 Passivation transients of the stationary Stellite 6 (S6), Stellite 21 (S21), low carbon Stellite 21 (LCS21) alloys and 304L stainless steel measured in 0.5M H2SO4 solution. Potential is switched from -1.5V up to 0V.

The passivation transients were used to calculate the passivation charge density Q_p in order to determine the amount of metal that is oxidized when forming a passive film. The values were calculated by integrating the current density from 0.003s (first measured point after the potential step) up to 0.5s [51]. Three experiments at 0V for each alloy were performed. In the case of the 304L alloy, two potentials were performed, -0.25V and -0V. The obtained charge densities are presented on Table 4-4. It is observed that passivation charges are similar for CoCr alloys where the low carbon CoCr alloy (LCS21) is the lowest. Higher values are observed for 304L alloy on both passive potentials, -0.25V and 0V.

Table 4-4 Passivation charge densities in 0.5M H_2SO_4 solution.

Alloy	Potential [V]	Passivation charge Q_p [mC/cm^2]
S6	0	3.11 ± 0.06
S21	0	3.55 ± 0.04
LC S21	0	2.92 ± 0.06
304L	0	5.40 ± 0.04
304L	-0.25	5.21 ± 0.37

4.3 Tribocorrosion behavior

4.3.1 Total wear volume:

Profilometry using a non-contact scanning laser UBM Telefokus apparatus (10nm vertical resolution, 1 μm lateral resolution) was used to characterize the wear track geometry. For this 3 scans across the wear track (perpendicular to the sliding direction) were measured on each sample. Typically, a profilometer scan can exhibit two distinct wear features (Figure 4-7): the track formed by removed material and ridges formed by metal displaced by plastic deformation during sliding. The track (V_{track}) and the ridges volume (V^b) can be determined from the cross section profiles as follows. The perpendicular area of the track (A_{track}) showed in the Figure 4-7 is calculated by integration along the track width.
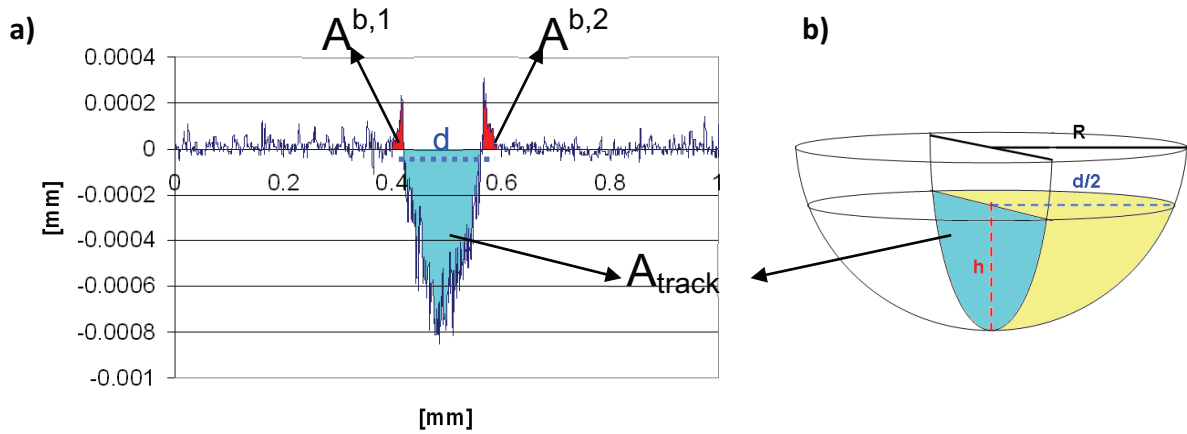
Figure 4-7 Different areas taken in account for the calculation of the wear track and ridges volume. a) profilometer trace, b) estimation of the track border for the volume cap calculation.

The obtained area is multiplied by the stroke amplitude (5mm) to obtain the $V_{track,1}$. The complete track volume should also consider the hemicycles formed at the ends of the strokes. For this, the end of the track has been estimated as a perfect geometrical half cap (Figure 4-7b), so a complete cap is formed taking in count the two ends. Its volume is calculated by Eq. (4-1).

$$V_{cap} = \frac{\pi}{3} \cdot (3R - h) \qquad\qquad R = \frac{\left(d/2\right)^2 + h^2}{2 \cdot h} \qquad\qquad \text{(4-1)}$$

Then the track volume (V_{track}) is defined as:

$$V_{track} = \left(A_{track,1} \cdot 5mm\right) + V_{cap} \qquad\qquad \text{(4-2)}$$

The area of the ridges (A^{ridges}) observed outside of the track (**Figure 4-7**) are integrated over 0.1mm from the border of the track. The additions of both areas correspond to $A^{ridges,1\&2}$. The ridges are assumed to go all around the wear track and their volume is calculated in two parts. The first part corresponds to the length of the track (5mm) and the second to the hemicycles at the end of the track ($V^{ridges,3}$). The distance around the border will corresponds to a semi-circumference of a radius d/2 (**Figure 4-7b**). The obtained ridges volume is calculated as:

$$V^{ridges} = \left(\left(A^{ridge,1} + A^{ridge,2}\right) \cdot 5mm\right) + \left(A^{ridge} \cdot \pi \cdot \frac{d}{4}\right) \qquad \text{(4-3)}$$

It was observed that the S6 alloy (15% of carbides) present the smaller wear track profile. In contrast, the largest wear track on the CoCr alloys corresponds to the LCS21 alloy, which corresponds to the alloy with no carbides, and 304L. Both alloys presented large ridges compared to S6 alloy.

In the Figure 4-8 is presented characteristic wear track profiles obtained for the three CoCr alloys and the stainless steel alloy (304L) at the same normal load (11.7N). Total wear volumes were calculated taking into account the area of the cross section, the sliding distance and the hemicycles formed at the end of the track.
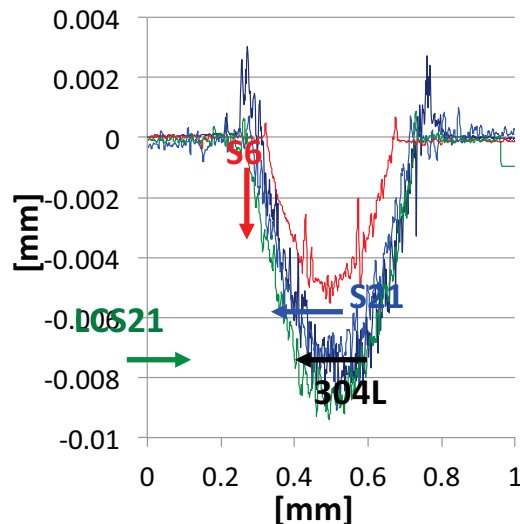
Figure 4-8 Profilometer cross section scans of wear tracks formed at 0V (passive potential) at 11.7N.

4.3.2 Chemical wear volume

The chemical wear volume, that, together with mechanical wear, contributes to overall degradation of the rubbing area, can be extracted from the average current I_{mean} as plotted in Figure 4-9.
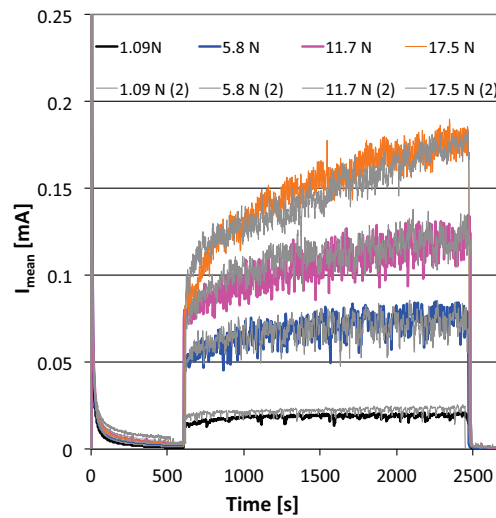
Figure 4-9 Evolution of the current with time during an experiment at passive potential (0 V) at different loads. Results of two independent tests are plotted for each load.

For extract this information the procedure described next has been used. First the excess current I_r was determined by subtracting to the value of the current I_{mean} averaged over the rubbing period the average value of the current values measured just before rubbing onset and 60 s after rubbing end [51]. This calculation allows eliminating the contribution to the current from the area outside of the wear track. According to the Faraday's law (Eq. **(4-4)**) the excess of current produced by rubbing at passive potential corresponds to an equivalent metal volume (V_{chem}) that was oxidized.

$$V_{chem} = \frac{I_r \cdot t_{rub} \cdot M_{mol}}{n \cdot F \cdot \rho}$$

(4-4)

where, I_r is the current excess, t_{rub} is the rubbing time, M_{mol} is the molar mass in g/mol, n the charge number, ρ density in g/cm³ and F the Faraday's constant.

The charge number is calculated from the molar ratio of the main alloy elements. The elements considered for the CoCr alloys were the Co, Cr and Mo(S21, LCS21)/W(S6). In the case of the 304L, the oxidized elements are the Fe, Cr and Ni [19]. If the elements present two valences, their

average value is used. The data corresponding molar mass, density and charge number of the alloys is presented on Table 4-5.

Table 4-5 Table of alloys characteristics, the charge number and the valences of the elements taken into account for charge number calculation.

Alloy	Molar mass [g/mol]	ρ [g/cm^3]	n [-]	Average value of the valences
LCS21	59.02	8.33	2.52	Co +2, Cr +3, Mo +5 (+4-+6)
S21	58.80	8.33	2.37	Co +2, Cr +3, Mo +5 (+4-+6)
S6	61.84	8.44	2.54	Co +2, Cr +3, W +5 (+4-+6)
304L	55.44	7.86	2.80	Fe +3, Cr +3, Ni +2

The mechanical wear volume is calculated as the difference between the total and chemical wear volume. The numerical values corresponding to the wear track volume (V_{track}) are presented on Table 4-6.

Table 4-6 Summary of the results extracted from tribocorrosion tests performed at OV and -0.25V (304L).

Alloy	Force [N]	COF [-]	$V_{track}*10^{-3}$ [mm^3]	$V_{chem}*10^{-3}$ [mm^3]	$V_{mech}*10^{-3}$ [mm^3]	Hardness Inside [HV]	Hardness Outside [HV]
S6	5.8	0.21 ± 0.01	3.30 ± 0.25	2.50	0.80	920 ± 35	670 ± 12
		0.22 ± 0.01	3.63 ± 0.06	2.59	1.04	875 ± 50	668 ± 9
	11.7	0.24 ± 0.02	5.5 ± 0.22	3.83	1.66	852 ± 10	688 ± 91
		0.23 ± 0.02	5.87 ± 0.32	3.76	2.11	1012 ± 65	743 ± 144
	17.5	0.24 ± 0.01	6.90 ± 0.31	4.75	2.15	975 ± 52	750 ± 30
		0.24 ± 0.01	7.05 ± 0.20	4.79	2.26	895 ± 63	712 ± 86
S21	1.09	0.20 ± 0.01	1.33 ± 0.04	0.90	0.43	663 ± 17	594 ± 22
		0.22 ± 0.02	1.43 ± 0.07	1.05	0.38	675 ± 33	555 ± 16
	5.8	0.27 ± 0.01	6.56 ± 0.12	3.95	2.61	781 ± 21	592 ± 4
		0.28 ± 0.02	6.67 ± 1.78	4.00	2.67	803 ± 34	538 ± 15
	11.7	0.25 ± 0.01	10.16 ± 0.36	6.10	3.13	789 ± 92	554 ± 6
		0.26 ± 0.01	9.80 ± 0.28	6.47	3.33	780 ± 65	579 ± 6
	17.5	0.25 ± 0.01	15.61 ± 0.99	8.60	7.01	771 ± 116	597 ± 10
		0.28 ± 0.02	17.69 ± 1.58	8.31	9.38	751 ± 45	588 ± 20
LC S21	5.8	0.23 ±0.01	7.75 ± 0.30	3.89	3.86	848 ± 78	462 ± 15
		0.25 ± 0.01	7.59 ± 0.15	3.87	3.72	811 ± 52	446 ± 23
	11.7	0.21 ± 0.01	11.79 ± 0.89	6.10	5.86	850± 56	496 ± 38
		0.23 ± 0.01	12.15 ± 1.15	6.13	6.05	882 ± 21	473 ± 52
304L	11.7	0.28 ± 0.01	12.13 ± 0.47	6.85	5.28	398 ± 20	180 ± 20
		0.29 ± 0.01	12.57 ± 0.84	6.71	5.86	352 ± 39	174 ± 5
304L -0.25V	2.7	0.22±0.01	4.74 ±0.41	2.96	1.79	304 ± 16	188 ± 25
		0.19 ±0.02	4.31 ± 0.14	2.72	1.64	266 ± 9	147 ± 8
	5.8	0.30 ± 0.01	9.13 ± 0.52	5.66	3.47	350 ± 52	166 ± 2
		0.29 ± 0.01	9.06 ± 0.25	5.53	3.53	370 ± 18	149 ± 9
	11.7	0.26 ± 0.01	19.49 ± 1.62	11.52	8.02	330 ± 8	168 ± 4
		0.27 ± 0.01	19.47 ± 0.51	11.25	8.10	365 ± 16	143 ± 11

4.3.3   Wear topography

The Figure 4-10 show the different patterns observed inside of the wear track for the three alloys by using high resolution SEM microscope.

The Figure 4-10**a** show the wear scar of Stellite 6, it is observed that the surface is flat and few marked stripes can be distinguished. Most of the debris observed was few nanometers in size. Bigger particles measuring around 1µm were rarely observed. Carbides were clearly visible. In few places, they start to de-bond **(#1)** but most of them seems to be pull into the matrix (Figure 4-10**a**).

The Figure 4-10**b** shows the wear scar of the Stellite 21 alloy. The surface presents marked stripes on the rubbing direction. A large quantity of debris particles is observed with respect to the Stellite 6 alloy. The debris particles size is in the range of few nanometers. Particle agglomerates were observed randomly on the surface **(#2)**. Carbides were clearly distinguished.

The Figure 4-10**c** presents a surface with more stripes compared to Stellite 21 (Figure 4-10**b**). It was also observed in few places deeper stripes **(#3)**. Inside the track fine particles (nm range) are observed, most of them are confined on stripes. A few are spread all around the wear track. No carbides were observed in the middle of the track.

The Figure 4-10**d** presents a wear scar with sheet-like wear particles on the surface. This behavior is related to surface fatigue during repeated plastic deformation by a harder counter-body [56]. Most of the debris observed were apparently compacted and spread over the wear track. Few debris particles (not compacted) were observed inside the track, their size is smaller than 100nm.

The counter piece in alumina was observed using optical microscope and it did not present scratches after the tribocorrosion tests of the three alloys independently of the applied force.
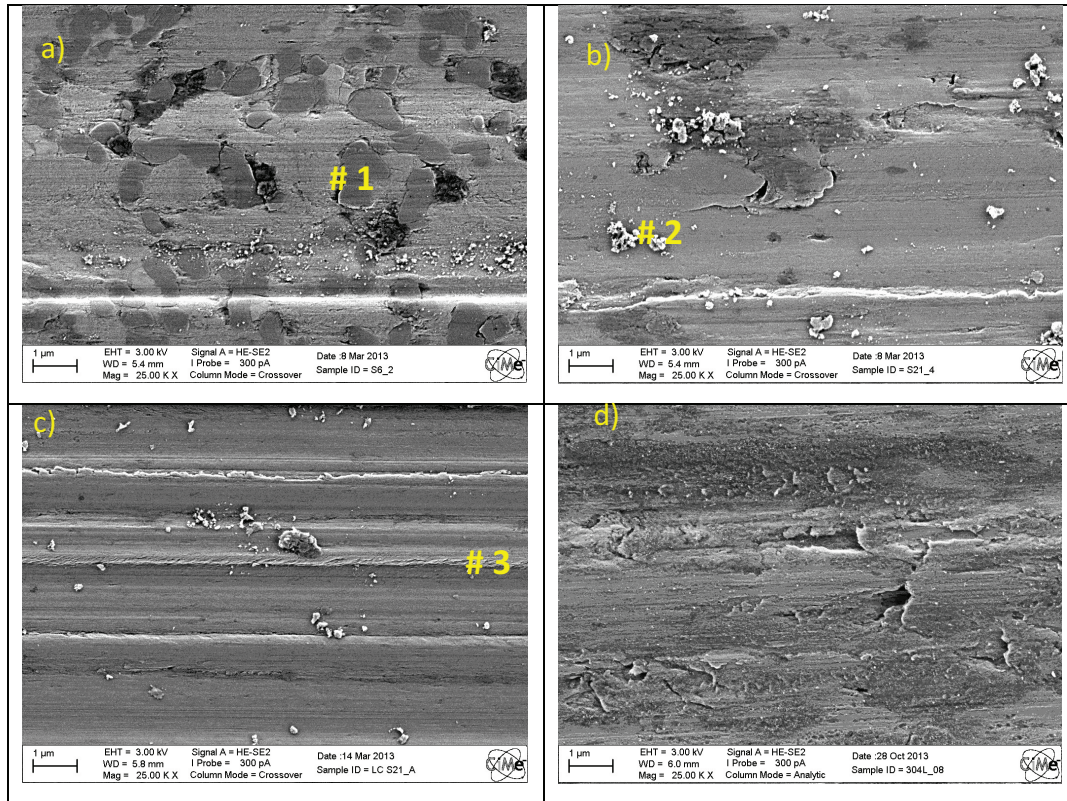
Figure 4-10 SEM images taken inside the wear track at 0V and 11.7 N for a) S6 (CoCrW) alloy, b) S21 (CoCrMo) alloy, c) LCS21 (Low carbon CoCrMo) and d) 304L. #1 carbide de-bonding, #2 debris particles agglomerated and #3 stripes.

4.3.4   Subsurface deformation (FIB)

Figure 4-11 shows SEM images obtained of a cross section prepared through focus ion beam (FIB) of CoCr alloys obtained after a tribocorrosion test at 0V and 11.7N normal force. The images were taken perpendicular to the sliding direction inside (Figure 4-11a, c, e) and outside (Figure 4-11 b, d, f) of the wear track. The latter was taken at ~300μm from the border of the wear track.

- *Outside of the wear track:*

Outside of the wear track (Figure 4-11a, c, e), the alloys presented well-defined grains with a size up to ~3μm on the LCS21 and S21 (Figure 4-11a), and ~2μm on the S6 alloy. Numerous twins were observed on the matrix of the three alloys.

Figure 4-11**c** shows the structure of the Stellite 21 alloy. Grains on the bulk are in size similar to those observed on the LCS21 except near the carbides where grains are smaller. Carbides measuring up to 2μm are observed on the bulk.

Figure 4-11**e** shows the bulk microstructure of the S6 alloy. It is observed a grain refined zone on the top of the surface of less than 0.5μm thick. Then larger grains are observed on the bulk material. They can be distinguished two types of carbides, chromium (dark grey) and tungsten (white) types, they were observed on grains boundaries. Most of the chromium carbides are observed to be agglomerated and only few randomly distributed. Tungsten carbides are found together with chromium carbides. Single chromium carbides measures less than 1μm.

- *Inside the wear track:*

The Figure 4-11**b, d, f** show the subsurface deformation of samples tested under passive potential with an applied normal force of 11.7 N. Notice that the initial microstructure of the alloys (Figure 4-11 **a, c, e**) is lost and a grain-refined zone is observed near the surface. The grain size increases towards the bulk. The formation of the grain-refined zone was observed on previous tribocorrosion works performed in stainless steel [43-45] and CoCrMo [46]. Its origin was attributed to the large strain and strain rate, as well as the multidirectional repetitive loading [57].

Figure 4-11**b** shows the deformation of the LCS21 alloy (no carbides); the grain-refined zone is the largest compared to the other two alloys. Figure 4-11**d** present the grain-refined zone on S21, the grains are observed to be smaller compared to the LCS21. At the lower part of this zone, the bulk

microstructure is still recognized. Carbides were observed floating in between the nano-grains and others on the top of the refined zone. The latter remains at the same level than the surface. Figure 4-11**f** shows that the deformed area on the S6 alloy is smaller compared to the other two alloys and is limited to the first two microns. Chromium and tungsten carbides were observed to keep their shape and structure. In some cases, the grains below the carbides are slightly bigger compared to the ones observed on the refined zone. The bulk microstructure is rapidly observed below the refined zone.
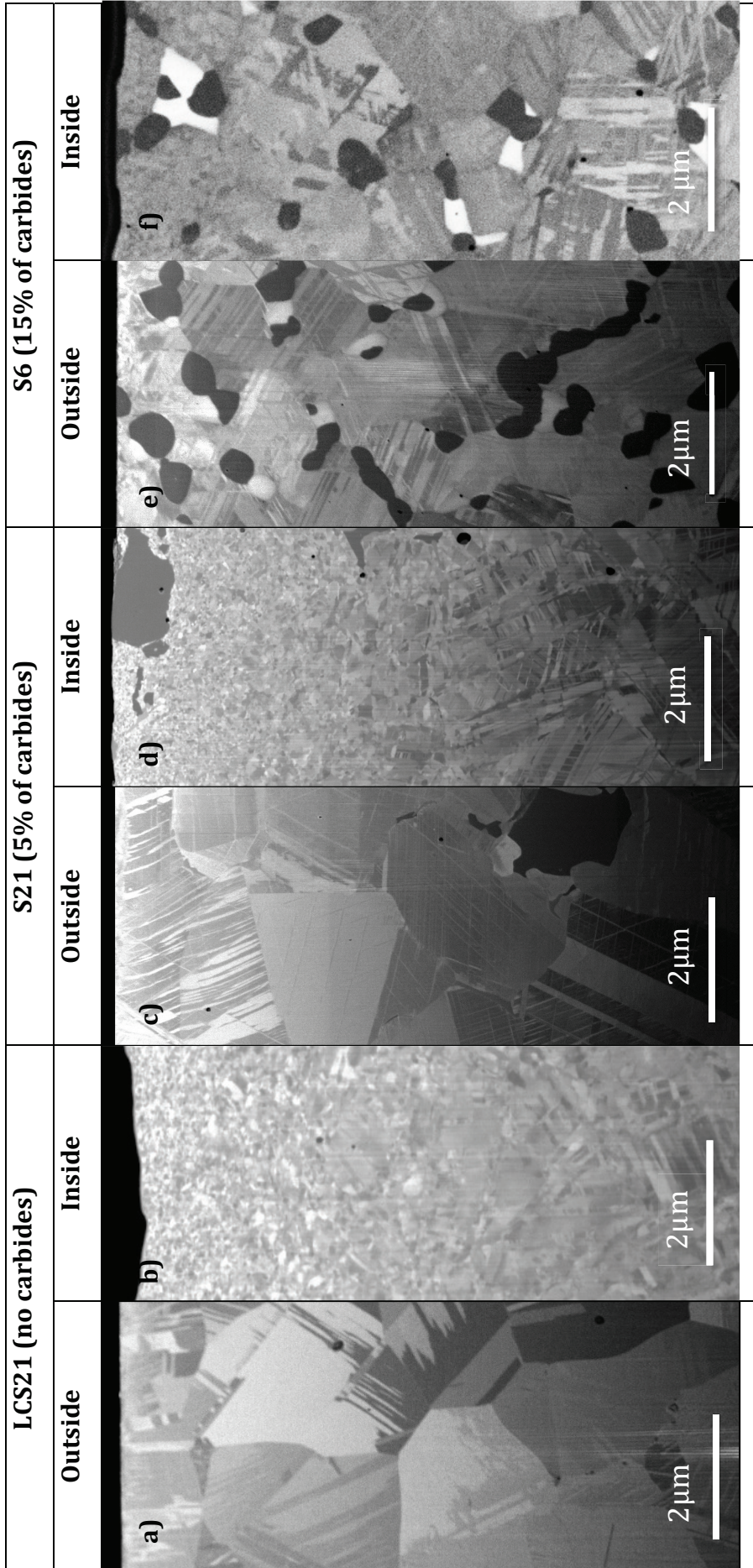
Figure 4-11 FIB transversal cross-sections outside (a, c, e) and inside (b, d, f) of the wear track at passive potential 0V for a,b) LCS21 alloy, c,d) S21 and e,f) S6 at 11.7N. Carbides appear dark grey and tungsten carbides (S6) on white (e,f). Cross sections are taken perpendicular to the rubbing direction.

4.4 Discussion

4.4.1 Effect of normal force

The total wear volume was divided into chemical and mechanical wear from Table 4-6 for the S21 and S6 alloys. These values were plotted in Figure 4-12 as function of the normal force. It appears clearly that the normal force influences both the mechanical and chemical wear.
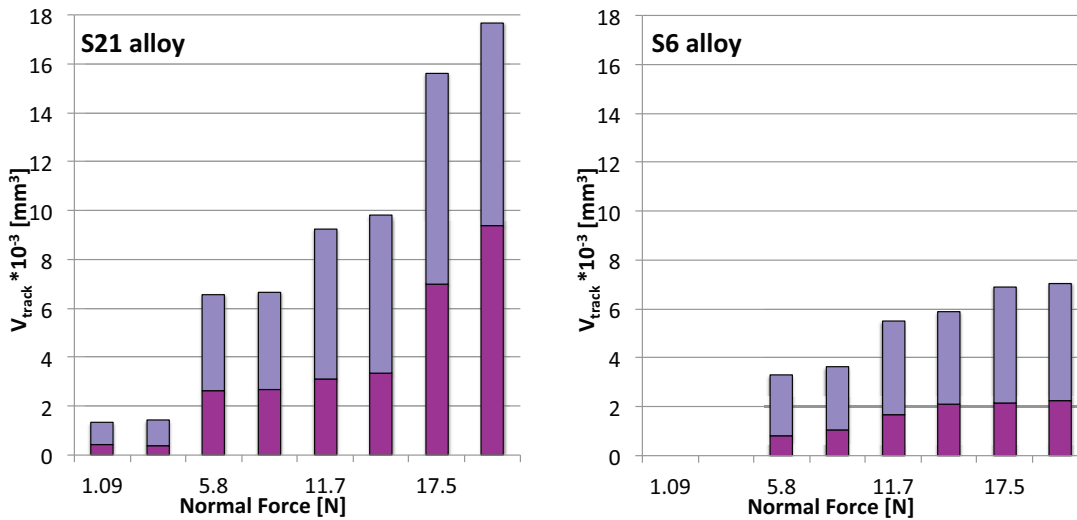
Figure 4-12 Evolution of the wear volume with the normal force for tests on Stellite 21 and Stellite 6 under applied potential (0V/MSE).

It is observed that wear increases with the applied normal force for both alloys. The influence is less important in the case of the Stellite 6 (S6) alloy where the total wear decreases of half when applying the same force (5.8N). The difference is even higher when applying higher normal loads (17.5N). The observed difference when testing different loads between both Stellite alloys could be related to the presence of a higher amount of carbides (~15%) forming a network on S6 (Figure 4-11c). This structure will acts as an internal structure avoiding the matrix to be damaged. In Stellite 21, the amount of carbides is less than 5% in volume and they were dispersed on the matrix (Figure 4-11e).

4.4.2 Effect of potential

The chemical and mechanical wear volumes from Table 4-6 were plotted in Figure 4-13 as a function of the applied potential. It appears that tribocorrosion damage of the investigated CoCrMo alloy is greatly affected by the electrochemical conditions. Indeed, more wear is observed when a passive film forms on the surface independently whether the potential is applied or not (OCP). The prevailing potential influences both the mechanical and the chemical wear. Chemical wear increases with potential from -0.7 V up to 0 V where it tends to stabilize. This increase can be attributed to the harsher oxidative conditions established at larger anodic potentials. Interestingly the mechanical wear shows a clear transition towards higher values (5 time increase) when moving from cathodic potentials to passive potentials. Within the cathodic and the passive domains the potential does not affect significantly the mechanical wear volume.
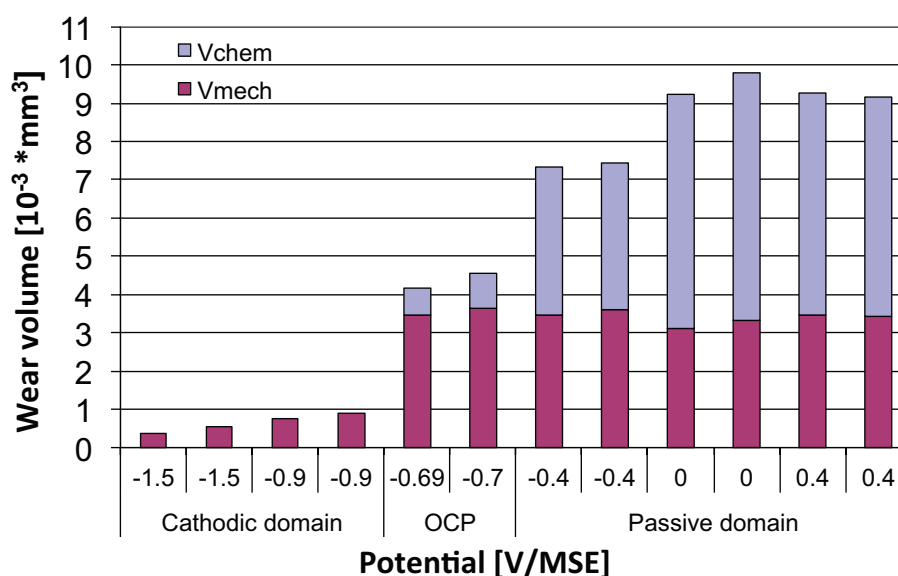
Figure 4-13 Evolution of the wear volume (decomposed in chemical Vchem and mechanical Vmech wear volumes with electrode potential.

The massive difference in mechanical wear between cathodic (free surface) and passive (oxide film) potential was already reported in the case of carbon steel [58, 59], stainless steels [43-45] and Ni-Cr alloys [60]. It was tentatively attributed to the embrittlement of the metal surface (Roscoe effect [61]) caused by the presence of the thin passive film that interferes with dislocation mobility [44]. Indeed, the SEM images show the occurrence of large plastic flow at cathodic potential (Figure 4-10c) while at passive potential cracking and material tearing out are observed (Figure 4-10b).

At cathodic potential a thinner nano-crystalline layer forms in the wear track indicating a less damaged surface compared to the passive potentials. Moreover, friction induced strain hardening is more pronounced at passive potential as indicated by the micro-hardness measurements (Table 4-6). Further, the larger strain hardening evidenced since the coefficient of friction is similar or even slightly larger at cathodic potential, the difference in deformation response is likely caused by the passive film that can act as dislocation source due to its relative hardness compared to the metal as well as a barrier against dislocation annihilation at the surface [44].

4.4.3   Effect of carbides content

The Chemical and mechanical wear volumes values obtained (Table 4-6) for the CoCr alloys and 304L, at 11.7N and OV were plotted in Figure 4-14. It is observed that stainless steel behave similarly than LCS21 alloy with respect to mechanical and chemical wear. Cobalt-based alloys showed that increasing their carbide content makes them more wear resistant when testing them on a sulfuric acid solution.
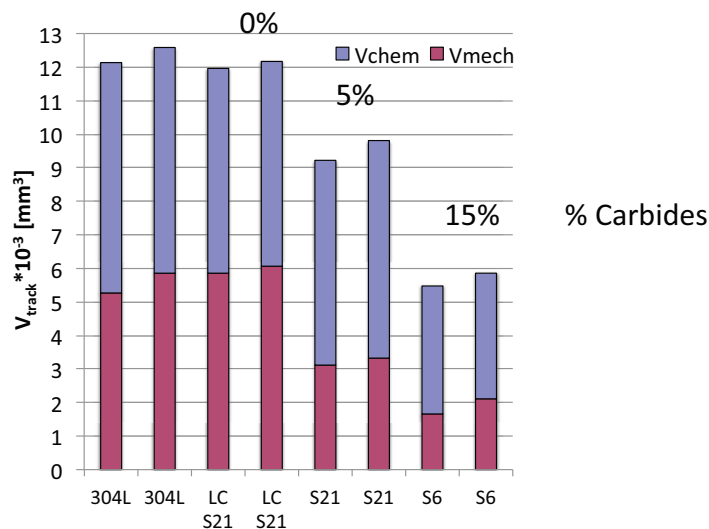
Figure 4-14 Wear volumes for the alloys LCS21, S21, S6 and 304L decomposed into chemical V_{chem} and mechanical V_{mech} wear. The normal force is 11.7N and the applied potential is 0V.

FIB cross sections on the CoCr alloys showed a tribological transformation of their surface (TTS) after a tribocorrosion test as consequence of large strain. The presence of carbides in high amount (15%) seems to limit this deformation as it was observed on the S6 alloy (Figure 4-11**f**). In contrast, the presence of a few carbides (5%) was observed to not influence this subsurface deformation (Figure 4-11**b**). This indicates that the carbides structure on the alloys can take part of the applied

load, as exposed on 4.4.1, and introduce less strain on the matrix even if the applied force is the same.

4.4.4 Mechanical wear

Mechanical wear, in absence of significant chemical effects is expected to follow an Archard wear behavior with the wear volume proportional to the normal load, sliding distance and inversely proportional to the indentation hardness of the metal (Eq. (4-5)).

$$V_{mech} = K \cdot \frac{F_N \cdot l_s}{H}$$

(4-5)

where K is a proportionality constant. In order to check this proportionality the mechanical wear volumes listed in Table 4-6 for passive potentials were plotted in Figure 4-15 against the corresponding ratio normal load F_N to the Vickers indentation hardness (load 0.1 Kg) measured inside the wear track (i.e. accounting for work hardening). In all cases the experimental points fit reasonably well the interpolation line corresponding to the Archard's correlation. The different slopes of the curves indicate that the wear coefficient K varies among the alloys, with the S6 alloy having the lowest sensitivity to wear. Mechanical wear at cathodic potentials is much lower than at passive potential. Unfortunately, the wear rate at cathodic potential was only measured at a single normal load and therefore the applicability of Archard law to the alloys rubbed in absence of passive film cannot be verified.
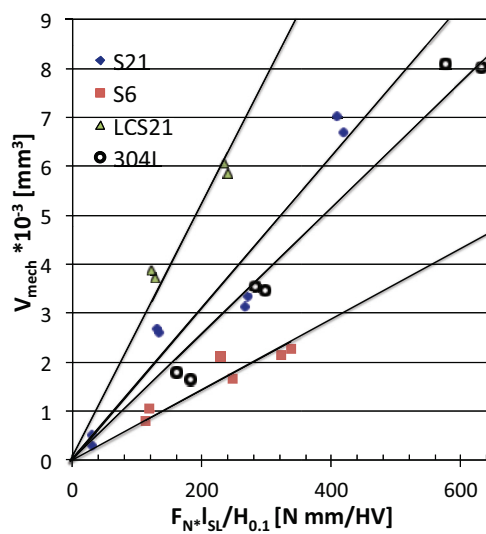
Figure 4-15 Effect of the normal force FN and micro-hardness on mechanical wear volume. All tests carried out at 11.7N and OVMSE are considered for CoCr and 304L.

4.4.5 Chemical wear

Models exist to describe chemical wear as a function of a number of mechanical, electrochemical and materials parameters [Chapter 2]. Considering chemical wear as a consequence of wear accelerated corrosion as plastically deforming asperity contacts, the model proposed by Landolt [24] predicts that the chemical wear volume follows equation (4-6):

$$V_{chem} = \frac{K_a \cdot v_s \cdot Q_p \cdot \left(\frac{F_N}{H}\right)^{0.5} \cdot t_{rub} \cdot M_{mol}}{n \cdot F \cdot \rho} \qquad (4\text{-}6)$$

where K_a is a proportionality constant, v_s is the sliding velocity in m/s, Q_p is repassivation charge density in C/m^2, F_N is the normal force in N and H is the indentation hardness in Pa, t_{rub} [s] is the rubbing time, M_{mol} $[g \cdot mol^{-1}]$ is molecular mass, n is charge number, F is Faraday's constant (approximately 96500 $[C \cdot mol^{-1}]$) and ρ $[g \cdot cm^{-3}]$ the mass density.

In order to verify that this law can describe the experimental results obtained here the chemical wear volumes were plotted against normal force, hardness and passivation charge density. The obtained trends are presented on Figure 4-16.
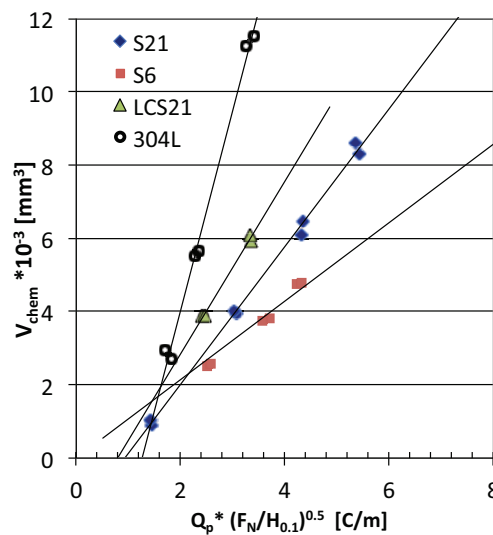
Figure 4-16 Effect of the normal force FN, micro-hardness H and passivation charge density Qp. on chemical wear volume. All tests carried out at 11.7N and OVMSE are considered for CoCr and 304L.

Reasonable good linearity was observed for the tests performed under different loads on all the alloys. Interestingly, the interpolation curves in Figure 4-16 do not cross the origin but cross the abscissa at a value corresponding to a normal force of approximately 0.6 N. This suggests that a minimum force is necessary to trigger chemical wear. This force corresponds to an initial

average Hertz pressure of 420MPa, a value close to the yield strength of the S21 alloy (500 MPa). Plastic deformation of the contact occurs in principle only when the average pressure exceeds the yield strength [62]. This explanation is in apparent contrast to the fact that a similar threshold should be observed for mechanical wear, which also depends on asperity plastic deformation. This is however not clearly observed in Figure 4-15. It is possible that the larger scattering in mechanical wear compared to chemical wear masks a possible threshold. An alternative explanation is that lubrication effects influences wear at low loads and thus creates this apparent threshold.

The increase in current observed during rubbing (Chapter 1) implies that the factor K_a varies with time. K_a depends on the number of asperities and on the probability an asperity contact effectively depassivates the metal. With on going wear the wear track widens and therefore the number of active asperities is expected to increase too. This yields larger currents. Indeed, Dahm [63] observed using a microscope mounted on a tribocorrosion test rig an increase in current with progressive wear track widening.

However, considering average values, the linear relationship found in Figure 4-16 for tests carried out under different loads is in good agreement with Eq. (4-6), which appears as a useful tool to rationalize the effect of different parameters on the electrochemical response of the alloys during tribocorrosion.

Clearly, improving of the modeling requires a better consideration of side effects as lubrication, evolution of roughness and possible evolution of temperature. Local temperature can have and effect although increasing of temperature could not be observed during the test.

4.5 Conclusion

In this study the tribocorrosion behavior of three CoCr alloys and stainless steel 304L has been investigated in a model contact (alumina counter piece, 0.5M sulfuric acid environment, room temperature). Under these conditions, the following conclusions could be drawn.

Two mechanisms contribute to the CoCr alloys deterioration; wear accelerated corrosion (corrosion of depassivated metal) and mechanical wear (ejection of metal particles). Archard's wear law was found to accurately describe the evolution of wear with different normal loads and chemical conditions while the chemical wear is well described by an existing model describing this phenomenon as the repassivation of plastically deformed asperities. Moreover, it was observed that the presence of carbides diminishes the deformed surface below the wear track after a tribocorrosion test.

The results showed that the electrochemical response is mainly determined by the amount of metallic matrix during rubbing. It was observed that a higher amount of carbides diminishes the electrochemical reactivity of the alloy and thus their corrosion. Carbides influence over the mechanical response is much more complex, phenomena such work hardening, friction, third body and wear debris were observed to affect the alloy behavior.

Chapter 5   Physical laws for ϕ_2 or Source flows

Experiments in high temperature pressurized water (Aurore tribometer)

This chapter presents the tribocorrosion behavior of Stellite 6 and 304L alloys under PWR conditions as investigated using Aurore tribometer in high temperature (300°C) and pressurized (150bars) water. Two test protocols are described:

- short term tribo-electrochemical tests intended to provide insights into oxidation kinetics, wear mechanisms and electrochemical response of the investigated metal
- long term wear tests aimed at quantitatively establishing wear rates

The obtained results will serve as basis for the definition of the mass flows ϕ_2 (high temperature water) and ϕ_4.

5.1 Experimental

5.1.1 Materials

The samples were made out of the same Stellite 6 and 304L alloys as used for room temperature tests in the previous chapter. The alloy 316L was subjected to a nitrating processing. This later was obtained in a plasma containing 10% H_2, 20%N_2 and 70% CH_4. The obtained alloy was named 316Lnit [31, 32]. The composition of the alloys is listed in Table 4-1 (Chapter 4).

The sample configuration consists in a tube sliding against a sleeve as sketched on Figure 5-1a. The dimensions are given in the table below for the protocol A (short term tribo-electrochemical tests) and protocol B (long term wear tests).

Protocol	Sample	Internal diameter	External diameter	Height
A	Tube	7.7mm	9.7 mm	5.7 mm
	Sleeve	10.7 mm	15.1 mm	3 mm
B	Tube	8.7 mm	9.7 mm	11 mm
	Sleeve	10.7 mm	15.1 mm	5 mm
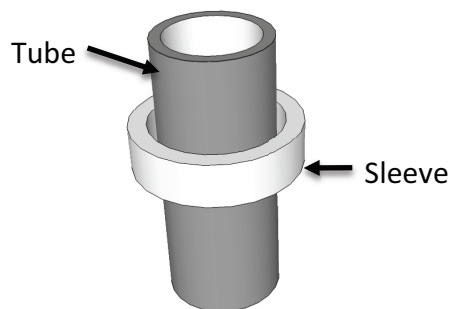
Figure 5-1 Schematic view of the contacting components in the Aurore tribometer.

5.1.2 Aurore tribometer

Aurore tribometer has been developed by AREVA in order to investigate the wear behavior of components under pressurized water reactor (PWR) relevant conditions. One of the applications of AURORE tribometer is to simulate materials degradation in rod control cluster assembly (RCCA) and CRDM under controlled mechanical and electrochemical conditions.

The general features of Aurore are shown in **Figure 5-2**. Two coaxial cylinders form the contact: a stationary sleeve and a mobile tube rigidly clamped on a support mast (**Figure 5-2a** and **Figure 5-2b**). The motion of the tube is controlled by four electro-magnets that permit to obtain different types of motions. Force sensors placed around the sleeve support measure the normal and tangential forces (**Figure 5-2c**). In addition, AURORE tribometer can be equipped by an electrochemical cell and a circulation loop for the water flow [16, 32].

The electrochemical measurements are performed using a three-electrode system. The working electrode is the material to be tested; it corresponds to the tube presented in the **Figure 5-2b**. The counter electrode is made out of platinum. The reference electrode is an external, cold, pressurized Ag/AgCl electrode. A secondary reference electrode (Pt disk) is also used to minimize the Ohmic drop [8]. The tribometer work in an autoclave at a temperature up to 320±5°C and a pressure of 154 bars [64].

b) Electrochemical cell

Minimize Ohmic drop

Platinum disc

Secondary reference

Counter electrode

Platinum

Prevents tube rotation on itself

Flexible support

Tube support

External Reference Electrode

Cold pressurized Ag/AgCl

ZrO$_2$

Stationary sleeve

Tube

Sleeve

Titanium loop

Water flow

Material to be tested

Mobile tube

c) Detection

Tube

Sleeve

Mast

Stiffness

Force sensor

Displacement sensor

Deflection of the support is measured by **the force sensor**

Electro-magnets control de motion of the tube

Normal force F_N
Tangential Force F_f

Kinematics

a)

Mast

Contact zone

Figure 5-2 Configuration of the contact in Aurore Tribometer a) general representation, b) Perpendicular cross section and c) view from the upper part

5.1.3 Tribocorrosion test

Environment

In order to simulate the environment of a PWR, a fully de-aerated solution containing boric acid (H_3BO_3) and lithium hydroxide (lithine LiOH) is commonly used. In PWRs, Boron is used in order to control the neutrons absorbance and lithine is used as pH regulator. The pH of the solutions at 300°C can be adjusted by appropriate dosing of boric acid and lithine. When the solution contains 2000 ppm of boric acid the pH is 5.2. In the case of lithine addition (2.2 ppm) the pH becomes 7.9.

Mechanical solicitations

The Aurore tribometer can provide three different mechanical solicitations: impact, sliding and impact-sliding. The different movements are obtained by appropriately adjusting the current in the electromagnets presented on **Figure 5-2**. During the impact solicitation, the magnets attract the tube towards the sleeve producing the impact (**Figure 5-2c**). The tube is turned before each impact. During the sliding, the magnets keep the tube in contact with the sleeve during all the movement and make them slide all over the sleeve circumference (**Figure 5-3b**). In the case of the impact and sliding movement, the tube suffers first an impact and then it is kept in contact against the sleeve during one cycle. The tube sticks off and then a new impact is performed (**Figure 5-3c**).
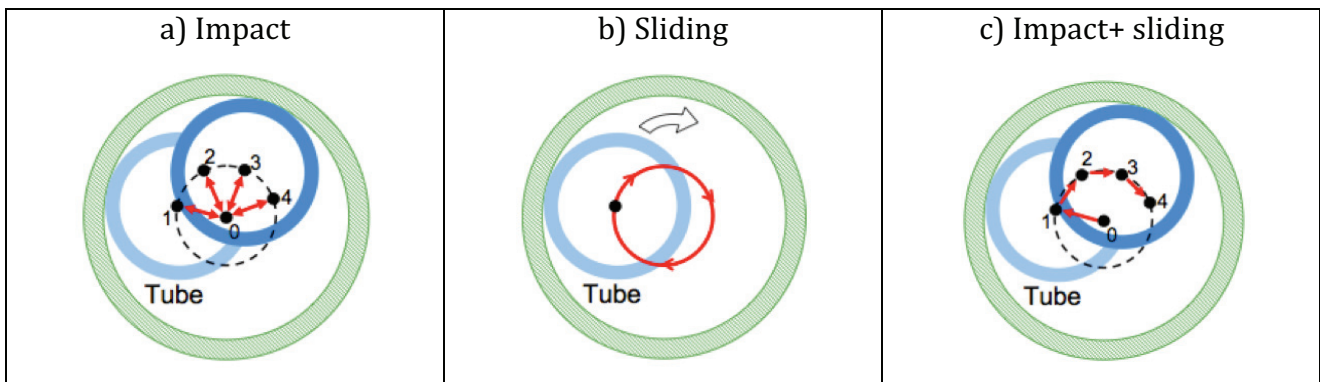
Figure 5-3 Mechanical solicitations between the tube and the sleeve using Aurore tribometer: a) impact, b) sliding and c) impact + sliding [32]

Acquisition protocol A

Tribocorrosion tests realized using Aurore tribometer follow the mechanical and electrochemical protocol [32] schematically shown in Figure 5-4. During the initial phase of thermal stabilization and pressurization, the sample is kept at open circuit potential (OCP), i.e. without any polarization. After reaching a stable temperature of 300°C and a pressure of 150 bar, the sample is subjected to a cathodic cleaning at a potential of -1V/Pt during 600s. Afterwards, the sample is kept at OCP for two hours in order to recover stable OCP. During this time, a sliding cycle is performed to control the alignment of the sample. At t0, i.e. after approximately two hours after thermal stabilization the chosen potential is applied. The first sliding cycle is imposed after one hour of applied potential. Four different sequences of rubbing are performed during the test: three times one cycle, once ten cycles, once hundred cycles and then once thousand cycles. At the end of the rubbing, no polarization (OCP) is applied during cooling and depressurization. 304L, 316Lnit and Stellite 6 alloys were tested using this protocol. Their configuration is exposed on Table 5-1.
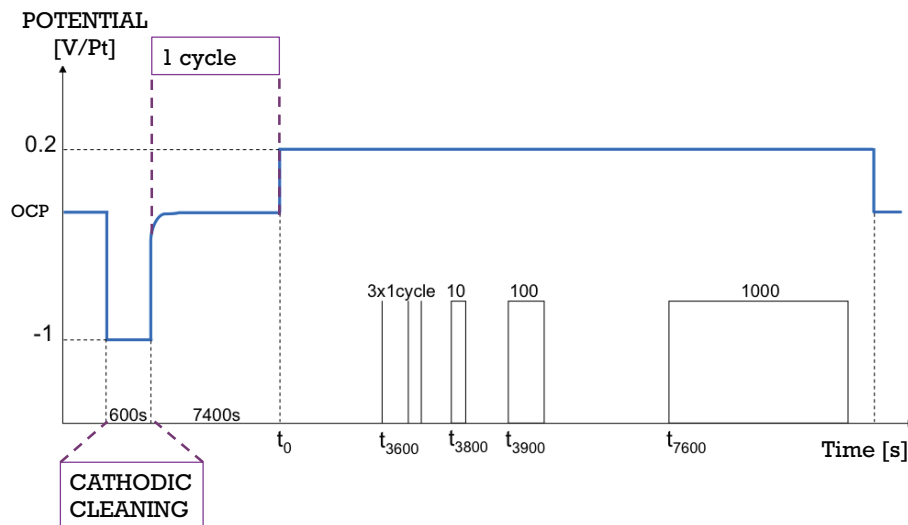
Figure 5-4 Mechanic solicitations and applied potential during Aurore tests [32].

Acquisition protocol B

This protocol was developed by D. Kaczorowski [12] in his thesis to simulate wear in industrial components. Long tests time (70 hours) were chosen in order to match industrial cases and to maximize wear in order to facilitate its quantification. Both sleeve and tube were made out of 304L stainless steel. The tribocorrosion tests were realized in impact/sliding regime. The rotation frequency was 10 rotations per second and 15 impacts per rotation. The corresponding sliding speed was 300 mm/s. The applied normal load was of 15N.The testing time was 70h corresponding to a total number N of impacts of $4*10^7$. The tests were performed at open circuit potential without any potential control. Test were carried out in water at 300°C and 154 bar with either pH 5 or 6.9. Wear was quantified by gravimetry.

Acquisition protocol B

5.2 Results

5.2.1 Protocol A: short term tribo-electrochemical tests

The results shown here are issued from the thesis of Julien Perret [32] except for the test ST4 on the Stellite 6 alloy. A synopsis of the tests is given in Table 5-1.

Table 5-1 Summary of the JP tests by taking into account the configuration tube/sleeve, pH, applied potential, number of cycles, metal hardness (theoretical), the current at the plateau (steady state conditions) and the parabolic oxidation constant k_p for each test. The test ST4 on Stellite 6 was also included (same protocol as JP).

Test	Tube	Sleeve	pH	Potential [V/Pt]	# cycles	Hardness [HV]	$I_{plateau}$ [µA]	k_p [cm²/s]
JP6	**304L**	ZrO$_2$	7.9	0.2	1000	400	8.92	$2.5*10^{-16}$
JP8	**304L**	ZrO$_2$	7.9	0.2	1000	400	9.00	$1.8*10^{-16}$
JP8bis	**304L**	ZrO$_2$	7.9	0.2	1000	400	8.38	$1.8*10^{-16}$
JP7	*316L nit*	ZrO$_2$	7.9	0.2	1000	1600	5.23	$2.9*10^{-16}$
JP11	ZrO$_2$	**304L polish**	5.2	-0.1	1000	400	1.80	$2.1*10^{-16}$
JP12	**304L**	ZrO$_2$	5.2	0.015	1000	400	0.74	$1*10^{-17}$
JP14	ZrO$_2$	**304L polish**	5.2	0.2	1000	400	0.70	$5.08*10^{-17}$
ST4	**Stellite6**	ZrO$_2$	5.2	-0.1	1000	~600	0.08	$3.83*10^{-20}$

Electrochemical response
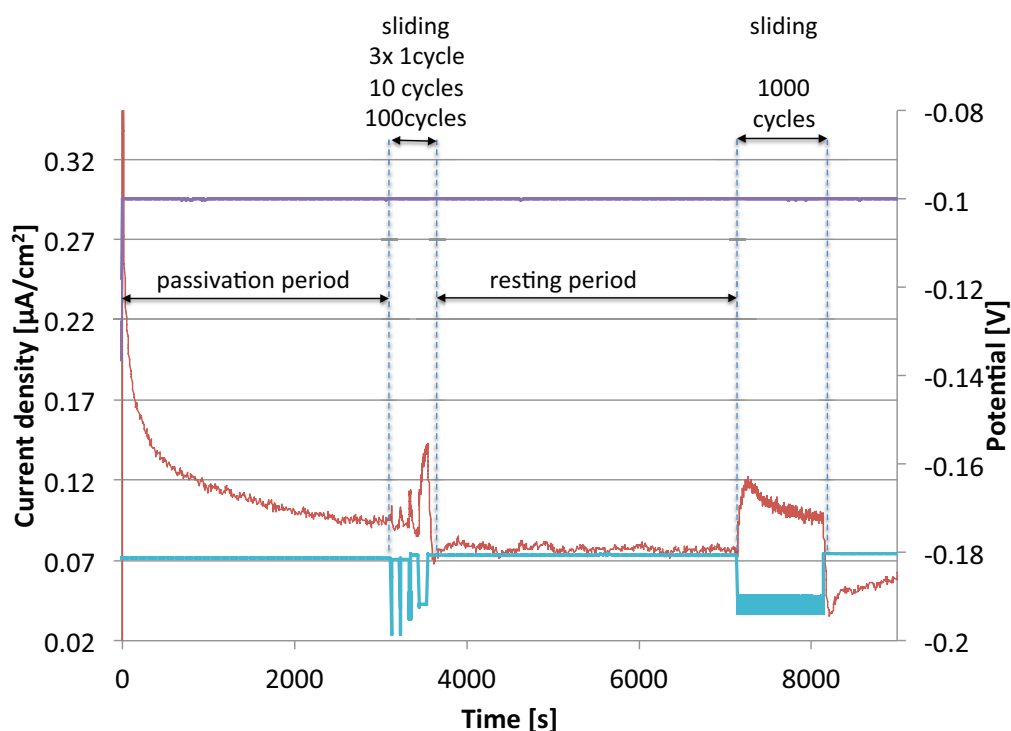
Figure 5-5 Current evolution during tribocorrosion test ST4 using protocol A. Applied potential -0.1V/Pt.

Figure 5-5 shows the evolution of the current during the ST4 experiment. In this figure time 0 corresponds to the application of the passive potential of -0.1 V_{Pt}. The current steadily decreases during the initial hour due to the oxide film build up and thickening (see chapter 2.x.a.b.c.f.g). The first sequence of sliding (3 x 1 cycle, 10 cycles, 100 cycles) starts at 3600 s and in characterized by current peaks related to the local removal of the oxide film and the subsequent re-oxidation of these damaged sites. Note that after this sliding sequence, the current does not immediately recover the level attained before the sliding sequence but rather attains a lower current, at least within the first minutes. This behavior can be attributed to the reduction of hydronium ions to that is catalyzed by the bare metal created by rubbing. The resulting cathodic current tends to lower the measured current. With the repassivation of the rubbed surface, the contribution of the hydronium reduction to the overall current disappears and thus the current recovers the level characteristic of a passive surface. A similar but larger effect is observed after the second sliding sequence (1000 cycles) starting at 7600 s. For the present work this second sliding sequence is more relevant and therefore it will be discussed in more details.

Typical current transients (1000 sliding duration) are shown In Figure 5-6a for the stainless steel 304 and in Figure 5-6b for the ST4 alloy. After an initial running in phase of few hundreds second the current reaches in case of stainless steel (304 or 316Lnit) a steady state plateau. The current recovers the pre-sliding value after few hundreds of seconds after sliding ceases. In case of the ST4 the current plateau is reached after a current peak at after approximately 100 s). The fall in current after the maximum is probably related to the concurrent raise of the reduction of hydronium ions on bare metal. The fact that the anodic recovery of the current after the sliding sequence (Figure 5-6b) has a quite symmetric evolution as the decrease during sliding lend support to this hypothesis. Thus the decrease in current after the peak is disregarded in the following as an artifact not reflecting the real oxidation kinetics.
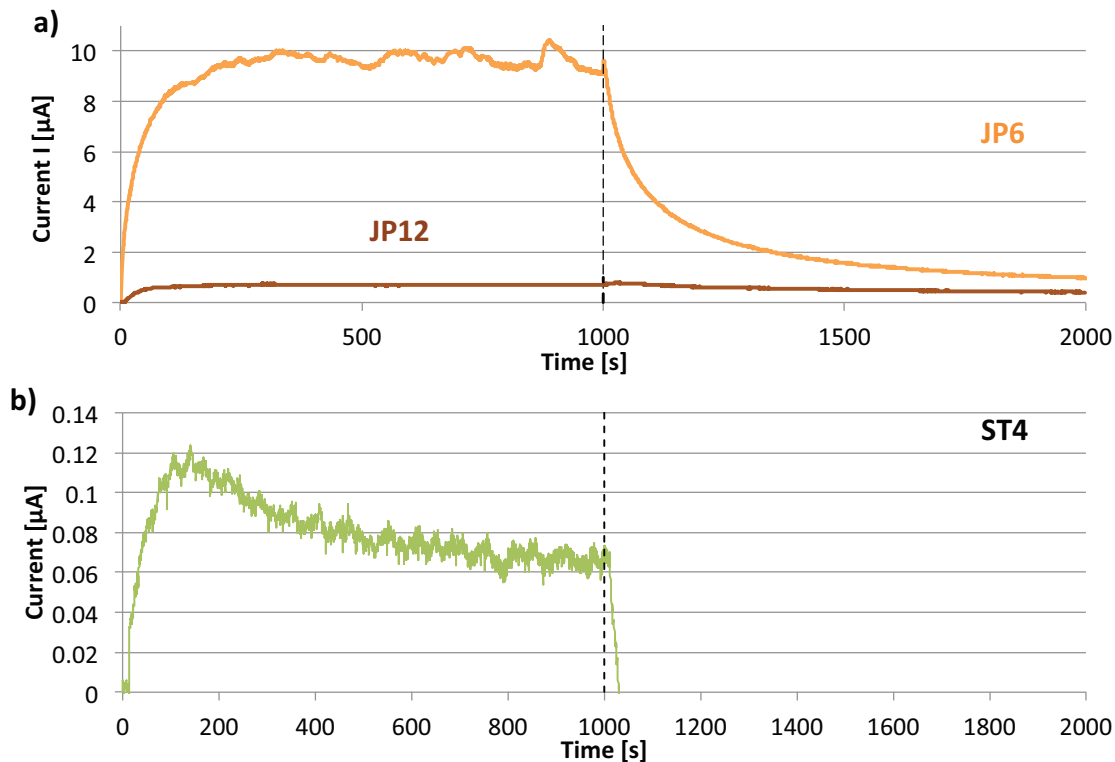
Figure 5-6 Electrochemical response of test performed during 100 and 1000 cycles a) on 304L at pH 7.9 (JP6) and pH 5.2 (JP12), b) Stellite 6 pH 5.2 (ST4).

For the present study the steady state current is of interest. The evolution of the current during the running-in phase and during the repassivation period was already discussed by J. Perret [32] and modeled in terms of balance between mechanical depassivation by abrasion and repassivation. The steady state currents are listed in Table 5-1 for the different tests considered here.

Figure 5-7 shows the surface of the ST4 tube after 1113 cycles. The rubbing direction is horizontal. The original surface present a regular machining ripple pattern with 1.5µm deep hollows. The interval of these ripples is about 50µm as it can be observed on Figure 5-7a. The higher damage is observed on the upper part of the ripples (Figure 5-7b) although in the center of the damaged area, where wear is more pronounced, wear marks are also visible inside the ripples.
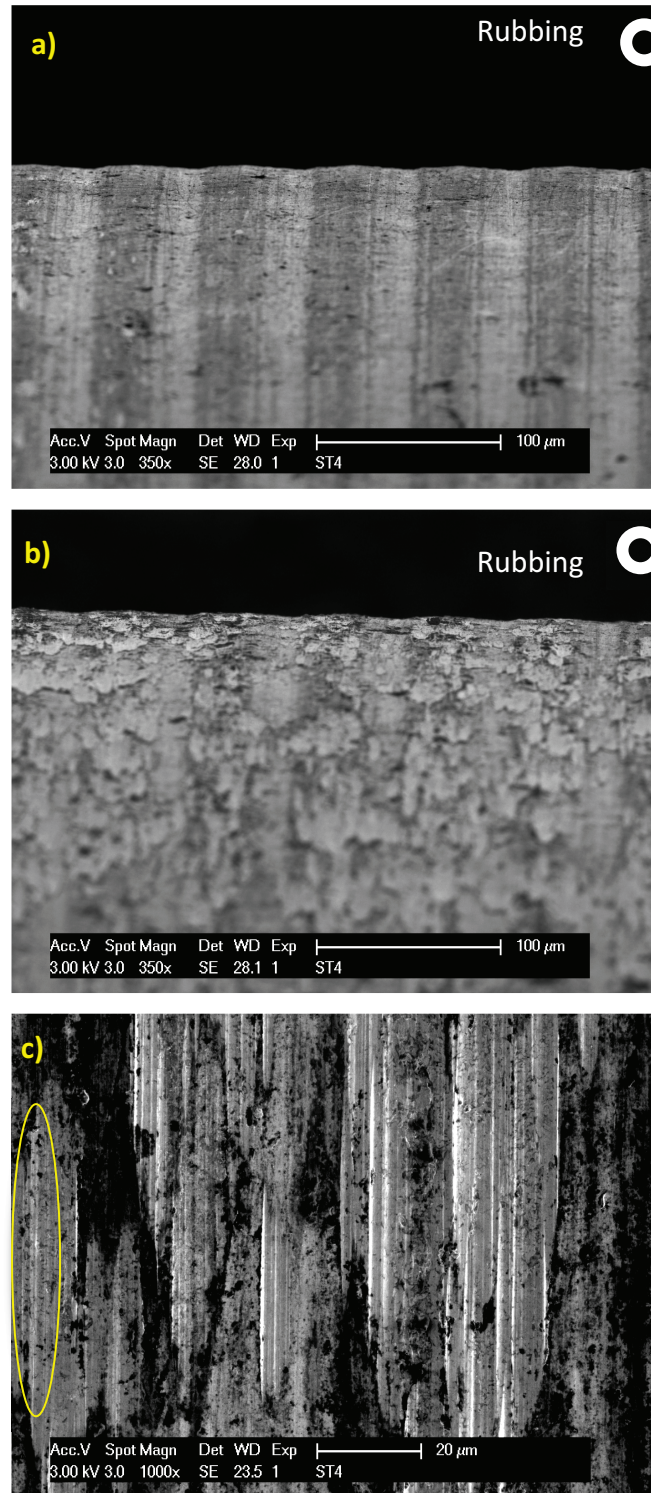
Figure 5-7 SEM images taken a) out of the track, b) inside the track c) inside the track

A more detailed image of the wear marks is presented in Figure 5-7c. The scratches appear in in form of elongated cupules with lengths in between 60 and 70 µm and widths of approximately 10µm. No debris particles were observed inside or outside of the wear track. These patterns are consistent with observed features in nuclear power reactors (Figure 2-2, Chapter 2).

In an attempt to quantify the wear volume of the tube, two surface profiles were measured over a distance of three millimeters perpendicular to the wear track (Figure 5-8) by using a scanning dynamic focus laser profilometer (UBM Telefokus). The damaged sections, where the initial surface patterns are lost, are marked in red in Figure 5-8 while the undamaged areas, characterized by machining ripples, are marked in blue. In order to reduce noise from the ripples and the waviness, the damaged area was interpolated with a function of second degree while the undamaged areas with a polynomial function of third degree. The wear volume is then calculated by taking the difference between the two interpolation functions integrated over the width of the damaged area and multiplying it by the circumference of the tube. The obtained wear volumes are 2.2 and 1.8 10^{-5} mm^3 for the two measured profiles.
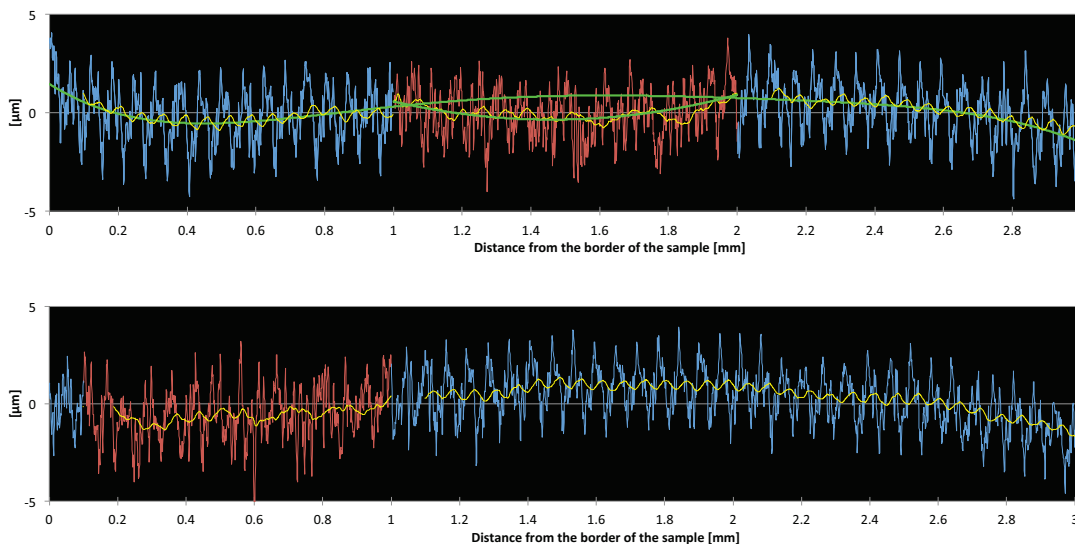
Figure 5-8 Wear track profiles using UBM profilometer in two different places.

In order to determine the thickness and the composition of the oxide present on Stellite 6 after a tribocorrosion test, the sample ST4 was analyzed using Auger Electron Spectroscopy associated with depth profiling by ion bombardment (PHI AES660 system, 10 KV, 10 nA primary electron beam, 2 kV Ar+ ion gun rastered over an area of 1 x 1 mm). Two measurements were realized,

inside and outside of the wear track. The depth profile is presented on the Figure 5-9.
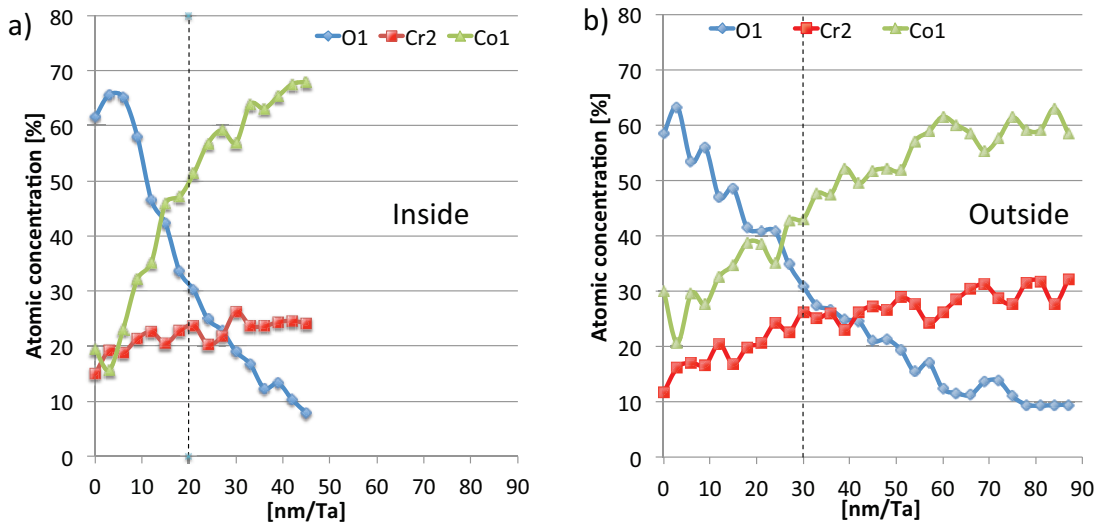
Figure 5-9 Auger depth profile of the sample ST4 (S6 alloy). Tribocorrosion tests were performed on Aurore tribometer. a) Inside the wear track and b) outside of the wear track

It is observed that the oxide thickness outside the wear track is 10nm larger compared to inside. With respect to the chemical composition, it is observed an increase of cobalt outside the wear track while chromium amount is similar. No traces of tungsten were observed. Moreover the interface oxide/substrate outside the wear track is large and give rise to an uncertainty on the obtained thickness. Difference in slope on the oxide Auger profile (inside and outside the wear track) is probably related to the different roughness observed outside the wear track (Figure 5-8).

5.2.2 Protocol B : long term wear tests

The results presented here are extracted form the thesis of D. Kaczorowski [12]. Two tests (KD15 and KD18) were considered. Surface analysis by Auger Electron Spectroscopy was carried out by Julien Perret [32] to characterized the oxide film formed on the samples inside an outside of the worn area. The test conditions and the obtained results, including film thicknesses, are summarized on Table 5-2.

Table 5-2 Summary of the total wear volume obtained during tests performed on Aurore electrochemistry tribocorrosion tests (metal on metal tests, 70h, OCP) [12].

Test	pH	Potential [V/Pt]	F_N [N]	Time [h]	Mass loss		Thickness oxide (nm)	
					Tube	Sleeve	Inside	Outside
KD15/H	6.9	OCP	15	70	-1.72	-0.78	371	99
							372	133
KD18/H$_{PH}$	5	OCP	15	70	-13.3	-4.15	250	200
							182	153
							131	262

5.3 Discussion

5.3.1 Parabolic constant of Stellite 6

The parabolic oxidation constants k_p were obtained using the electrochemical current measured when the potential is applied without rubbing, between t_o and t_{3600} shown in Figure 5-4. The relation used corresponds to the charge density calculated using the parabolic kinetics presented on

$$q = \frac{\rho \cdot n \cdot F}{M_{mol}} \left(2k_p\right)^{1/2} t^{1/2} \qquad (5\text{-}1)$$

Where q is the charge density [C/cm^2], ρ the mass density [g/cm^3], n charge number, M_{mol} is the molar mass [g/mol] and F the Faraday's constant (C/mol). All these parameters are grouped in the constant α.

$$q = \alpha t^{1/2} \qquad (5\text{-}2)$$

α is determined by the slope obtained when plotting the charge density (q) in function of square root of time ($t^{1/2}$). Details of the procedure to calculate the parabolic oxidation constant is described in Perret's thesis [32].

When plotting the experimentally determined charge density against the square root of the time a linear relationship should be observed with a slope α. The parabolic constant kp is then defined as:

$$k_p = \frac{1}{2}\left(\frac{\alpha \cdot M_{mol}}{\rho \cdot n \cdot F}\right)^2 \qquad (5\text{-}3)$$
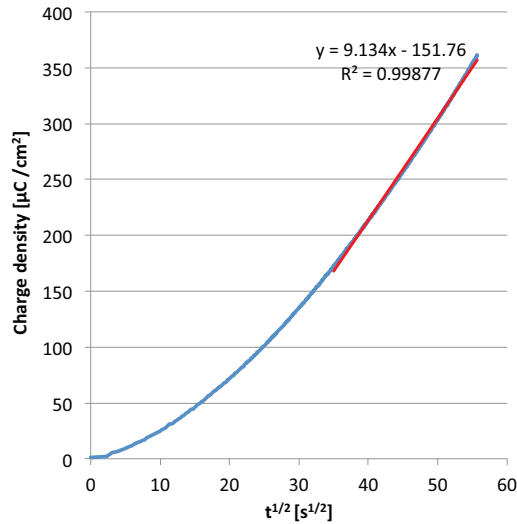
Figure 5-10 Evolution of the charge density measured in the ST4 experiment (Stellite 6) as a function of the square root of time. Potential is -0.1V/Pt.

Figure 5-10 shows the evolution of the passivation charge density as determined by the integration of the current during the initial passivation time (from t_0 to t_{3600} in Figure 5-4). A clear linear trend as predicted by the parabolic oxidation law is observed only after approximately 900 s. The initial deviation from this law indicates that other factors such as the ohmic resistance of the solution and the ions migration through the film under the influence of the electric field [19]. From the slope of the linear part of Figure 5-10 one obtains through equation (5-3) a parabolic oxidation constant k_p for the Stellite 6 of $3.45\cdot10^{-20}$ [cm^2/s]. This value is significantly lower than the one founds for stainless steel (approximately 10^{-16} [cm^2/s] [19]).

5.3.2 Application of wear accelerated corrosion

The wear accelerated corrosion model proposed by Landolt et al. [24] have shown to provide a quite accurate description of the tribocorrosion of stainless steel and stellite at room temperature. In principle, this model should also apply to the wear accelerated corrosion observed in high temperature water. However, some of the model underlying hypotheses needs to be reconsidered. The model assumes that rubbing remove the passive film formed at room temperature on those passive materials with consequent repassivation (oxidation) of the exposed bare metal. Assuming that the bare metal has sufficient time to repassivate between two successive depassivation events, the amount of wear accelerated corrosion corresponds to the amount of metal that needs to be oxidized to form the passive film. The above assumption implies that the oxidation kinetics is much faster than the depassivation events. This condition is satisfied in the low temperature experiments described in the previous chapter where the time necessary for passive film build up is typically in the range of few tens on milliseconds and the time between two successive passes of the ball is 0.5 s. The same is not true for the present Aurore experiments since the oxidation kinetics is much slower than at room conditions. Indeed, as seen in Figure 5-5 the current stabilizes only after more than 1000 s, i.e. a time definitively larger than the time between two revolutions in Aurore tests (1 s and 0.1 s for protocol A and B, respectively). Thus the passivation charge density for Aurore experiments needs to be determined by integrating the parabolic oxidation law from time 0 to the time between two successive depassivation events, i.e. the cycle time t_{cycle} in Aurore experiments. Thus the passivation charge density Q_p in Aurore experiments is defined by Eq. (5-4):

$$Q_p = \frac{\rho \cdot n \cdot F}{M_{mol}} \cdot \left(2 \cdot k_p\right)^{1/2} \cdot t_{cycle}^{1/2} \qquad (5\text{-}4)$$

Combining equation (5-4) with Eq. (4 - 6) Chapter 4 one yield an equation (5-5) describing the current (wear accelerated corrosion) at high temperature is then defined by:

$$I_r = K \cdot v_s \cdot \left(\frac{\rho \cdot n \cdot F}{M_{mol}} \cdot \left(2 \cdot k_p\right)^{\frac{1}{2}}\right) \cdot t_{cycle}^{1/2} \cdot \left(\frac{F_N}{H}\right)^{0.5} \qquad (5\text{-}5)$$

In order to verify the appropriateness of Eq. (5-5) to describe the wear accelerated corrosion in Aurore tribo-electrochemical experiments (protocol A), the plateau current values (Table 5-1) were plotted in Figure 5-11 against the ratio of the k_p and hardness to the power 0.5. As all other parameters were the same in these experiments and only the hardness (304L or 316L nit steels) or the k_p (different potentials) varied, a linear relationship is expected in Figure 5-11.
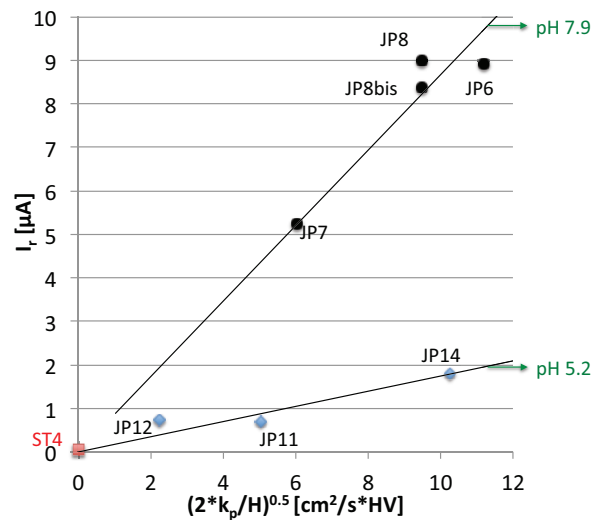
Figure 5-11 Current function of the k_p and the hardness under different tests conditions: JP6, JP8 and JP8bis (304L, pH 7.9, 0.2V/Pt), JP7 (316 nitrided, pH 7.9, 0.2V/Pt), (304L, pHJP11 (304L, pH 5.2, -0.1V/Pt, inversed configuration), JP12 (304L, pH 5.2, 0.015V/Pt) and JP14 (304L polished, pH 5.2, 0.2V/Pt).

Linear relations are indeed observed between current and the ratios k_p to hardness. This indicates first that equation (5-5) effectively describes wear accelerated in PWR conditions. Secondly, the slopes, i.e. the depassivation probabilities K, depend on the pH of the aqueous environments. This is probably related to the different nature of the oxide film formed at different pH values [32] and thus to the different generated surface mechanical properties (hardness, toughness, internal stresses).

5.4 Conclusion

Tribocorrosion test under PWR conditions using Aurore tribometer has shown that:

- Parabolic oxidation growth kinetics describes well the oxidation of S6 Stellite as measured by electrochemical techniques in Aurore tribometer.
- The wear accelerated corrosion model developed for low temperature tribocorrosion can be applied successfully to describe high temperature degradation. For this the passivation charge density must be defined as a function of the parabolic oxidation constant k_p and the time between two depassivation events
- The proportionality constant of the wear accelerated corrosion model is significantly affected by the water pH that, by modifying the oxide composition, likely influences its mechanical properties.

Chapter 6   Definition of Mass Flows ϕ

This chapter is dedicated to the formalization of mass rates associated to the flows considered here for modeling the overall wear rate:

ϕ_1 Metal particles entering the friction film
ϕ_2 Oxidized metal entering friction film
ϕ_3 Particle detachment from the friction film
ϕ_4 Particles re-deposition
ϕ_5 Oxidation of metal particles within the friction film

The formalization of the two first flows will be based on the mechanisms and models assessed in the previous two chapters. Published theoretical and experimental observations will be used to formulate flow rates. In absence of available experimental data or theories, the last two flows are appraised by mathematically formalizing simplified, speculative phenomenological models.

6.1 Mass flow

The variation of the mass dm as a function of time t is represented by the symbol ϕ_n and it defined as follows:

$$\phi_n = \frac{dm}{dt} = \rho_{metal} \cdot \frac{dV}{dt} \quad [g/s]$$

(6-1)

Where, V is the wear volume [cm^3], ρ the mass density [g/cm^3].

6.1.1 Mass flow $\boldsymbol{\phi}$1

The mass flow $\boldsymbol{\phi_1}$ corresponds to the amount of material that is lost from the substrate (Compartment 1) and introduced as metal into the friction film by plastic deformation of asperities and subsequent wear and mechanical mixing. This flow can be assimilated to the mechanical wear as assessed in the investigation of room temperature tribocorrosion of Stellite alloys and 304L steel described in Chapter 4. Mechanical wear was found to be correctly described by the Archard's wear law (Equation (4 - 5)) relating volume loss to normal load F$_N$, indentation hardness H$_{in}$ and sliding distance l$_s$.

Thus, by considering a constant sliding velocity v$_s$ and in absence of a friction film, the mass flow $\boldsymbol{\phi_{1,RT}}$ is given by Eq. (6-2).

$$\phi_{1,RT} = K_{\phi_{1,RT}} \cdot \rho_{metal} \cdot F_N \cdot v_s \cdot \frac{1}{H_{in}}$$

(6-2)

Here the subscript RT designates room temperature conditions. The proportionality constants $K_{\phi_{1,RT}}$ is determined by plotting the mechanical wear rate (Table 4-6) as a function of the parameters exposed in Eq. (6-2). Data concerning S6 and 304L alloy were retained to quantify the proportionalities constants, as these two materials are of more interest for PWR applications. The obtained plots are presented in Figure 6-1.
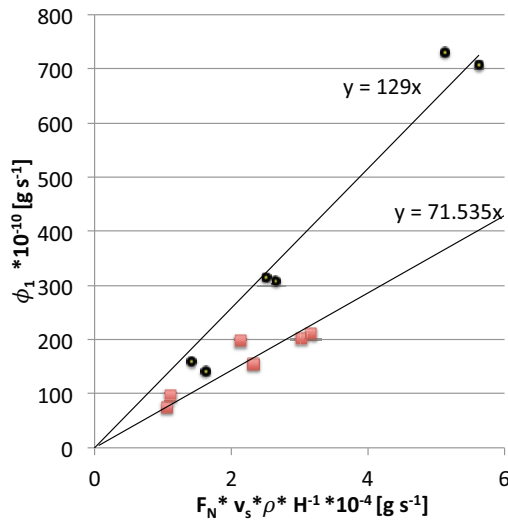
Figure 6-1 Mass flow ϕ_1 for Stellite 6 and 304L stainless steel defined by taking Eq. (6-2). The slope of the linear regression that was forced to pass through zero determines the proportionality factor $K_{\phi_{1,RT}}$.

The slopes of the regression lines yield $K_{\phi_{1,RT}}$ values of $12.9 *10^{-5}$ and $7.15*10^{-5}$ for 304L and Stellite 6 alloys, respectively.

However, before applying equation (6-2) to the PWR conditions one has to consider that the oxide film thickness and the metal hardness may change when passing from a temperature of 25°C to 300°C.

Oxides films formed at room temperature on the considered alloys have typical thicknesses of a few nanometers, i.e. much thinner that the oxides formed under PWR conditions. The latter may thus attenuate the stress field acting on the metal and thus decrease its deformation and wear. Therefore, for applying the mass loss rate corresponding to ϕ_1 one has to integrate stress attenuation factor a in Eq. (6-2) as expressed in Eq. (6-3).

$$\phi_{1,RT} = K_{\phi_{1,RT}} \cdot \rho_{metal} \cdot a \cdot F_N \cdot v_s \cdot \frac{1}{H_{in}}$$
(6-3)

The extent of attenuation depends on the acting normal and tangential forces as well on the thickness and mechanical properties of the oxide film. Kermouche et al. [21] studied, using finite element modelling, the cumulated strain in an austenitic stainless steel surface after sliding impact of a rigid asperity (radius: 105µm) and more in particular the effect of a surface film of 1 µm thickness. The numerical simulation showed that for a friction film of 1µm thick, the plastic strain

just below the substrate surface can be reduced by a factor of 2 under impact-sliding (Figure 6-2). Further, the presence of the film greatly reduces the accumulated strain in the near surface zone. This analysis was performed assuming the asperity to be rigid and spherical. Loading is achieved by monitoring the displacement of the asperity of radius 105µm; the maximum penetration depth during sliding is 1µm and an oxide thickness of 1µm [20].
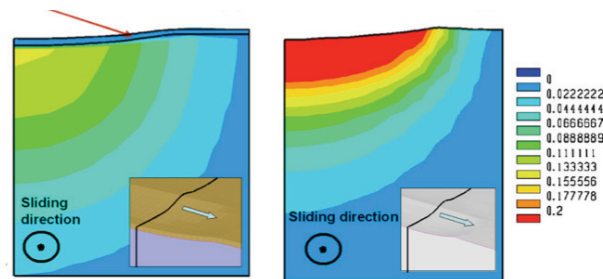
Figure 6-2 a) Distribution and intensity of the cumulated plastic strain after impact-sliding on a 304L stainless steel in presence (left diagram) and in absence (right diagram) of a 1 µm thick oxide film [21].

The above information is not sufficient in order to precisely determine values of the attenuation factor a. By taking the maximum cumulated strain one can estimate an attenuation factor of 0.5 for a 1 µm thick film. In the Aurore tests considered in the present work the film thickness is approximately 200-300 nm and thus the attenuation should be less, around 0.9 by taking a simple cross multiplication. However, by considering the amount of deformed material, which is much larger in absence of the film as shown in Figure 6-2, the attenuation could be significantly smaller than 0.5. Thus, the attenuation factor a is considered in the followings as a known unknown parameter that requires fitting for quantitative assessments.

The mechanical property of 304 stainless steel varies depending on temperature. When passing from 20°C to 300°c the elastic limit and young's modulus changes from 175 to 100 MPa and from 200 to 179 GPa, respectively, Thus the hardness and the work hardening are also expected to change. Therefore, the hardness values considered in Eq. (6-3) should be measured directly on surface worn under PWR conditions. Kaczorowski observed experimentally that after rubbing under PWR conditions in the Aurore tribometer, the hardness of the 304L steel lying below the friction film was approximately 600 HV suggesting larger work hardening than found at room temperature (hardness after rubbing ranging from 300 to 370 HV) in the laboratory experiments described in Chapter 4.

The hardness of Stellite alloys also decrease with increasing temperature at a rate of approximately 0.1 HV per °C [65], i.e. a difference of less than 30 HV when moving from room temperature to PWR conditions. Although the effect of temperature on the Stellite mechanical properties alloys appears small, experimental determined hardness values should be used in the model.

6.1.2 Mass flow $\phi2$

The mass flow ϕ_2 corresponds to the amount of oxidized substrate material that feeds the friction film from compartment 1. In the tests at room temperature this behavior is related to the wear accelerated corrosion that results chemical wear. In Chapter 5 Eq. $(5-5)$ was derived from the wear accelerated model proposed by Landolt et al. [24] by expressing the oxidation charge density in terms of parabolic oxidation kinetics. Eq. $(5-5)$ expresses the current due to wear-accelerated corrosion at high temperature as a function of the parabolic oxidation constants and the time t_{cycle} between two successive strokes. Eq. (6-4) can then define the mass flow ϕ_2:

$$\phi_2 = I_r \frac{M_{mol}}{n \cdot F} = K_{\phi_2} \cdot v_s \cdot \left(\rho \cdot \left(2 \cdot k_p \right)^{\frac{1}{2}} \right) \cdot t_{cycle}^{1/2} \cdot \left(\frac{F_N}{H} \right)^{0.5} \qquad (6\text{-}4)$$

Data concerning S6 and 304L alloy were retained from experimental room temperature tribocorrosion tests to quantify the proportionality constants. The obtained plots are presented on Figure 6-3.
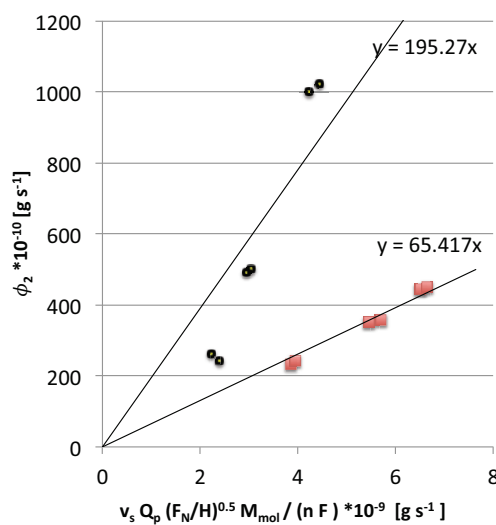
Figure 6-3 Mass flow ϕ_2 for Stellite 6 and 304L stainless steel defined by taking Eq. (6-4). The slope of the linear regression that was forced to pass through zero determines the proportionality factor $K_{\phi_{2,RT}}$.

The linear regression performed on each material data was forced to pass through zero in order to obtain the slope. This latter corresponds to the value of the proportionality constant $K_{\phi_{2,RT}}$ under room temperature conditions. The obtained values are 19.5 and 6.54 for 304L and S6 alloys respectively.

These values were used to calculate the anodic current due to the flow ϕ_2. The obtained values are listed in the Table 4 - 6 for different experimental conditions. Interestingly, the calculated currents are significantly larger than the experimentally observed ones. The ratio between model predictions and measured values is quite reproducible for identical conditions and attains 0.12 for the 304L steel at pH7.9, 0.04 for the 304L steel at pH5.2 and 0.4 for the Stellite 6 alloy at pH 5.2. This indicates that at high temperature the depassivation process is less effective than at room temperature, most likely because the thicker oxide film formed at 300°C screens the loads and reduces the overall plastic strain experienced by the underlying metal in an analogous manner as already discussed for the mechanical wear associated with flow ϕ_1. Thus, the attenuation factor a should also be introduced in Eq. (6-4). This yields Eq. (6-5) that describes the mass flow ϕ_2 under PWR conditions.

$$\phi_2 = K_{\phi_2} \cdot a \cdot v_s \cdot \left(\rho \cdot (2 \cdot k_p)^{\frac{1}{2}} \right) \cdot t_{cycle}^{1/2} \cdot \left(\frac{F_N}{H} \right)^{0.5} \qquad (6\text{-}5)$$

From the ratios listed in Table 6-1, the attenuation factors are 0.12 for the 304L steel at pH7.9, 0.04 for the 304L steel at pH5.2 and 0.4 for the Stellite 6 alloy at pH 5.2.

Table 6-1 Summary of the current values calculated using the Eq. (6-4) and compared with the experimental steady state current presented on chapter 5.

pH	5.2	7.9			5.2			7.9
Material	S6	304L			304L			316L
Test	ST4	JP6	jP8	jP8bis	JP12	JP14	JP11	JP7
Current [µA] Predicted [1]	0.20	81.15	68.86	68.86	16.23	16.23	74.37	43.70
Current [µA] Measured in Aurore (300°C)	0.08	8.92	9.00	8.38	0.74	0.70	1.80	5.23
Measured to calculated ratio	0.40	0.11	0.13	0.12	0.05	0.04	0.02	0.12

[1] based on equation (6-4) considering $K_{\phi_{2,RT}}$ values determined for room temperature conditions.

6.1.3 Mass flow $\phi 3$

The mass flow ϕ_3 corresponds to the oxide wear rate. It represents the oxide particles moving from the compartment 2 to compartment 4 (external environment). In order to convert the mass of oxide into equivalent mass of metal, the stoichiometric ratio r_{ox} is defined as follows:

$$r_{ox} = \frac{m_{alloy}}{m_{oxide\ formed}} = \frac{M_{alloy} \cdot n_{X,oxide}}{n_{X,alloy} \cdot M_{oxide}}$$

(6-6)

Thus:

$$m_{oxide\ formed} = \frac{m_{alloy}}{r_{ox}}$$

(6-7)

Where, m_{alloy} represents the mass of bare metal [g], m_{oxide} formed is the amount of oxide formed using a given amount of metal [g], M_{alloy} is the molar mass of the alloy [g/mol], X is the element present in the oxide and the alloy, $n_{X,oxide}$ is the number of moles of the element X on the oxide [mol], $n_{X,alloy}$ is the number of moles of the element X present on the alloy composition [mol] and M_{oxide} is the molar mass of the oxide [g/mol]

r_{ox} values are calculated based on the hypothesis that the oxide formed is mainly CoO in the case of Stellite 6 and Fe_2O_3 for the 304L. The values of r_{ox} are 1.55 and 1.04 for CoO and Fe_2O_3 oxides respectively.

In this work it is postulated that the wear of the oxide films follows an Archard's law type. Thus one can write:

$$\phi_3 = K_{\phi_3} \cdot \rho_{oxide} \cdot F_N \cdot v_s \cdot r_{ox}$$

The proportionality constant K_{ϕ_3} corresponds to the specific wear rate, i.e. the removed volume per unit load and per unit sliding length commonly used in the engineering practice of tribology. Such data are more commonly found in literature and easier determined experimentally than the non dimensional wear coefficients corresponding to the ratio between specific wear rate and indentation hardness used for ϕ_1 .

The specific wear rates depend among others on materials properties such as composition, microstructure and level of internal stresses. They should be therefore determined

experimentally. In the present case this would require producing oxide films on the investigated metal surface through oxidation in high temperature pressurized water in order to reproduce the specific structures and composition found in PWR conditions. The tested oxide film could then be tested in tribometers as used for the investigations of the source flows at room temperature. Such an approach presents several difficulties. First, the oxidation process in water is slow and requires long immersion times of several weeks or even months. Secondly, metal oxidation is highly dependent on surface defects and thus optimized protocols need to be established for carrying out controlled oxidation experiments. Further, the ex-situ tribological characterization is needed isolate the oxide wear process and to suppress concomitant oxide reformation. It is however questionable whether the oxide film properties established during isothermal oxidation in water would change or not during cooling down, in particular with reference to internal and thermal stresses. Due to the uncertainties associated with the experimental determination of specific wear rates of oxide films and the time constraints of the thesis it was decided to extract approximated wear rates from existing literature.

For this, a literature search of wear of ceramics in water was carried out. The obtained data are summarized in Table 6-2.

Table 6-2 Literature data concerning the values of the constant K_{ϕ_3}

Reference	Couple	Environment	Load	Speed	K_{ϕ_3}
Litaoka Wear 1997	SiC / SiC	Water 300°c	19.6 N	0.42 m/s	$4 \ 10^{-8}$ cm^2/N
Hsu in modern tribology Handbook	Al$_2$O$_3$ / Al$_2$O$_3$	Water, room temperature	10 N	0.3 m/s	$4 \ 10^{-12}$ cm^2/N
idem	Y TZP/ Y-TZP	Water, room temperature	10 N	0.3 m/s	$2 \ 10^{-12}$ cm^2/N
idem	SiC / SiC	Water, room temperature	10 N	0.3 m/s	$1 \ 10^{-12}$ cm^2/N
Wei 199X	Cr$_2$O$_3$ / steel	Water, room temperature			$1 \ 10^{-12}$ cm^2/N

The specific wear rates found for different types of ceramics in cold water range from 2 to $8 \ 10^{-12}$ cm^2/N, a surprisingly small range. Increasing the temperature of water apparently leads to larger

wear rates as suggested by comparison of the data on SiC from Kitaoka [39] and Hsu [66]. In the following a specific wear rate of 2 10^{-12} cm^2/N was considered as reference value for $K_{\phi 3}$.

As indicated by the variability of the attenuation factors determined in the precedent paragraph, the mechanical properties, and thus the wear rate, of the oxide film are expected to change when modifying the water pH or the alloy. A speculative but simple approximation can be considered for taking into account the differences in wear rates of the different oxide films. For this the oxide formed on 304 stainless steel at pH 5.2 was considered as a reference having a $K_{\phi 3}$ of 2 10^{-12} cm^2/N as extracted from the literature.

6.1.4 Mass flow $\phi 4$

The mass rate ϕ_4 corresponds to the amount of metal that was first detached from the friction film and afterwards re-deposed on the friction film by sedimentation and/or compaction. The re-deposition is a complex phenomenon involving among others inter-particle forces linked to the double layer charge and particle size [32], convection conditions in the fluid, contact geometrical considerations. This flow cannot be appraised in its complexity within the time frame of this thesis. Thus it will be phenomenological described by a kinetic of first order involving the flow being proportional to the metal mass concentration $|M^o|_4$ in the compartment 4 (solution) as described below:

$$\phi_4 = k_{\phi_4} \cdot |M^\circ|_4 \qquad\qquad (\,6\text{-}8\,)$$

The proportionality constant k_{ϕ_4} can be estimated from the experimental findings described in Chapter 5 in the following way. The re-deposition of particles in the contact was observed to depend on the water pH. Indeed, the Aurore test KD15 (Table 5-2) performed at pH 6.9 presented thicker (approximately 250 nm according to Auger depth profiles) oxide layers inside the wear track compared to the outside, non rubbed part. This thickening is entirely attributed to the re-deposition of oxide particles. This permits to calculate the fraction of re-deposed metal (FRDM). In fact the 250nm are equivalent to 0.042mg of metal by assuming Fe_2O_3 to be the main oxide formed on the surface (density 5.2g/cm^3). The volume is calculated considering the sample geometry and that the thickness of the oxide is uniform in the 1mm long wear track. The experimental FRDM is then the ratio of the amount of re-deposed material (0.042mg) and the total material loss (2.5mg, tube and sleeve). This relation permit to calculate that only approximately 2% of material released into the water re-deposes on the metal surface during rubbing.

By regarding this information, the constant k_4 can be calculated. Based on the mass rates flow chart (Chapter 3). It is observed that the FRDM fraction can be defined as the ratio between the mass rate coming from the Compartment 4 ($\phi_4(t)$) and the mass rate going out of the friction film ($\phi_3(t)$). This relation is presented on Eq. (6-9) :

$$FRDM = \frac{\phi_4(t)}{\phi_3(t)} \qquad\qquad (\,6\text{-}9\,)$$

By replacing $\phi_4(t)$ with the expression presented on Eq. (6-9), we obtain:

$$FRDM = \frac{k_{\phi_4} \cdot |M^o|_4}{\phi_3(t)}$$

<div align="right">(6-10)</div>

Where $|M^o|_4$ is determined by performing the mass balance on the compartment 4 ($\frac{dM_4}{dt}$). The procedure to obtain this expression is presented on Appendix section. It was observed that $|M^o|_4$ is equal to $\frac{(1-e^{-k_4 t}) \cdot \phi_3}{k_4}$. By replacing this expression on Eq. (6-10), we obtain that:

$$FRDM = 1 - e^{-tk_4}$$

<div align="right">(6-11)</div>

The experimental FRDM (2%, KD15) is then replaced on Eq. (6-11) with a time t equal to 252'000 seconds (70h tests). According to this procedure $\boldsymbol{k_{\phi_4}}$ **is equal to 6.8*10^{-8} s^{-1}**. This value will be used in the mass balance calculations described in the next chapter.

6.1.5 Mass flow $\boldsymbol{\phi}$5

The transport between the compartments is written in terms of a first order irreversible reaction rate. Its general form [67] is presented on Eq. (6-12).

$$A \xrightarrow{k} B, \quad r = k \cdot C_A \qquad \text{(6-12)}$$

Where A is the reactant, B the product, k the reaction rate constant, r the reaction rate and C_A the concentration of A. When describing the mass rate ϕ_4 and ϕ_5, the reactant A corresponds to the amount of mass present on the compartment 4 (C4) and on the compartment 3 (C3) respectively.

They mass ϕ_5 then will be written as is present on Eq. (6-13)

$$\phi_5 = k_{\phi_5} \cdot |M^o|_3 \qquad \text{(6-13)}$$

The constant $k_{\phi 5}$ is related to the amount of material that will pass from the compartment 3 (C3) to 2 (C2). The cross sections performed on samples after tribocorrosion tests on Aurore tribometer (PWR conditions) [31] do not show the presence of metal particles on the friction film. In contrast, it can be observed the subsurface deformation and a mixing behavior. Based on these observations, I could assume that all the metal particles will be transformed into oxide by being in contact with the interface substrate/friction film and/or friction film/solution. Under this condition the constant k_{ϕ_5} is 1.

6.2 Summary

6.2.1 Parameters values and proportionalities constants

Table 1: Parameters values of tests KD15 and KD18 using 304L alloy during an Aurore tribocorrosion test.

Constants			Parameters			
				pH 5.2	pH 6.9	Units
$\rho_{metal,,}$	8	[g/cm^3]	K_{ϕ_1}	$1.61*10^{-5}$		[-]
ρ_{oxide}			K_{ϕ_2}	0.86	2.35	[-]
(Fe$_2$O$_3$)	5.24	[g/cm^3]	K_{ϕ_3}	$2*10^{-12}$		[cm^2/N]
F_N,	15	[N]	k_{ϕ_4}	$6.8*10^{-8}$		[1/s]
v_s	30	[cm/s]	k_{ϕ_5}	1		[1/s]
t_{cycle}	0.1	[s]	$a\ (d)$	0.04	0.12	[-]
			H	600000		[N/cm^2]
t$_r$	252000	[s]	k_p	$1*10^{-17}$	$2.5*10^{-16}$	[cm^2/s]
				(KD18)	(KD15)	

Table 2 Parameters values of test ST4 using Stellite 6 alloy during an Aurore tribocorrosion test.

Constants			Relevant		
ρ_{metal}	8.44	[g/cm^3]	K_{ϕ_1}	$7.15*10^{-5}$	[-]
ρ_{oxide}	5.24	[g/cm^3]	K_{ϕ_2}	2.61	[-]
(Cr$_2$O$_3$)			K_{ϕ_3}	$2*10^{-12}$	[cm^2/N]
F_N,	1	[N]	k_{ϕ_4}	$6.8*10^{-8}$	[1/s]
v_s	3	[cm/s]	k_{ϕ_5}	1	[1/s]
t_{cycle}	1	[s]	$a\ (d)$	0.4	[-]
			H	700000	[N/cm^2]
t$_r$	1000	[s]	k_p	$3.83*10^{-20}$ (pH 5.2)	[cm^2/s]

6.2.2 Mass rates laws

Table 6-3 Summary of the volume rates and mass rates with their physical laws

	Volume rate	Mass rate
Flow	$$\frac{dV}{dt} = \dot{V} \; \left[\frac{cm^3}{s}\right]$$	$$\frac{\Delta m}{\Delta t} = \dot{m} = \phi_n = \dot{V} \cdot \rho \; \left[\frac{g}{s}\right]$$
ϕ_1	$$\dot{V}_{mech} = K_{\phi_1} \cdot a(d) \cdot \frac{F_N \cdot v_s}{H}$$	$$\phi_1 = K_{\phi_1} \cdot \rho_{metal} \cdot a\,(d) \cdot F_N \cdot v_s \cdot \frac{1}{H_{in}}$$
ϕ_2	$$\dot{V}_{chem} = K_{\phi_2} \cdot \sqrt{\frac{k_p}{H}} \cdot (2 \cdot F_N)^{0.5} \cdot t_{cycle}^{0.5} \cdot v_s$$	$$\phi_2 = a \cdot K_{\phi_2} \cdot \rho_{metal} \cdot v_s \cdot \left(2 \cdot \frac{k_p}{H} \cdot F_N \cdot t_s\right)^{0.5}$$
ϕ_3	$$\dot{V}_{oxide} = K_{\phi_3} \cdot \frac{F_N \cdot v_s}{H}$$	$$\phi_3 = K_{\phi_3} \cdot \rho_{oxide} \cdot F_N \cdot v_s \cdot r_{ox}$$
ϕ_4		$$\phi_4 = k_{\phi_4} \cdot |M^o|_4$$
ϕ_5		$$\phi_5 = k_{\phi_5} \cdot |M^o|_3$$

Chapter 7 Modeling

This chapter presents the mass balance definition and its further application to solve the mathematical equations in function of different compartments:

C1   Contains mass of bulk metal

C2   Contains mass of oxidized metal on the friction film

C3   Contains mass of non oxidized metal in the friction film

C4   Contains mass of oxidized metal in water (WEAR)

The assumptions and definitions of flows performed in the precedent chapter will be used to calculate the overall behavior of the system and to compare with respect to the experimental PWR tests values (Chapter 5). It will be highlighted the importance of some critical parameters such as the friction film wear rate, hardness and the parabolic oxidation constant on the system behavior.

7.1 Mass balance

7.1.1 Generalities

The materials quantities, as they pass through processing operations, can be described in terms of material balances. The law of mass conservation stipulates mass can neither be created nor destroyed. A mass balance on a material in a system is written in a general way as presented on Eq. (7-1).

$$INPUT + Generation - OUTPUT - Consumption = Accumulation \quad \text{(7-1)}$$

Where "Input" is the mass entering through the system boundaries, "Generation" is the material produced within the system boundaries, "Output" is the material leaving through the system boundaries, "consumption" is the material consumed within the system and "accumulation" is the buildup within the system [68].

When no chemical reaction is happening on the system, the mass balance can be rewritten as (Eq. (7-2)):

$$INPUT = OUTPUT + Accumulation \quad \text{(7-2)}$$

When no accumulation occurs, two cases could be described [69]:

- A **batch process**, in which the materials are fed into the process at the outset. No material removal or addition is performed during the process time. At the end of the product is removed. During batch process the variables will change with time, so they proceed as a transient operation.
- A **continuous process**, over a time interval, is described as a process where raw materials continuously enter and product continuously leaves the process. Under these conditions the operation can be performed as transient or steady state. The latter being when the values of all variables associated with the process does not change with time.

7.1.2 Mass balance on the compartments

Regarding to the definitions cited on Section 0, the mass balance would be realized for each compartment by considering a continuous process under transient conditions [69]. The

accumulation of mass on each compartment will be calculated regarding the relation showed on Eq. (7-2). All the mass arriving to the compartment are accounted as INPUT fluxes, the mass leaving the compartment are accounted as OUTPUT and the remaining mass inside the compartment corresponds to the mass accumulation.

The mathematical description of the mass balance is expressed as a differential Eq. that evaluates the mass variation on each compartment in function time. A recapitulative of the procedure to be performed in each compartment is presented on the Figure 7-1.

Generality	$Accumulation = INPUT - OUTPUT$	(7-2)
Schema		
Differential equation	$$\frac{dM_n}{dt} = \phi_n - \phi_m$$	

Figure 7-1 Recapitulative of the mass balance procedure for each compartment, where C_n is the compartment number, ϕ_p and ϕ_q the mass rates defined with a physical law and dM_n the mass variation in a given compartment.

The differential Eq. (7-3) to (7-6) represents the mass balance on the compartments C1 to C4 according the mass diagram exposed on Chapter 3 when defining the strategy of solving this system.

C1
$$\frac{dM_1}{dt} = -\phi_1 - \phi_2$$
(7-3)

C2
$$\frac{dM_2}{dt} = \phi_2 - \phi_3 + \phi_4 + \phi_5$$
(7-4)

C3
$$\frac{dM_3}{dt} = \phi_1 - \phi_5$$
(7-5)

C4
$$\frac{dM_4}{dt} = \phi_3 - \phi_4$$
(7-6)

7.2 Resolution of differential equations

The mass balance, performed in each compartment, give an equation system of four differential equations. In order to solve them, it is considered that all the compartments are empty at the beginning (t=0s) of the process.

From the mass balance it is observed that the compartment two (C2) is the one where most of the mass flows meet. The resolution of the Eq. (7-4) will then be performed when solved M_1, M_2 and M_3.

7.2.1 Compartment 1

The Eq. (7-3) that corresponds to the first compartment is solved taking into account that all the parameters defining ϕ_1 and ϕ_2 are independent of time. The mass variation on the compartment one is described by the Eq. (7-7).

$$\frac{dM_1}{dt} = -\phi_1 - \phi_2 \qquad\qquad (7\text{-}3)$$

$$M_1(t) = \int_{t_0=0}^{t} (-\phi_1 - \phi_2)\, dt$$

$$M_1(t) = -t(\phi_1 + \phi_2) \qquad\qquad (7\text{-}7)$$

7.2.2 Compartment 3

In the case of the compartment three, the resolution of the equation is developed as it follows:

$$\frac{dM_3}{dt} = \phi_1 - \phi_5 \qquad\qquad (7\text{-}5)$$

As for the Eq. (7-3), the parameters describing ϕ_1 are independent of time. By replacing the definition of the mass flow ϕ_5 obtained on Chapter 5 on Eq. (7-5) we obtain:

$$\frac{dM_3(t)}{dt} = \phi_1 - k_5 \cdot M_3(t) \qquad\qquad (7\text{-}8)$$

The integral is then:

$$\int_{M_{3,0}}^{M_{3,f}} \frac{1}{\left(1 - \frac{k_5 \cdot M_3(t)}{\phi_1}\right)} \cdot dM_3(t) = \int_{t_o=0}^{t_f=t} \phi_1 \, dt \tag{7-9}$$

By solving the integral, we obtain:

$$M_3(t) = \left(e^{\frac{-k_5}{\phi_1}\left((\Delta t)\cdot\phi_1 - M_{3,0}\right)} - 1\right) \cdot \left(\frac{\phi_1}{-k_5}\right) \tag{7-10}$$

It was assumed that the compartments are empty at the beginning of the process, then $M_{3,0} = 0$. By replacing this value on Eq. (7-10), we obtain the mass on the compartment three (Eq. (7-11)).

$$M_3(t) = \frac{(1 - e^{-k_5 t}) \cdot \phi_1}{k_5} \tag{7-11}$$

7.2.3 Compartment 4

The mathematical resolution of the mass on the compartment four is similar to the procedure presented for the compartment three. Then the resolution sequence of the Eq. (7-6) is:

$$\frac{dM_4}{dt} = \phi_3 - \phi_4 \tag{7-6}$$

$$\frac{dM_4(t)}{dt} = \phi_3 - k_4 \cdot M_4(t) \tag{7-12}$$

$$\int_{M_{3,0}}^{M_{3,f}} \frac{1}{\left(1 - \frac{k_4 \cdot M_4(t)}{\phi_3}\right)} \cdot dM_4(t) = \int_{t_o=0}^{t_f=t} \phi_3 \, dt \tag{7-13}$$

$$M_4(t) = \frac{(1 - e^{-k_4 t}) \cdot \phi_3}{k_4} \tag{7-14}$$

7.2.4 Compartment 2

Eq. (7-4) correspond to the mass balance on the compartment two.

C2
$$\frac{dM_2}{dt} = \phi_2 - \phi_3 + \phi_4 + \phi_5 \tag{7-4}$$

By replacing ϕ_4 and ϕ_5 with the mass flow definition (Chapter 5) we obtain:

$$\frac{dM_2}{dt} = \phi_2 - \phi_3 + (k_4 \cdot M_4(t)) + (k_5 \cdot M_3(t)) \tag{7-15}$$

$M_4(t)$ and $M_3(t)$ were obtained by solving the mass balance of the compartments three and four respectively. By replacing $M_4(t)$ and $M_3(t)$ with the Eq. (7-11) and (7-14) respectively on Eq. (7-4), we obtain:

$$\frac{dM_2}{dt} = \phi_2 + \phi_3(-e^{-k_4 t}) + \left((1 - e^{-k_5 t}) \cdot \phi_1\right) \qquad (7\text{-}16)$$

$M_2(t)$ corresponds to the integral:

$$M_2(t) = \int_{t_o}^{t_f} \phi_2 \, dt - \left(\phi_3 \int_{t_o}^{t_f} e^{-k_4 t} \, dt\right) + \left(\phi_1 \int_{t_o}^{t_f} (1 - e^{-k_5 t}) \, dt\right) \qquad (7\text{-}17)$$

The initial time t_o=0s, then $M_2(t)$ is presented on Eq. (7-18) :

$$M_2(t) = \phi_2 t + \left(\phi_3 \frac{(e^{-k_4 t} - 1)}{k_4}\right) + \phi_1 \left(t + \frac{(e^{-k_4 t} - 1)}{k_5}\right) \qquad (7\text{-}18)$$

A more detailed procedure for the integral calculation is presented on the Appendix B. The mass balance resolution equations are presented on Table 7-1.

Table 7-1 Summary of the mass balance equations resolution with respect to compartments one to four.

C	Initial conditions	Equations solved	
1	$M_1(0) = 0$	$M_1(t) = -t(\phi_1 + \phi_2)$	(7-7)
2	$M_2(0) = 0$	$M_2(t) = \left(t + \dfrac{-1 + e^{-tk_5}}{k_5}\right)\phi_1 + t\phi_2 + \left(\dfrac{-1 + e^{-tk_4}}{k_4}\right)\phi_3$	(7-18)
3	$M_3(0) = 0$	$M_3(t) = \dfrac{(1 - e^{-tk_5})\phi_1}{k_5}$	(7-11)
4	$M_4(0) = 0$	$M_4(t) = \dfrac{(1 - e^{-tk_4})\phi_3}{k_4}$	(7-14)

C: compartment number

7.3 Mathematica software model interface

Mathematica is a software system and computer language for use in mathematical applications. This software can be used to perform operations on functions, to do calculus and to manipulate algebraic formulas. This latter was used in the context of this chapter in order to better visualize the mass behavior on each compartment depending on the parameters values.

The graphical interface that was developed is presented on Figure 7-2 (with arbitrary values). It can be divided in two sections: The first, Figure 7-2a, correspond to the plot of the metal mass variation (mg) in function of time (s) for all the compartments simultaneously. The second part, Figure 7-2b, presents the different parameters and their values. They were classified in function of the laws corresponding to each mass flow. The values of the parameters can be treated as individual values or varied with a bar that slides between two given values (#1). The color code for each compartment is presented on the lower right part. The equations that are represented on this tool correspond to the equations obtained after the mass balance on each compartment (Table 7-1) and the mass flows law presented on Chapter 5.
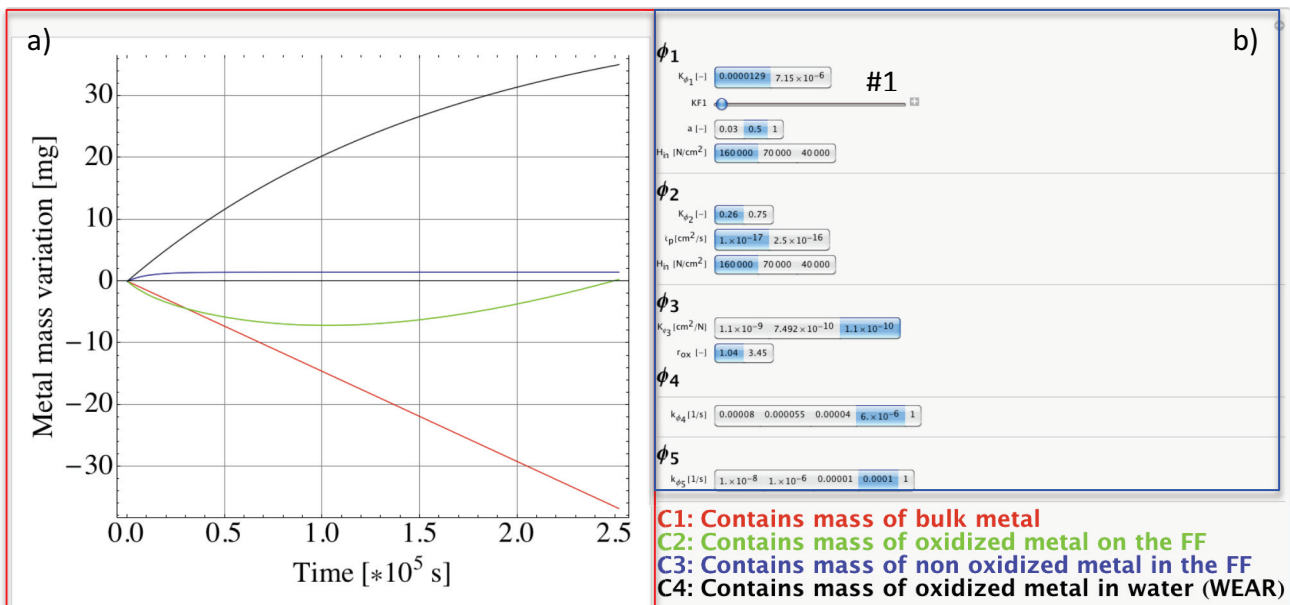

Figure 7-2 Interface showing the overall behavior of the system using Mathematica software. a) Plot of the metal mass variation in function of time. It shows the evolution of each compartment with time. b) Parameters to choose that belong to each mass rate flow. Right bottom: the compartments names with their color code. Parameters values are arbitrary.

7.4 Model predictions vs Aurore tests

- **304L alloy**

The validity of the model is verified by applying the parameters obtained in the previous chapter when discussing the mass flows (Chapter 6). Three different tests conditions are considered. The two first concerns the tests series KD18 (pH 5.2) and KD 15 (pH 6.9) performed with the protocol B using 304L steel; the third one is the test ST4 performed with the protocol A and using Stellite 6 alloy (Chapter 5). The test parameters were summarized at the end of the precedent chapter (Chapter 6). The obtained model predictions for the stainless s steel (KD15 and KD18) are plotted in Figure 7-3.
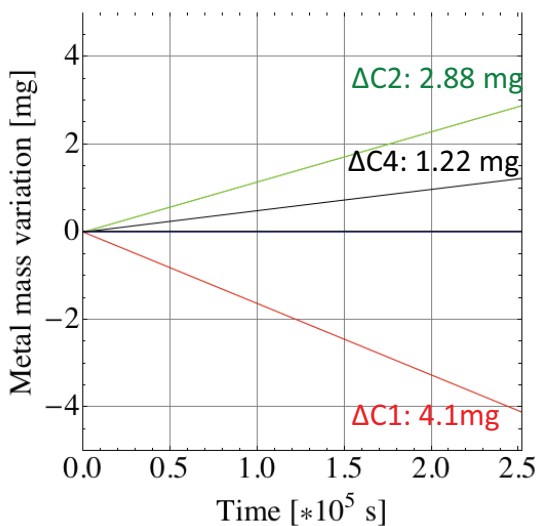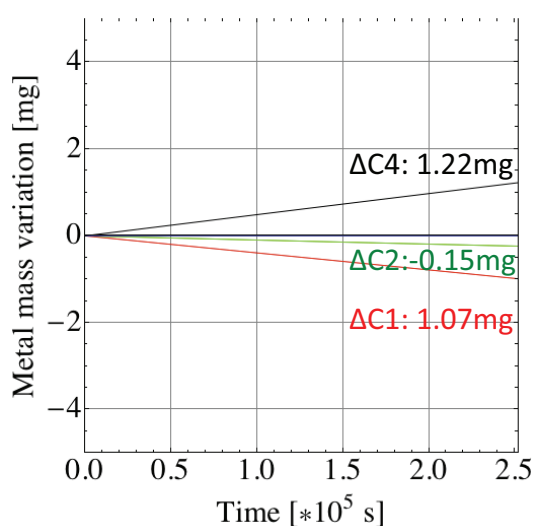
a) pH 7   b) pH 5

Figure 7-3 Compartments behavior of C1 (red), C2 (green), C3 (blue) and C4 (black) for the tests a) KD 15 and b) KD18. The value of the constant K_{ϕ_3} is $2*10^{-12}$ [cm^2/N], parameters values are on Chapter 6.

The evolution of the mass in Compartment 4 reflects the evolution of the overall mass loss due to wear. No difference between the two pH values can be observed on wear, which reaches after 0.25 Ms the value of 1.22 mg. The absence of a pH effect on wear is not surprising since the mass balance in the compartment 4 is essentially controlled by the wear coefficient of the oxide K_{ϕ_3}, which is kept constant for both pH values, despite the fact that film properties are pH dependent [12]. However, small variation in this coefficient may significantly change wear, as shown in the next chapter. Nevertheless, the calculated total wear (1.22 mg) is very surprisingly close as the experimentally determined ones (17 mg for KD18 at pH 5.2 and 2 mg for KD15 at pH 7). Clearly,

the K_{ϕ_3} value extracted from literature data is a quite close, although underestimating, approximation of the real values.

The green line on Figure 7-3 represents the mass variation of the friction film (C2). The model predicts an increase in mass of the friction film formed at pH 6.9 up to 2.88mg (corresponding to a thickness change of ~17µm). In contrast a diminution of the mass is observed when passing to pH5 and reaching even negative values -0.15 mg (corresponding to a thickness change of ~-0.9µm). This tendency is in qualitative agreement with the thickening by 255 nm of the oxide film found inside of the wear track compared to the rest of the sample. In test KD18 at pH 5, the thickness remains similar inside and outside the wear track; this corresponds to the model prediction of a smaller mass change of Compartment 3. The calculated friction film mass variations are quite high compared to the experimental observations. This is most likely relate to the underestimated wear rate of the oxide film introduced by the approximate K_{ϕ_3} value used in the calculations. The effect of this parameter on friction film thickness is discussed in the next chapter. Again, the K_{ϕ_3} appears to constitute one of the key parameters determining the evolution of overall wear and of the friction film.

The compartment 3 (blue) is not observable in Figure 7-3 because its value is close to zero and overlaps with the abscissa. This negligible value is a consequence of the immediate conversion within the friction film of metal into oxide, as assumed by taking a large value of K_{ϕ_4} as effectively done in the present study. This issue will be discussed in the next section.

- **Stellite 6 alloy**

In order to observe the influence of the material regarding the mathematical model, a test using Stellite 6 alloy parameters is now presented. It is assumed that the same re-deposition kinetics (constant k_{ϕ_4}) applies for Stellite alloys and stainless steel. The parameters values concerning the test ST4 are summarized in Chapter 6. Model predictions are illustrated in Figure 7-4.
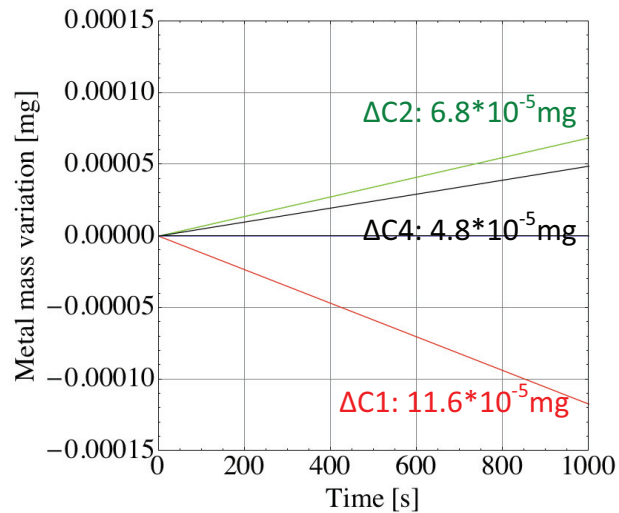
Figure 7-4 Compartments behavior of C1 (red), C2 (green), C3 (blue) and C4 (black) for the tests ST4 (Stellite 6). The value of the constant K_{ϕ_3} is $2*10^{-12}$ [cm²/N].

The model predicts for a test duration of 1000s a total wear volume of $4.8 \cdot 10^{-5}$ mg which is very close to the experimental values of $1.65*10^{-4}$ mg of metal (Chapter 5). This supports the validity of the model. The model predicts an increase on the friction film of $6.8*10^{-5}$ mg (~0.28nm). The experimental oxide variation at the end of the test show a difference of 15 nm, 50 times more to what is predicted by the model. According to the model, the amount of material lost by the substrate metal (compartment 3-red line) is mainly accumulated in the friction film and transferred to Compartment 4 as in the of the 304L steel at pH7 (Figure 7-3a).

7.5 Parameters influence

In the previous section discrepancy between experimental results and model predictions highlighted the effect of certain parameters and the need to control them in a precise manner. In order to determine the influence of parameters on the overall compartment behavior; the friction film wear rate K_{ϕ_3}, the hardness H, the parabolic oxidation constant k_p and the rate constant k_{ϕ_5} are evaluated in the followings. For comparison purposes, the system 304L alloy at pH 5.2 is taken as reference for the defaults values of the different parameters kept constant (for these conditions see Chapter 6).

7.5.1   Friction wear rate K_{ϕ_3}

Figure 7-5 shows the evolution of the compartments when varying the friction film wear rate determining parameter K_{ϕ_3}. The Figure 7-5a presents a general overview of the behavior while Figure 7-5b is a zoom into the main changes. No significant changes are observed when varying the K_{ϕ_3} from $1*10^{-16}$ cm^2/N up to $1*10^{-12}$ cm^2/N. In contrast, above $1*10^{-12}$ the friction film (green line) switches from a positive to a negative metal mass variation. This behavior is accompanied by an acceleration of mass loss on the compartment 4 (C4). No influence of K_{ϕ_3} is observed on compartment C1 and C3.
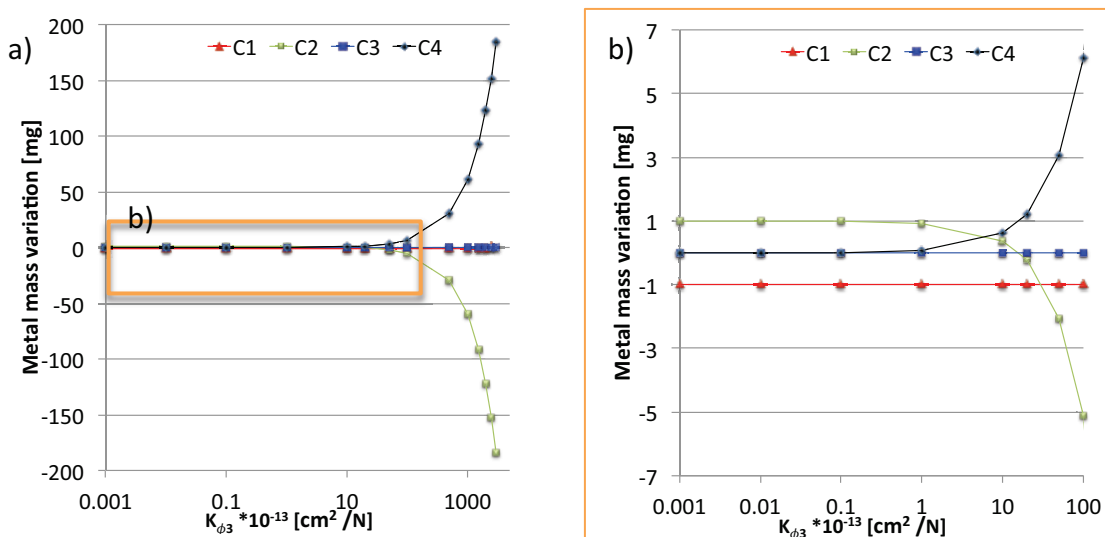

Figure 7-5 Influence of K_{ϕ_3} on the different compartment behavior (x axis in logarithmic scale)

The model shows that by changing one order of magnitude on the friction film wear rate can results on a significant acceleration of the overall wear rate. Moreover, the friction film is

consumed and at a given moment, it appears not to regenerate as fast as its wears. As a consequence the friction film start thinning.

7.5.2 Parabolic oxidation constant kp

Figure 7-6 shows the evolution of the compartments as a function of the parabolic oxidation constant. Changing the parabolic oxidation constant does not affect the wear compartments 4 (C4) and 3 (C3). The model shows that the variation in mass of compartments 1 and 2 is stable up to $1*10^{-16}$ cm^2/s, i.e. a value close to the K_p of 304L steel at 325°C [32]. At this point an inflexion on the friction film evolution (green line) is observed and an exponential growth is observed for higher k_p values. This can be explained by the fact that below this transition metal oxidation is not rapid enough to fully compensate the wearing off of the friction film. Above the transition the oxidation rate exceeds the wear rate and thus the film thickens. Thus, for carbon steel (kp $1*10^{-15}$ cm^2/s [ ] the model anticipates the build up of much thicker films than in case of 304L steel. This confirms that the oxidation behavior of steel plays a crucial role in the degradation in PWR conditions.
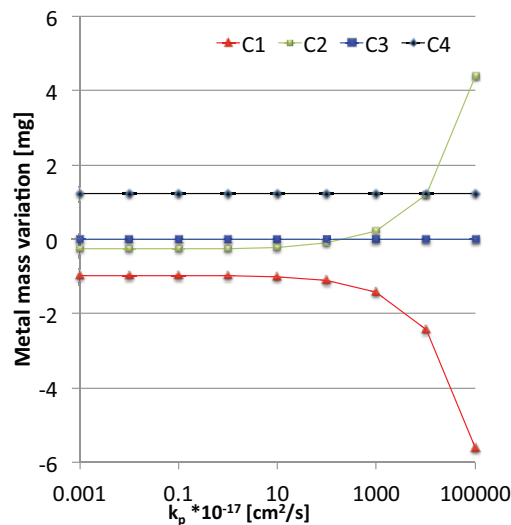

Figure 7-6 Influence of the parabolic oxidation constant on the compartment behavior. For comparison purposes, the other constants and parameters were fixed as presented for pH5.2 conditions (Chapter 6).(x axis in logarithmic scale)

7.5.3 Hardness H

Figure 7-7 shows the evolution of the mass compartments when varying the hardness of the metal. It is observed that increasing hardness reduces the metal mass variation on the friction film (green-line). It is clearly observed that from 500HV, the friction film starts to loss mass. This diminution is observed up to a plateau that is reached from 1300HV. At his point the mass loss of the friction film does not go below 1mg. In the case of the compartment 1 (C1), it is observed that when increasing the hardness, the mass loss is decreased up to a plateau approximately at -0.5mg. This compartment (C1) is observed to always loose material that is mainly changing the friction film evolution.
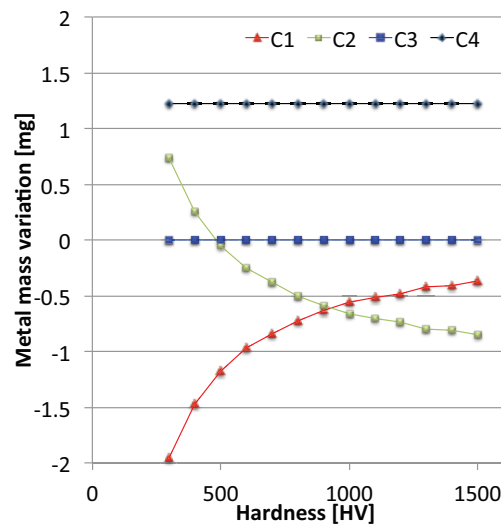
Figure 7-7 Influence of the hardness on the compartment behavior

The model shows that a harder material could decrease the sources flow. In fact a softer material is easier to deform plastically and as consequence more efficiently feeds the friction film. The model shows that, under these conditions, wear is not affected by the hardness of the material. Nevertheless it is directly related to the friction film evolution and to the source flows.

7.5.4 Constant rate k_{ϕ_5}

Figure 7-8 shows the evolution of the mass compartments when varying the constant rate k_{ϕ_5}. This described the transfer between the compartment 3 (C3) and 2 (C2) inside the friction film. In others words, it determines the oxidation of metal particles inside the friction film. The model shows that this parameter influences only the compartment to which it communicates (C3 and C2). It appears that until 10 000s ($1*10^{-4}$ s^{-1}) for oxidation time, not clear change is observed on the compartments behavior. For times decreasing up to $1*10^6$ seconds an increase of 0.3mg is observed which is also reflected on the friction film mass variation.
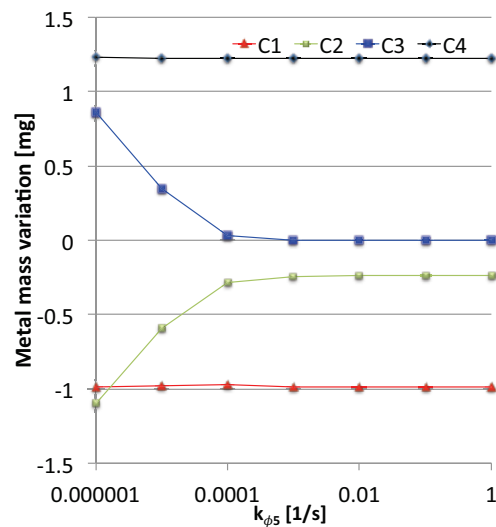
Figure 7-8 Influence of the constant rate k_{ϕ_5} on the compartment behavior (x-axis in logarithmic scale)

It is observed that under these considerations, k_{ϕ_5}, is not a as crucial parameters as the previously described ones. Nevertheless, one has to keep in mind that the effect of one parameter is linked to the overall system and can thus have a larger impact when other parameters, kept constant in these simulations, change.

7.6 Conclusions

In conclusion the mathematical model built using the physical laws and assembled defining compartment mass variation showed that:

- The model constitutes a valuable frame to appraise the interaction of physical parameters determining the tribocorrosion according to well-defined physical mechanisms.

- The properties of the friction film are determinant for the wear loss behavior of the alloy under tribocorrosion conditions.

- The increase of thickness of the friction film can be related to the growth kinetics of the alloy and not only to the pH re-deposition phenomena.

- The model shows that parameters such as oxide wear rate (K_{ϕ_3}) play a crucial role and need therefore to be determined and controlled.

Chapter 8   Conclusion and perspectives

This work presents an attempt to model tribocorrosion of metals in high temperature pressurized water as encountered in pressurized water reactors of power plants. Under these conditions, tribocorrosion is characterized by the complex interaction of plastic deformation of the metal, surface oxidation and build up of friction films. An analysis of the existing literature showed that this tribocorrosion system can be described by a multilayer structure involving the substrate metal undergoing work hardening, a mechanically mixed friction film containing oxidized and non oxidized metal and, finally, the water solution. The wear process in such a structure can be described through mass flows according to the third body approach of tribology. In this work, wear is described using five interrelated flows. The two first were defined as source flows from the substrate metal to the friction film (oxide and metal particles mixed mechanically). They describe the introduction of metal or oxidized particles into the friction film. Inside this latter, another flow describes the transformation of metal particles into oxide. Subsequently, two other flows illustrate the expulsion and particles re-deposition respectively from the friction film.

The flows were described using wear physical approaches based on mechanical deformation of the asperities. They were formulated by mirror techniques that permitted to illustrate the mechanical (Archard) and chemical (tribocorrosion model) behavior of the system taking into account materials aspects. The remaining flows that could not be experimentally developed were approximated using literature data and/or first order kinetics law. The utilization of physical laws permitted to describe wear rate as a function of clearly identifiable parameters. All these laws were interrelated using a mass balance approach that permit to solve differential equation systems in each connection point (compartments) where flows meet: bare metal, friction film or external environment.

The model showed that wear is directly related to the mechanical characteristics of the friction film. According to the available experimental data, only 2% of the total particles ejected redeposit on the friction film. As a consequence the wear properties of the friction film appears to play a key role on the overall wear rate. Thus tailored experiments should specifically focus on this issue.

The parameters analysis using the proposed model showed that hardness of the metal is not directly related to the overall wear rate. Nevertheless, it affects the inclusion of particles from the substrate metal into the friction film and in consequence it could change the mechanical behavior of the friction film. This analysis accounts for a thick friction film (1µm) such as observed for stainless steel. But in the case of thinner films, such as in Stellite 6, the hardness of the substrate metal becomes a crucial factor for wear. Indeed, in this case the thinner film cannot provide sufficient attenuation and thus a harder metal can bear a larger fraction of the load without wearing. Because of the dynamic nature of the friction film, its attenuation capability as a function of time should be taken into account for improving the proposed model.

The proposed model should be considered as a continuously evolving mathematical tool enabling the physical interpretation of a given phenomena. It could be applied to different systems independently on the geometry, which would help developing further insights on the flows schema and discriminating critical parameters

In general, the model has shown to constitute a promising tool for appraising the interaction of crucial material, mechanical and electrochemical parameters. It can be used to efficiently design test campaigns and to anticipate and analyze the effect of specific parameters in a variety of conditions.

For further studies, it could be interesting to develop the model by using the structural identifiability principle. Such approach could permit to perform a parameter sensitivity evaluation and mathematically identify the significance of specific parameters under given tests conditions.

References

1.   Wirt J: **A Federal Demonstration Project: N.S. Savannah, in Maritime Transportation Research Board , National Research Council (U.S.)**. *Innovation in the maritime Industry* 1979, **1**:29-36.

2.   Boczar PG: **11 - CANDU nuclear reactor designs, operation and fuel cycle**. In: *Nuclear Fuel Cycle Science and Engineering.* Edited by Crossland I: Woodhead Publishing; 2012: 278-299.

3.   Nordman F: **Aspects on chemistry in French Nuclear Power Plants**. *14th International Conference on the Properties of Water and Steam (ICPWS) Kyoto, Japan, August 29* 2004.

4.   **Water chemistry of nuclear reactor system 8: proceedings of the conference organized by the Nuclear Energy Society**, vol. 1 and 2. Bournemouth: British Nuclear Energy Society; 2000.

5.   Lister DH, Davidson RD, Mcalpine E: **The Mechanism and Kinetics of Corrosion Product Release from Stainless-Steel in Lithiated High-Temperature Water**. *Corros Sci* 1987, **27**(2):113-140.

6.   Kim HK, Kim SJ, Yoon KH, Kang HS, Song KN: **Fretting wear of laterally supported tube**. *Wear* 2001, **250**:535-543.

7.   Lina A, Moinereau D, Delaune X, Phalippou C, Reynier B, Riberty P: **The influence of water flow on the impact/sliding wear and oxidation of PWR control rods specimens**. *Wear* 2001, **251**:839-852.

8.   Kaczorowski D, Vernot JP: **Wear problems in nuclear industry**. *Tribol Int* 2006, **39**(10):1286-1293.

9.   Le Calvar M, Lemaire E: **Evidence of tribocorrosion wear in pressurized water reactors**. *Wear* 2001, **249**(5-6):338-344.

10.   Hertz D: **Approach to analysis of wear mechanisms in the case of RCCAs and CRDM latch arms: From observation to understanding**. *Wear* 2006, **261**(9):1024-1031.

11.   Waseem, Elahi N, Siddiqui A, Murtaza G: **Fuel rod-to-support contact pressure and stress measurement for CHASNUPP-1(PWR) fuel**. *Nucl Eng Des* 2011, **241**(1):32-38.

12.   Kaczorowski D: **Usures d'un acier inoxidable austénitique dans l'eau à haute pression et haute tempeérature**. 2002.

13.   Landolt D, Mischler S: **Tribocorrosion of passive metals and coatings**: Woodhead Publishing; 2011.

14.   Dupin M, Gosser P, Walls MG, Rondot B, Pastol JL, Faty S, Ferreira MGS, Belo MDC: **Influence of pH on the chemical and structural properties of the oxide films formed on 316L stainless steel, alloy 600 and alloy 690 in high temperature aqueous environments**. *Ann Chim-Sci Mat* 2002, **27**(1):19-32.

15.   Kritzer P, Boukis N, Dinjus E: **Factors controlling corrosion in high-temperature aqueous solutions: a contribution to the dissociation and solubility data influencing corrosion processes**. *J Supercrit Fluid* 1999, **15**(3):205-227.

16.   Kaczorowski D, Combrade P, Vernot JP, Beaudouin A, Crenn C: **Water chemistry effect on the wear of stainless steel in nuclear power plant**. *Tribol Int* 2006, **39**(12):1503-1508.

17.   Kaczorowski D, Georges JM, Bec S, Tonck A, Vannes AB, Vernot JP: **Wear of a stainless steel in pressurised high temperature water**. *Cr Acad Sci Iv-Phys* 2001, **2**(5):739-747.

18.   Ziemniak SE, Hanson M: **Corrosion behavior of 304 stainless steel in high temperature, hydrogenated water**. *Corros Sci* 2002, **44**(10):2209-2230.

19.   Landolt D: **Corrosion and Surface Chemistry of Metals**; 2006.

20.   Quinn TFJ: **Review of Oxidational Wear .1. The Origins of Oxidational Wear**. *Tribol Int* 1983, **16**(5):257-271.

21.   Kermouche G, Kaiser AL, Gilles P, Bergheau JM: **Combined numerical and experimental approach of the impact-sliding wear of a stainless steel in a nuclear reactor**. *Wear* 2007, **263**:1551-1555.

22.   Kim SJ, Lee KY, Kim GG, Kim JH, Lee SH: **Sliding wear behavior of hardfacing alloys in a pressurized water environment**. *Wear* 2007, **262**(7-8):845-849.

23.   Mischler S: **Triboelectrochemical techniques and interpretation methods in tribocorrosion: A comparative evaluation**. *Tribol Int* 2008, **41**(7):573-583.

24.   Landolt D, Mischler S, Stemp M: **Electrochemical methods in tribocorrosion: a critical appraisal**. *Electrochim Acta* 2001, **46**(24-25):3913-3929.

25.   Mischler S, Munoz AI: **Wear of CoCrMo alloys used in metal-on-metal hip joints: A tribocorrosion appraisal**. *Wear* 2013, **297**(1-2):1081-1094.

26.   Godet M: **The 3rd-Body Approach - a Mechanical View of Wear**. *Wear* 1984, **100**(1-3):437-452.

27.   Berthier Y, Vincent L, Godet M: **Velocity Accommodation Sites and Modes in Tribology**. *Eur J Mech a-Solid* 1992, **11**(1):35-47.

28.   Descartes S, Berthier Y: **Rheology and flows of solid third bodies: background and application to an MoS1.6 coating**. *Wear* 2002, **252**(7-8):546-556.

29. Landolt D, Mischler S, Stemp M, Barril S: **Third body effects and material fluxes in tribocorrosion systems involving a sliding contact**. *Wear* 2004, **256**(5):517-524.

30. Rigney DA, Hirth JP: **Plastic-Deformation and Sliding Friction of Metals**. *Wear* 1979, **53**(2):345-370.

31. Kaiser AL: **Caractérisation tribologique d'un acier inoxydable sollicités en impact-glissement dans un environnement sévère**. Central School of Lyon; 2005.

32. J.Perret: **Modélisation de la tribocorrosion d'aciers inoxidables dans l'eau à haute pression et haute température**. Lausanne: EPFL; 2010.

33. Sharma G, Limaye PK, Jadhav DT: **Sliding wear and friction behaviour of zircaloy-4 in water**. *J Nucl Mater* 2009, **394**(2-3):151-154.

34. Lee YH, Kim IS: **The effect of subsurface deformation on the wear behavior of steam generator tube materials**. *Wear* 2002, **253**(3-4):438-447.

35. Lee YH, Kim HK, Jung YH: **Effect of impact frequency on the wear behavior of spring-supported tubes in room and high temperature distilled water**. *Wear* 2005, **259**(1-6):329-336.

36. Kim IS, Hong SM: **Impact fretting wear of alloy 690 tubes at 25 degrees C and 290 degrees C**. *Wear* 2005, **259**(1-6):356-360.

37. Kim HK, Lee YH, Lee KH: **On the geometry of the fuel rod supports concerning a fretting wear failure**. *Nucl Eng Des* 2008, **238**(12):3321-3330.

38. Kim KT: **The study on grid-to-rod fretting wear models for PWR fuel**. *Nucl Eng Des* 2009, **239**(12):2820-2824.

39. Kitaoka S, Tsuji T, Yamaguchi Y, Kashiwagi K: **Tribochemical wear theory of non-oxide ceramics in high-temperature and high-pressure water**. *Wear* 1997, **205**(1-2):40-46.

40. Frick T: **Overview on the development and implementation of methodologies to compute vibration and wear of steam generator tubes**. *ASME Symposium on Flow-Induced Vibration* 1984, **3**:149-161.

41. Kim HK, Lee YH: **Wear depth model for thin tubes with supports**. *Wear* 2007, **263**:532-541.

42. Yan J, Yuan K, Tatli E, Karoutas Z: **A new method to predict Grid-To-Rod Fretting in a PWR fuel assembly inlet region**. *Nucl Eng Des* 2011, **241**(8):2974-2982.

43. Favero M, Stadelmann P, Mischler S: **Effect of the applied potential of the near surface microstructure of a 316L steel submitted to tribocorrosion in sulfuric acid**. *J Phys D Appl Phys* 2006, **39**(15):3175-3183.

44. Perret J, Boehm-Courjault E, Cantoni M, Mischler S, Beaudouin A, Chitty W, Vernot JP: **EBSD, SEM and FIB characterisation of subsurface deformation during tribocorrosion of stainless steel in sulphuric acid**. *Wear* 2010, **269**(5-6):383-393.

45. Bidiville A, Favero M, Stadelmann P, Mischler S: **Effect of surface chemistry on the mechanical response of metals in sliding tribocorrosion systems**. *Wear* 2007, **263**:207-217.

46. Buscher R, Tager G, Dudzinski W, Gleising B, Wimmer MA, Fischer A: **Subsurface microstructure of metal-on-metal hip joints and its relationship to wear particle generation**. *J Biomed Mater Res B* 2005, **72B**(1):206-214.

47. Xu Yangtao XT, Huang Yanling: **Microstructures Comparison of Stellite 6 Alloy by Self-Propagating High-Temperature Synthesis and Cast HS111 Alloy** *Rare Metal Materials and Engineering* 2009, **38**(8):1333-1337.

48. Yu H, Ahmed R, Lovelock HD, Davies S: **Influence of Manufacturing Process and Alloying Element Content on the Tribomechanical Properties of Cobalt-Based Alloys**. *J Tribol-T Asme* 2009, **131**(1).

49. Benea L, Ponthiaux P, Wenger F, Galland J, Hertz D, Malo JY: **Tribocorrosion of stellite 6 in sulphuric acid medium: electrochemical behaviour and wear**. *Wear* 2004, **256**(9-10):948-953.

50. Munoz AI, Julian LC: **Influence of electrochemical potential on the tribocorrosion behaviour of high carbon CoCrMo biomedical alloy in simulated body fluids by electrochemical impedance spectroscopy**. *Electrochim Acta* 2010, **55**(19):5428-5439.

51. Stojadinovic J, Bouvet D, Declercq M, Mischler S: **Effect of electrode potential on the tribocorrosion of tungsten**. *Tribol Int* 2009, **42**(4):575-583.

52. Jemmely P, Mischler S, Landolt D: **Electrochemical modeling of passivation phenomena in tribocorrosion**. *Wear* 2000, **237**(1):63-76.

53. Hodgson AWE, Kurz S, Virtanen S, Fervel V, Olsson COA, Mischler S: **Passive and transpassive behaviour of CoCrMo in simulated biological solutions**. *Electrochim Acta* 2004, **49**(13):2167-2178.

54. Vidal CV, Munoz AI, Olsson COA, Mischler S: **Passivation of a CoCrMo PVD Alloy with Biomedical Composition under Simulated Physiological Conditions Studied by EQCM and XPS**. *J Electrochem Soc* 2012, **159**(5):C233-C243.

55. Stemp M, Mischler S, Landolt D: **The effect of mechanical and electrochemical parameters on the tribocorrosion rate of stainless steel in sulphuric acid**. *Wear* 2003, **255**:466-475.

56. Gahr K-HZ: **Microstructure and wear of materials**, vol. 10; 1987.

57. A. Igual Muñoz NE: **Tribocorrosion mechanisms in sliding contacts**. In: *Tribocorrosion of passive metals and coatings.* Edited by D Landolt and S Mischler: Woodhead Publiushing Limited; 2011.

58. Mischler S, Spiegel A, Landolt D: **The role of passive oxide films on the degradation of steel in tribocorrosion systems**. *Wear* 1999, **229**:1078-1087.

59. Mischler S, Spiegel A, Stemp M, Landolt D: **Influence of passivity on the tribocorrosion of carbon steel in aqueous solutions**. *Wear* 2001, **250**:1295-1307.

60. Espallargas N, Mischler S: **Tribocorrosion behaviour of overlay welded Ni-Cr 625 alloy in sulphuric and nitric acids: Electrochemical and chemical effects**. *Tribol Int* 2010, **43**(7):1209-1217.

61. Barril S, Mischler S, Landolt D: **Triboelectrochemical investigation of the friction and wear behaviour of TiN coatings in a neutral solution**. *Tribol Int* 2001, **34**(9):599-608.

62. Hutchings: **Tribology: friction and wear of engineering materials**; 1992.

63. Dahm KL: **Direct observation of the interface during sliding tribo-corrosion**. *Tribol Int* 2007, **40**(10-12):1561-1567.

64. **Tribocorrosion issues in nuclear power generation**. In: *Triborrosion of passive metals and coatings.* Edited by Landolt DM, S: Woodhead Publishing Limited; 2011.

65. Kapoor SL, R: Wu, X. J.;Yao, M. X.: **Temperature-Dependence of Hardness and Wear Resistance of Stellite Alloys**. *World Academy of Science, Engineering & Technology* 2012(68):2015.

66. Gates RS, Hsu SM: **Silicon-Nitride Boundary Lubrication - Lubrication Mechanism of Alcohols**. *Tribol T* 1995, **38**(3):645-653.

67. Jeffrey I. Steinfeld JSF, William L. Hase: **Chemical kinetics and dynamics**; 1999.

68. Rousseau RMFRW: **Elementary Principles of Chemical Processes**; 2004.

69. Bearup DJ, Evans ND, Chappell MJ: **The input-output relationship approach to structural identifiability analysis**. *Comput Meth Prog Bio* 2013, **109**(2):171-181.

Apendix

Apendix A : Mathematica code

- Resolution of differential equations :

```
Exit[]
```

Main Equations (fluxes)

```
eq1 := M1'[t] == -ϕ₁ - ϕ₂
eq2 := M2'[t] == ϕ₂ - ϕ₃ + k₄ M4[t] + k₆ M3[t]
eq3 := M3'[t] == ϕ₁ - k₆ M3[t]
eq4 := M4'[t] == ϕ₃ - k₄ M4[t]
```

Solving differential equations

```
DSolve[{eq1, eq2, eq3, eq4}, {M1[t], M2[t], M3[t], M4[t] },
 t]
```

$$\left\{\left\{M1[t] \to C[1] + t\,(-\phi_1 - \phi_2),\right.\right.$$

$$M2[t] \to C[2] + e^{-t\,k_6}\left(-1 + e^{t\,k_6}\right) C[3] + e^{-t\,k_4}\left(-1 + e^{t\,k_4}\right) C[4] +$$

$$t\,\phi_1 - \frac{e^{t\,k_6}\,\phi_1}{k_6} + \frac{\left(-1 + e^{t\,k_6}\right)\,\phi_1}{k_6} + t\,\phi_2 - \frac{e^{t\,k_4}\,\phi_3}{k_4} + \frac{\left(-1 + e^{t\,k_4}\right)\,\phi_3}{k_4},$$

$$M3[t] \to e^{-t\,k_6}\,C[3] + \frac{\phi_1}{k_6}, \quad M4[t] \to e^{-t\,k_4}\,C[4] + \frac{\phi_3}{k_4}\left.\right\}\right\}$$

```
FullSimplify[%]
```

$$\left\{\left\{M1[t] \to C[1] - t\,(\phi_1 + \phi_2),\right.\right.$$

$$M2[t] \to C[2] + C[3] - e^{-t\,k_6}\,C[3] + C[4] - e^{-t\,k_4}\,C[4] + \left(t - \frac{1}{k_6}\right)\phi_1 + t\,\phi_2 - \frac{\phi_3}{k_4},$$

$$M3[t] \to e^{-t\,k_6}\,C[3] + \frac{\phi_1}{k_6}, \quad M4[t] \to e^{-t\,k_4}\,C[4] + \frac{\phi_3}{k_4}\left.\right\}\right\}$$

Initial conditions

Solving differential equations with given initial conditions

```
DSolve[{eq1, eq2, eq3, eq4, M1[0] == 0, M2[0] == 0, M3[0] == 0,
  M4[0] == 0}, {M1[t], M2[t], M3[t], M4[t]}, t]
```

$$\Big\{\Big\{M1[t] \to -t\ (\phi_1 + \phi_2),$$

$$M2[t] \to \frac{1}{k_4\ k_6}\ e^{-t\,k_4 - t\,k_6}\ \Big(e^{t\,k_4}\ k_4\ \phi_1 - e^{t\,k_4 + t\,k_6}\ k_4\ \phi_1 + e^{t\,k_4 + t\,k_6}\ t\ k_4\ k_6\ \phi_1 +$$

$$e^{t\,k_4 + t\,k_6}\ t\ k_4\ k_6\ \phi_2 + e^{t\,k_6}\ k_6\ \phi_3 - e^{t\,k_4 + t\,k_6}\ k_6\ \phi_3\Big),$$

$$M3[t] \to \frac{e^{-t\,k_6}\ \left(-1 + e^{t\,k_6}\right)\ \phi_1}{k_6}\ ,\ M4[t] \to \frac{e^{-t\,k_4}\ \left(-1 + e^{t\,k_4}\right)\ \phi_3}{k_4}\Big\}\Big\}$$

```
FullSimplify[%]
```

$$\Big\{\Big\{M1[t] \to -t\ (\phi_1 + \phi_2),\ M2[t] \to \left(t + \frac{-1 + e^{-t\,k_6}}{k_6}\right)\ \phi_1 + \frac{t\ k_4\ \phi_2 + \left(-1 + e^{-t\,k_4}\right)\ \phi_3}{k_4},$$

$$M3[t] \to \frac{\left(1 - e^{-t\,k_6}\right)\ \phi_1}{k_6}\ ,\ M4[t] \to \frac{\left(1 - e^{-t\,k_4}\right)\ \phi_3}{k_4}\Big\}\Big\}$$

- • Code Mathematica

Parameters definition depending on the tests conditions

Variation parameters by compartment					
Parameters values					

```
Parameters[ρ_metal = 8, KF1 = 1.29 * 10⁻⁵, a = 0.03, F_N = 15, v_s = 30, H = 160000, KF2 = 0.26, kP = 1 * 10⁻¹⁷,
    s = 0.1, rox = 1.04, KF3 = 0.91 * 10⁻⁹, KF301 = 0.91 * 10⁻⁹, KF302 = 0.91 * 10⁻⁹, KF303 = 0.91 * 10⁻⁹, ρ_oxide = 5.24];

(*Values*)
Grid[{{"ρ_metal [g/cm³]" , "K_F1 [-]", "a [-]", "F_N [N]", "v_s [cm/s]", "Hardness [N/cm²]"},
    { ρ_metal, KF1, a, F_N, v_s, H }, {},
    { "K_F2 [-]", "kp [cm²s⁻¹]", "Stroke time [s]", "Ratio [-]", "K_F3 [cm²/N]" , "ρ_oxide [g/cm³]"},
    {KF2, kP, s, rox, KF3, ρ_oxide}}, Frame → All]
```

ρ_{metal} [g/cm³]	K_{F1} [-]	a [-]	F_N [N]	v_s [cm/s]	Hardness [N/cm²]
8	0.0000129	0.03	15	30	160 000
K_{F2} [-]	kp [cm²s⁻¹]	Stroke time [s]	Ratio [-]	K_{F3} [cm²/N]	ρ_{oxide} [g/cm³]
0.26	1 / 100 000 000 000 000 000	0.1	1.04	9.1×10^{-10}	5.24

Mathematica code for protocol B (KD series)

```
<< PlotLegends`
Manipulate[
  Plot[{- (t * 100 000) ((KF1 * ρ_metal * a * F_N * v_s * 1/H) + (KF2 * a * ρ_metal * (kP / H)^0.5 * (2 * F_N * s)^0.5 * v_s)) * 10³,

    (((t * 100 000) + (-1 + e^(-(t*100000)*k5))/k5) * (KF1 * ρ_metal * a * F_N * v_s * 1/H) +

    1/k4 (((t * 100 000) * k4 * a * (KF2 * ρ_metal * (kP / H)^0.5 * (2 * F_N * s)^0.5 * v_s)) + ((-1 + e^(-(t*100000)*k4)) * ((KF3) * (ρ_oxide * rox) * (F_N * v_s))))) * 10³,

    (1 - e^(-(t*100000)*k5)) (KF1 * ρ_metal * a * F_N * v_s * 1/H)/k5 * 10³, (1 - e^(-(t*100000)*k4)) ((KF3) * (ρ_oxide * rox) * (F_N * v_s))/k4 * 10³}, {t, 0, 2.52},

    PlotRange → {{0, 2.52}, Automatic}, PlotStyle → {Red, Green, Blue, Black}, Frame → True, FrameLabel → {"Time [*10⁵ s]", "Metal mass variation [mg]"},
    LabelStyle → Directive[FontSize → 30], ImageSize → Scaled[0.3], AspectRatio → 1, GridLines → Automatic
  ],

  Style["φ₁", Bold, Large], {{KF1, 1.61 * 10⁻⁵, "K_φ₁[-]"}, {1.61 * 10⁻⁵, 0.715 * 10⁻⁵}}, {{a, 0.044, "a [-]"} , {0.044, 0.14, 1, 0.9}}, {{a, 0.044, 1}},
  {{H, 1 600 000, "H_in [N/cm²]"}, {1 600 000, 70 000, 40 000, 17 000}}, {H, 1 600 000, 200 000}, Delimiter,
  Style["φ₂", Bold, Large], {{KF2, 0.86, "K_φ₂[-]"}, {0.86, 2.35}}, {{kP, 1.0 * 10⁻¹⁷, "k_p[cm²/s]"}, {1.0 * 10⁻¹⁷, 2.5 * 10⁻¹⁶}}, {{kP, 1.0 * 10⁻¹⁴, 1.0 * 10⁻²⁰}},
  {{H, 1 600 000, "H_in [N/cm²]"}, {1 600 000, 70 000, 17 000}}, Delimiter,
  Style["φ₃", Bold, Large], {{KF3, 1.0 * 10⁻¹¹, "K_φ₃[cm²/N]"}, {1.1 * 10⁻⁹, 1.0 * 10⁻¹¹, 1.0 * 10⁻¹⁰, 1.0 * 10⁻⁸, 12.0 * 10⁻¹⁰}}, {KF3, 1.0 * 10⁻⁸, 1.0 * 10⁻¹¹},
  {{rox, 1.04, "r_ox [-]"}, {1.04, 3.45}},
  Style["φ₄", Bold, Large], Delimiter, {{k4, 6.8 * 10⁻⁸, "k_φ₄[1/s]"}, {6.8 * 10⁻⁸, 4 * 10⁻⁸, 1}}, Delimiter,
  Style["φ₅", Bold, Large], {{k5, 1, "k_φ₅[1/s]"}, {1.0 * 10⁻⁸, 1. * 10⁻⁶, 1. * 10⁻⁵, 1. * 10⁻⁴, 1}}, Delimiter,

  Style["C1: metal loss from the bare metal", Bold, Large, Red], Style["C2: metal oxidized and included on the FF", Bold, Large, Green],
  Style["C3: metal included mechanically on the FF", Bold, Large, Blue], Style["C4: metal particles out of the contact-WEAR", Bold, Large, Black],

  ControlPlacement → Right]
```

Mathematica code for protocol A (ST4 test)

```mathematica
<< PlotLegends`
Manipulate[
 Plot[{-(t) ((KF1 * ρ_metal * a * F_N * v_s * 1/H) + (KF2 * ρ_metal * (kP/H)^0.5 * (2 * a * F_N * S)^0.5 * v_s)) * 10^3,

  (((t) + (-1 + e^(-(t)*k5))/k5) * (KF1 * ρ_metal * a * F_N * v_s * 1/H) + 1/k4 (((t) * k4 * (KF2 * ρ_metal * (kP/H)^0.5 * (2 * a * F_N * S)^0.5 * v_s)) + ((-1 + e^(-(t)*k4)) * ((KF3) * (ρ_oxide * rox) * (F_N * v_s))))) * 10^3,

  ((1 - e^(-(t)*k5)) (KF1 * ρ_metal * a * F_N * v_s * 1/H))/k5 * 10^3, ((1 - e^(-(t)*k4)) ((KF3) * (ρ_oxide * rox) * (F_N * v_s)))/k4 * 10^3}, {t, 0, 1000},

  PlotRange → {{0, 1000}, {-0.0005, 0.0005}}, PlotStyle → {Red, Green, Blue, Black}, Frame → True, FrameLabel → {"Time [s]", "Metal mass variation [mg]"},
  LabelStyle → Directive[FontSize → 30], ImageSize → Scaled[0.3], AspectRatio → 1, GridLines → Automatic
 ],

 Style["ϕ_1", Bold, Large], {{KF1, 1.61*10^-5, "K_ϕ_1[-]"}, {1.61*10^-5, 0.715*10^-5}}, {{a, 0.4, "a [-]"}, {0.4, 0.14, 1, 0.9}}, {{a, 0.044, 1}},
 {{H, 1600000, "H_in [N/cm^2]"}, {1600000, 70000, 40000, 17000}}, {H, 1600000, 200000}, Delimiter,
 Style["ϕ_2", Bold, Large], {{KF2, 0.86, "K_ϕ_2[-]"}, {0.86, 2.35, 2.61}}, {{kP, 3.83*10^-20, "k_p[cm^2/s]"}, {1.0*10^-17, 2.5*10^-16, 3.83*10^-20}},
 {{H, 1600000, "H_in [N/cm^2]"}, {1600000, 70000, 17000}}, Delimiter,
 Style["ϕ_3", Bold, Large], {{KF3, 1.0*10^-11, "K_ϕ_3[cm^2/N]"}, {1.1*10^-9, 1.0*10^-11, 1.0*10^-10, 1.0*10^-8, 12.0*10^-10}}, {KF3, 1.0*10^-8, 1.0*10^-11},
 {{rox, 1.55, "r_ox [-]"}, {1.55, 1.04, 3.45}}, Delimiter,
 Style["ϕ_4", Bold, Large], Delimiter, {{k_4, 6.8*10^-8, "k_ϕ_4[1/s]"}, {6.8*10^-8, 4*10^-8, 1}}, Delimiter,
 Style["ϕ_5", Bold, Large], {{k_5, 1, "k_ϕ_5[1/s]"}, {1.0*10^-8, 1.*10^-6, 1.*10^-5, 1.*10^-4, 1}}, Delimiter,

 Style["C1: metal loss from the bare metal", Bold, Large, Red], Style["C2: metal oxidized and included on the FF", Bold, Large, Green],
 Style["C3: metal included mechanically on the FF", Bold, Large, Blue], Style["C4: metal particles out of the contact-WEAR", Bold, Large, Black],

 ControlPlacement → Right]
```

Appendix B : Differential equations resolution

- **Compartment 3 and 4**

$\frac{dM_3}{dt} = \phi_1 - \phi_5$ Where $\phi_5 = k_5 \cdot M_3(t)$

$$\frac{dM_3(t)}{dt} = \phi_1 - k_5 \cdot M_3(t)$$

$$\frac{dM_3(t)}{dt} = \phi_1 \cdot \left(1 - \frac{k_5 \cdot M_3(t)}{\phi_1}\right)$$

$$\frac{1}{\left(1 - \frac{k_5 \cdot M_3(t)}{\phi_1}\right)} \cdot \frac{dM_3(t)}{dt} = \phi_1$$

$$\int_{M_{3,0}}^{M_{3,f}} \frac{1}{\left(1 - \frac{k_5 \cdot M_3(t)}{\phi_1}\right)} \cdot dM_3(t) = \int_{t_o}^{t_f} \phi_1 \, dt$$

$$\frac{\phi_1}{-k_6} \cdot \ln\left(1 - \frac{k_5 \cdot M_3(t)}{\phi_1}\right) + M_{3,0} = (t_f - t_o) \cdot \phi_1$$

$$\frac{\phi_1}{-k_6} \cdot \ln\left(1 - \frac{k_5 \cdot M_3(t)}{\phi_1}\right) = (\Delta t) \cdot \phi_1 - M_{3,0}$$

$$\ln\left(1 - \frac{k_5 \cdot M_3(t)}{\phi_1}\right) = \frac{-k_5}{\phi_1}\left((\Delta t) \cdot \phi_1 - M_{3,0}\right)$$

$$1 - \frac{k_5 \cdot M_3(t)}{\phi_1} = e^{\frac{-k_5}{\phi_1}\left((\Delta t) \cdot \phi_1 - M_{3,0}\right)}$$

$$-\frac{k_5 \cdot M_3(t)}{\phi_1} = e^{\frac{-k_5}{\phi_1}\left((\Delta t) \cdot \phi_1 - M_{3,0}\right)} - 1$$

$$M_3(t) = \left(e^{\frac{-k_5}{\phi_1}\left((\Delta t) \cdot \phi_1 - M_{3,0}\right)} - 1\right) \cdot \left(\frac{\phi_1}{-k_5}\right)$$

If $M_{3,0} = 0$ (initial condition)

$$M_3(t) = \left(e^{-k_5 \Delta t} - 1\right) \cdot \left(\frac{\phi_1}{-k_5}\right)$$

$$M_3(t) = \frac{\left(1 - e^{-k_5 \Delta t}\right) \cdot \phi_1}{k_5}$$

The development is similar for the mass balance of the compartment 4, where k_5 is replaced by k_4 and ϕ_1 by ϕ_3

- **Compartment 2**

$$\frac{dM_2}{dt} = \phi_2 - \phi_3 + (k_4 \cdot M_4(t)) + (k_5 \cdot M_3(t))$$

We replace $M_4(t)$ and $M_3(t)$

$$\frac{dM_2}{dt} = \phi_2 - \phi_3 + \left(k_4 \cdot \frac{(1 - e^{-k_5 t}) \cdot \phi_3}{k_5}\right) + \left(k_6 \cdot \frac{(1 - e^{-k_5 t}) \cdot \phi_1}{k_5}\right)$$

Simplifying and putting in common

$$\frac{dM_2}{dt} = \phi_2 - \phi_3 + \left((1 - e^{-k_4 t}) \cdot \phi_3\right) + \left((1 - e^{-k_5 t}) \cdot \phi_1\right)$$

$$\frac{dM_2}{dt} = \phi_2 + \phi_3(-1 + 1 - e^{-k_4 t}) + \left((1 - e^{-k_5 t}) \cdot \phi_1\right)$$

$$\frac{dM_2}{dt} = \phi_2 + \phi_3(-e^{-k_4 t}) + \left((1 - e^{-k_5 t}) \cdot \phi_1\right)$$

$$M_2(t) = \int_{t_o}^{t_f} \phi_2 \, dt - \left(\phi_3 \int_{t_o}^{t_f} e^{-k_4 t} \, dt\right) + \left(\phi_1 \int_{t_o}^{t_f} (1 - e^{-k_6 t}) \, dt\right)$$

$$M_2(t) = \phi_2(t_f - t_o) - \left(\phi_3 \frac{1}{-k_4} \left(e^{-k_4 t_f} - e^{-k_4 t_o}\right)\right) + \phi_1(t_f - t_o) - \left(\phi_1 \frac{1}{-k_5} \left(e^{-k_4 t_f} - e^{-k_4 t_o}\right)\right)$$

with initial time $t_o = 0s$

$$M_2(t) = \phi_2 t - \left(\phi_3 \frac{1}{-k_4} \left(e^{-k_4 t} - 1\right)\right) + \phi_1 t - \left(\phi_1 \frac{1}{-k_5} \left(e^{-k_4 t} - 1\right)\right)$$

$$M_2(t) = \phi_2 t + \left(\phi_3 \frac{\left(e^{-k_4 t} - 1\right)}{k_4}\right) + \phi_1 t + \left(\phi_1 \frac{\left(e^{-k_4 t} - 1\right)}{k_5}\right)$$

$$M_2(t) = \phi_2 t + \left(\phi_3 \frac{\left(e^{-k_4 t} - 1\right)}{k_4}\right) + \phi_1 t + \left(\phi_1 \frac{\left(e^{-k_4 t} - 1\right)}{k_5}\right)$$

$$M_2(t) = \phi_2 t + \left(\phi_3 \frac{\left(e^{-k_4 t} - 1\right)}{k_4}\right) + \phi_1 \left(t + \frac{\left(e^{-k_4 t} - 1\right)}{k_5}\right)$$

List of symbols

		Units
ρ_{metal}	Density of the metal	$\left[\frac{g}{cm^3}\right]$
ρ_{oxide}	Density of the oxide	$\left[\frac{g}{cm^3}\right]$
ϕ	Mass rate	$\left[\frac{g}{s}\right]$
ε	Ratio between V_F and V_{S4}	[-]
$|Ox|_4$	Oxide mass on C4	[g]
$|M^o|_3$	Metal mass on C3	[g]
a (d)	Attenuation factor	[-]
d	Oxide thickness	[69]
C_1	Compartment 1	
C_2	Compartment 2	
C_3	Compartment 3	
C_4	Compartment 4	
F_N	Normal force	[N]
H	Hardness	[N/cm^2]
$\dot{m}$	Mass flow	$\left[\frac{g}{s}\right]$
k_p	Parabolic oxidation constant	[cm^2/s]
K_{ϕ_1}	Proportionality constant of ϕ_1	[-]
K_{ϕ_2}	Constant proportional to the probability that an asperity can be depassivated	[-]
K_{ϕ_3}	Proportionality constant of ϕ_3	[cm^2/N]
k_{ϕ_4}	First order rate constant of ϕ_4	[1/s]
k_{ϕ_5}	First order rate constant of ϕ_6	[1/s]
t_{cycle}	Cycle time	[s]
t_r	Rubbing time	[s]
$\dot{V}_{chem}$	Chemical volume rate	$\left[\frac{cm^3}{s}\right]$
$\dot{V}_{mech}$	Mechanical volume rate	$\left[\frac{cm^3}{s}\right]$
$\dot{V}_{oxide}$	Oxide volume rate	$\left[\frac{cm^3}{s}\right]$
v_s	Sliding velocity	[cm/s]

Curriculum Vitae

Sandra Guadalupe

Born May 18, 1983 in Quito, Ecuador

FORMATION

2010-2014	*Doctoral student and assistant in the Tribology and Interfacial Chemistry Group, Ecole Polytechnique Fédérale de Lausanne, Switzerland. Under the supervision of Dr. Stefano Mischler*
2010	*Master of Science MSc in Molecular and Biological Chemistry, Ecole Polytechnique Fédérale de Lausanne, Switzerland.*
2009	*Bachelor in Chemistry and Chemical Engineering, Ecole Polytechnique Fédérale de Lausanne, Switzerland.*

PUBLICATIONS

S. Guadalupe Maldonado, S. Mischler, W.-J. Chitty, C. Falcand, Effect of dwell time and electrode potential on the tribocorrosion of Stellite, in: Nordic Symposium on Tribology 2012 (NORDTRIB 2012), Trondheim, Norway, 2012

Sandra Guadalupe Maldonado, Stefano Mischler. Marco Cantoni, Walter-John Chitty, Carole Falcand, Dominique Hertz, *« Mechanical and chemical mechanisms in the tribocorrosion of a Stellite type alloy »*, Wear 308 (2013) 213-221.

PENDING PUBLICATIONS

Shoufan Cao, Sandra Guadalupe, Stefano Mischler, "Wear modeling of artificial hip joints combining tribocorrosion and lubrication", (Submitted to Wear)

S. Guadalupe Maldonado, S. Mischler, W.-J. Chitty, C. Falcand, "Tribocorrosion of CoCr alloys with different carbides content"

S. Guadalupe Maldonado, J. Perret, S. Mischler, W.-J. Chitty, C. Falcand, "Modeling of the electrochemical response in PWR conditions"

ORAL PRESENTATIONS

- ECOTRIB2011, « 3rd European Conference on Tribology », 7-9 Juin 2011, Vienne (Austria), *"Plasma Electrolytic Oxidation coatings on Zirconium for tribological applications"*.
- NORDTRIB2012, « 15th Nordic Symposium on Tribology », 12-15 Juin 2012, Trondheim, Norway, *"Mechanical and chemical contribution to the tribocorrosion of Stellite"*.
- Friction, Wear and Wear Protection, 6-8 Mai 2014, Karlsruhe, Germany, *"Tribocorrosion of CoCr alloys with different carbides contents"*

POSTERS

- LDDR, « 19th International Local Drug Delivery meeting and cardiovascular course on Revascularization & Molecular strategies», 2-4 Février 2012, Genève, Suisse, *"Improving wear corrosion resistance of zirconium in aqueous solutions".*
- 3rd International Conference on Tribocorrosion, 19-20 Avril 2012, Atlanta, Etats-Unis, "Electrochemical response of stainless steel during wear in pressurized high temperature water"
- Gordon Research Conference, Coupled Challenges at the moving interface, July 20-25, 2014, Bentley University, Waltham, MA, « Tribocorrosion modeling in pressurized high temperature water »